THÈSE POUR OBTENIR LE GRADE DE DOCTEUR
DE L'UNIVERSITÉ DE MONTPELLIER

En Mathématiques et Modélisation

École doctorale Information, Structures et Systèmes

Unité de recherche IMAG UMR 5149

Simulation de l'interaction fluide-structure dans les valves veineuses

Présentée par Barthélémy THIBAUD
le 9 décembre 2024

Sous la direction de Franck NICOUD
et Simon MENDEZ

Devant le jury composé de

Guillaume BALARAC, Professeur des universités, Université Grenoble Alpes	Président
Guillaume OGER, Ingénieur de recherche, CNRS	Rapporteur
Julien FAVIER, Professeur des universités, Aix-Marseille Université	Rapporteur
Victoria TISHKOVA LEONI, Maîtresse de conférence, Aix-Marseille Université	Membre
Antonia PEREZ MARTIN, Professeure des universités practicien hospitalier, Université de Montpellier	Membre
Franck NICOUD, Professeur des universités, Université de Montpellier	Directeur
Simon MENDEZ, Chargé de recherche, CNRS	Co-directeur

UNIVERSITÉ DE MONTPELLIER

A mon oncle Guy,

A mes grands parents.

Remerciements

Au terme de cette thèse, un travail riche en défis, en apprentissages et en découvertes, je tiens à exprimer ma profonde gratitude à toutes les personnes qui ont contribué à la réussite de ce projet.

Je remercie tout d'abord chaleureusement Franck Nicoud et Simon Mendez, pour leur encadrement exemplaire. Votre expertise, vos conseils éclairés, votre rigueur scientifique et votre disponibilité constante ont été des piliers de ce travail. Vous m'avez non seulement transmis des connaissances précieuses, mais aussi une méthode et une vision scientifiques qui m'accompagneront tout au long de ma carrière. Je suis profondément reconnaissant pour votre soutien et votre confiance.

Je tiens à remercier Guillaume Oger et Julien Favier, pour avoir accepté le rôle exigeant de rapporteurs de cette thèse. Je suis également très reconnaissant à Guillaume Balarac, Victoria Tishkova Leoni et à Antonia Perez Martin, membres du jury pour la pertinence de vos conseils.

Je remercie chaleureusement l'ensemble des acteurs projet DYV-MTEV. Je commencerais par le corps hospitalier avec Antonia Perez Martin, Jean-Christophe Gris, Elsa Faure, Julien Frandon et Isabelle Quere, mais également nos expérimentalistes, Arianna Gianetti, Manouk Abkarian, Christine Benistant et Elisabeth Guenot.

Ma gratitude va également à l'ensemble des membres de l'équipe de l'IMAG, Nathalie Collain, Brigitte Labric, Céline Dricot, Laurence Roux, Sophie Cazanave, Carmela Madonia, Heinui Bottemer, Karine Bonnet et Baptiste Chapuisat pour leur disponibilité, leur patience et leur aide précieuse.

Un grand merci à mes collègues enseignants-chercheurs du département de mathématiques que j'ai côtoyé au cours mon année d'ATER. Tout particulièrement, je souhaite remercier Pascal Azerad et Moulay Benameur, pour leur soutien et conseils avisés, qui m'ont permis de progresser et d'affiner méthodes d'enseignements.

Le paragraphe le plus attendu, le plus scruté (est-ce qu'il m'a oublié ?), le plus redouté (est-ce que je t'ai oublié ?) : celui pour les copains. Merci à vous, les vieux, qui m'avez accueilli à bras ouvert : Julien, Thiziri, Ivan, Emmanuel, Tom et Amandine, Alan et Albin. À vous qui avez embarqué dans cette aventure avec moi, et qui avez partagé les moments de joies, de stress, de fêtes : Raph, Victor, Junyi et

Emmanuel. À mes co-bureaux : Agathe et Ozzi pour les plus anciens, et les ajouts récents : Alex et Pierre-Louis. À celleux qui ont pris le train en marche (on rentre dans le dur) : Hermès, Salomé, Aurelio, Amélie, Pablo, Joris et Juliette et à celleux que je n'ai pas cités, mais se reconnaîtrai. Merci pour votre soutien. À nos sorties randos, week-end ski, semdoc, bars d'après semdoc et bien d'autres moments. Merci à vous Alain et Pascal, aux ~~Chouffe~~ Granini du jeudi soir, sorties slack/rivière et autres bagatelles.

En fait, j'ai menti en voilà un deuxième, mais celui-ci pour les *copains*. À nos pauses café, à nos envolées sans queue ni tête, un peu border où Tanguy avait toujours une réponse, ces envolées parfois gênantes dont seul Pedro a le secret. À nos blagues nulles et pas nulles qui nous ont quand même bien fait rire. A nos soirées jeux Orlane, aux pandas de Suraxe battus à plat de couture (et oui ! Ce n'est pas des licornes les pandas). Merci à toi Corentin, qui m'a initié au métal alors que je partais de loin. Et mercé Matchiiilde pour nos discussions foot et ces tunnel-visions qu'on s'est pris, on retournera voir des matchs promis, de LDC cette fois-ci. Ce temps passé avec vous était précieux, je languis ceux qui arrivent. Et puis la team s'est agrandit : Salut Pierre-Louis, Alex et Anne.

Je souhaite aussi adresser un grand merci à mes amis hors de la sphère IMAG, rencontré sur la route. Tout d'abord sur le chemin des bruits du quotidien : Soumaya notre écologue préférée : "Oh regarde une buse", "Regarde la route Soum!!", Omar mon acolyte qui m'a fait découvrir les joies de la falaise, et Marina celle de la slack. Mais depuis la fin l'INSA, il n'y qu'une équipe qui est restée, soudée, contre vents et marées, malgré les emplois du temps serrés, les randos de 23 bornes qui en deviennent 30, les Cévennes, Bisca-plage, Viel-Aure, Besse, le GR20, des cailloux, un col, encore des cailloux, un vallon, toujours des cailloux... Même si je n'ai pas pu le faire avec vous, merci pour ces moments de vie Juliette, Clément et Guillaume.

A ma famille, à mon père qui m'a toujours poussé à me dépasser (merci d'avoir préféré aller à la plage) et à ma mère et ma sœur qui m'ont toujours soutenu, merci pour votre amour et votre confiance. Au Mas Germain où j'ai grandi à vos côtés Tatie Véro, Tonton Lionel, Camille et Mamie Sylvette et qui m'avez toujours permis de me ressourcer et de me retrouver. À mes grands-parents Solange et Daniel, il est bien loin le temps où je m'entêtais derrière cette brouette qui ne voulait pas avancer. Et parce que la vie à la campagne sans animaux ce n'est pas vie à la campagne, merci à Ninou, Nala, Pou, Dune, Flèche et Patch.

Mes dernières pensées sont pour Morgane, qui a bien voulu me prendre en chemin et sans qui la vie serait beaucoup moins fun.

Contents

Résumé substantiel en français

La thrombose veineuse profonde (TVP) constitue l'une des principales causes de mortalité dans les pays occidentaux, se classant au troisième rang des maladies cardiovasculaires après l'infarctus du myocarde et l'accident vasculaire cérébral. Elle s'inscrit dans un ensemble de maladies plus vaste appelé thrombo-embolie veineuse (TEV), qui englobe à la fois la TVP et l'embolie pulmonaire. Les conséquences cliniques et socio-économiques sont considérables : hospitalisations prolongées, complications aiguës ou chroniques (comme le syndrome post-thrombotique) et coûts de santé élevés. L'enjeu médical majeur consiste à mieux comprendre la formation des caillots afin de réduire l'incidence et la gravité de la TEV.

Les valves veineuses jouent un rôle central dans la genèse de la TVP. Présentes en grand nombre dans le réseau veineux profond des membres inférieurs, notamment au niveau poplité et fémoral, elles assurent un flux unidirectionnel vers le cœur. Chaque valve comprend deux feuillets tapissés d'endothélium et entourés de tissus conjonctifs et musculaires. C'est dans les poches valvulaires (ou sinus) que les thromboses se forment le plus souvent : ces zones, soumises à des conditions hémodynamiques complexes, peuvent favoriser la stagnation sanguine ou altérer l'activation endothéliale. Des études récentes suggèrent que les cellules endothéliales des sinus valvulaires, soumises à des régimes d'écoulement changeants, développent une réponse antithrombotique spécifique, par exemple via l'expression régulée de protéines clés telles que la thrombomoduline (TM) et le facteur von Willebrand (vWf). Un déséquilibre de cette réponse pourrait faciliter l'initiation du thrombus.

C'est dans ce contexte qu'intervient le projet DYV-MTEV (Dynamique des sacs valvulaires et complications aigües et chroniques de la maladie thrombo-embolique veineuse). Porté par une collaboration entre le CHU de Nîmes, le Centre de Biologie Structurale (CBS) et l'Institut Montpelliérain Alexander Grothendieck (IMAG), ce programme vise à décrypter le rôle de l'hémodynamique valvulaire dans la modulation de la réponse endothéliale. Trois approches sont menées en parallèle : (1) l'acquisition et l'analyse d'imagerie clinique (échographie Doppler, IRM) pour caractériser le mouvement et le flux au niveau des valves profondes ; (2) des expérimentations in vitro, notamment sur des cellules endothéliales exposées à des contraintes mécaniques (tension et cisaillement) reproduisant les conditions observées dans les sinus valvulaires ; (3) la modélisation numérique par interaction fluide-structure (IFS), permettant de simuler avec précision la dynamique de la valve et l'écoulement sanguin local. Les objectifs principaux de cette thèse sont d'évaluer qualitativement la dynamique des valves veineuses et l'hémodynamique associée sous différentes con-

ditions de flux sanguin, géométries valvulaires et tailles de vaisseaux. Comme décrit précédemment, les valves veineuses sont des tissus biologiques mis en mouvement par le flux sanguin. D'un point de vue physique, ce système représente une structure immergée dans un fluide, les deux interagissants de façon dynamique. La méthode numérique adaptée à la simulation de ce système est la méthode d'interaction fluide-structure (IFS).

Le Chapitre 2 présente la méthodologie de simulation employée pour modéliser la dynamique de valves veineuses dans un contexte d'interaction fluide-structure (IFS). Les outils décrits font partie de la suite YALES2BIO, dérivée du solveur YALES2, reconnue pour son efficacité en calcul parallèle sur maillages non structurés. Pour le fluide, les équations de Navier-Stokes sont résolues dans un cadre ALE (Arbitrary Lagrangian-Eulerian), pour permettre de suivre la déformation de la valve. La valve est traitée comme un solide hyperélastique, soumise à de grandes déformations. Le modèle néo-hookéen est utilisé pour caractériser les déformations de la valve. La résolution s'effectue par éléments finis (FEM), en régime dynamique via le schéma implicite de Newmark, incluant un amortissement de Rayleigh pour stabiliser la réponse.

Par la suite, le chapitre aborde les développements spécifiques à la simulation des valves veineuses. La première difficulté réside dans la gestion du contact entre les feuillets valvulaires, qui se touchent et se séparent au cours du cycle cardiaque. Une méthode de contact par pénalisation a été implémentée à cet effet. Plutôt que de détecter directement le contact entre les deux feuillets, on exploite ici une symétrie : chaque feuillet est repoussé par une force pénalisante quand il s'approche le plan de symétrie. Bien que la pénalisation ne soit pas strictement conservative, cette approche, simple à implémenter et suffisamment régulière, garantit la stabilité numérique de l'algorithme de couplage. Le couplage fluide-structure repose sur un schéma partitionné semi-implicite de type prédicteur-correcteur : le fluide et la structure sont résolus successivement par un point fixe, et l'on itère jusqu'à la convergence à chaque pas de temps. Pour prévenir l'effet de masse ajoutée (très fort quand fluide et solide ont la même densité), on emploie une sous-relaxation dynamique avec la méthode d'Aitken, qui calcule un facteur d'itération optimal pour stabiliser et accélérer la convergence. Les champs de forces pariétales du fluide sont transmises au solide via l'interface CWIPI, de même que le champ de déplacement du solide renvoyé vers le fluide. Le mouvement du maillage fluide s'effectue grâce à la méthode pseudo-solide ; la résolution d'un problème statique sur ce pseudo-solide fournit un champ de déplacement qui « déforme » le maillage fluide et préserve une bonne qualité de maillage proche de l'interface. Si la distorsion dépasse un certain seuil, on recourt au remaillage dynamique via la librairie MMG3D.

Enfin, le chapitre se conclut par la validation de l'ensemble de la chaîne de calcul. Un premier test illustre la méthode de contact (balle creuse rebondissant sur un plan rigide), confirmant la pertinence de la pénalisation et la conservation quasi intégrale de l'énergie (selon l'amortissement introduit). Puis, pour la partie IFS, un cas bidimensionnel classique (une languette flexible transversale à un écoulement) met en évidence la précision de la méthode partitionnée et la concordance avec

des résultats de référence. L'implémentation de tous ces développements (contact, modèle néo-hookéen et accélération par Aitken) offre ainsi un cadre complet pour aborder la simulation de valves veineuses soumises à des conditions réalistes de flux et de déformation.

Le Chapitre 3 présente une étude détaillée sur l'anatomie des valves veineuses, permettant le développement du modèle in silico de valve utilisé dans ces travaux. Par le passé, les études se sont concentrées exclusivement sur le régime de déformation par étirement. La pression nécessaire à l'ouverture de la valve est bien trop grande (100 mmHg) comparée à la pression disponible en position allongée (20 mmHg). Le régime de déformation résultant d'une réserve de surface, le flambement, semble être le bon candidat pour garantir le retour veineux. Le flambement étant extrêmement rapide, il est d'autant plus éprouvant pour les méthodes numériques.

C'est donc l'hypothèse de réserve de surface qui est retenue pour la modélisation de la valve veineuse. La valve est modélisée comme un solide hyperélastique, avec un modèle néo-hookéen. Le couplage fluide-structure est réalisé avec les modalités présentées dans le paragraphe précédent. L'écoulement sanguin est imposé par un débit pulsé en entrée, reproduisant une situation de pompe respiratoire en position allongée. Les principaux outils d'analyse utilisés pour caractériser la dynamique des valves veineuses et l'hémodynamique associée sont présentés :

- La dynamique des feuillets combinée au ratio d'ouverture.
- Les structures d'écoulement formées en aval des feuillets.
- Le taux de vidange par l'ensemencement uniforme de traceurs dans le sinus.
- Les efforts pariétaux sur les cellules endothéliales.

Les résultats montrent que la valve est capable de s'ouvrir avec un gradient de pression suffisamment faible (0.3 mmHg) pour permettre le retour veineux. On observe de fortes recirculations dans le sillage des commissures de la valve. On remarque que les feuillets près de leurs commissures ont du mal à s'ouvrir, créant une zone morte non négligeable. Un régime transitoire se développe en aval de la valve avec une réorientation de la nappe fluide dans la direction normale, phénomène observé dans la dynamique des jets elliptiques. L'hémodynamique dans le sinus se caractérise par trois zones d'écoulement différentes : proche de la base de la valve, les traceurs ont très peu de mouvement ; proche du bord de fuite, les traceurs sont évacués rapidement dans une zone de recirculation à l'orée du sinus ; enfin, une zone intermédiaire où les traceurs ont un mouvement d'aller-retour. La zone de stagnation semble dû au peu de mouvement du feuillet à sa base.

Cette étude ouvre sur plusieurs questions concernant le drainage et l'hémodynamique dans le sinus, notamment sur l'effet de la position de la valve le long de la cuisse, de la chasse musculaire et de la géométrie de la valve.

Le Chapitre 4 explore ces différentes questions. Concernant la position de la valve le long de la cuisse, trois différentes positions sont simulées : une valve de

veine poplitée (6 mm, petit diamètre, $v_{max} = 16$ cm/s), une valve de veine fémorale commune (10 mm, moyen diamètre, $v_{max} = 20$ cm/s) et une valve de veine fémorale commune (14 mm, grand diamètre, $v_{max} = 20$ cm/s). Les simulations montrent que la position de la valve le long de la cuisse a un impact significatif sur le drainage du sinus. Pour le plus petit diamètre on observe un ratio d'ouverture moindre comparé au moyen et grand diamètre, 33% contre 42%. Ce plus petit ratio d'ouverture est dû à une ouverture incomplète des feuillets. Le manque d'amplitude du feuillet s'accompagne d'un manque de mouvement dans le sinus, changeant la dynamique de sa vidange comparée aux moyen et grand diamètres. Les structures de recirculation derrière les feuillets sont comparables entre les trois diamètres. On observe un écoulement stable en aval de la valve de petit diamètre, légèrement déstabilisé pour le moyen diamètre et des lâchés tourbillonnaires pour le grand diamètre.

Dans un second temps, l'impact de la chasse musculaire est étudié. La simulation de chasse musculaire reprend le cas moyen diamètre (10 mm) après 2 cycles, en imposant un plus fort débit en entrée pour le 3^e cycle ($v_{max} = 40$ cm/s, observations cliniques). On observe des lâchés tourbillonnaires dans le sillage des feuillets pour le cas de la chasse musculaire. Les résultats montrent que la chasse musculaire a un impact significatif sur la dynamique de la vidange du sinus pour le cycle observé. Le ratio d'ouverture est plus élevé (50%) comparé au cycle sans chasse musculaire (42%), accompagné d'un vidage plus efficace du sinus.

Enfin, le chapitre se termine par une étude de sensibilité sur la géométrie de la valve. La géométrie de la valve de grand diamètre (14 mm, $v_{max} = 20$ cm/s) est modifiée par une légère relaxation de l'angle d'insertion des feuillets accompagnée d'une élision du bord libre proche des commissures. Les résultats montrent que la forme des feuillets a un impact significatif sur la dynamique de la valve. La recirculation a bien lieu à l'intérieur du sinus, ce qui permet un meilleur mélange et drainage du sinus. Le temps de résidence, estimé en extrapolant la quantité de traceurs restant le sinus, est beaucoup plus court pour la géométrie modifiée, 10 s contre 31 s pour la géométrie de référence.

En conclusion, ces travaux de thèse ont permis de développer un modèle numérique de valve veineuse, capable de reproduire la dynamique des valves et l'hémodynamique associée à une valve avec réserve de surface. Les simulations ont permis de caractériser la dynamique des valves veineuses et l'hémodynamique associée sous différentes conditions de flux sanguin, géométries valvulaires et tailles de vaisseaux. Les résultats montrent que la valve est capable de s'ouvrir avec un gradient de pression suffisamment faible pour permettre le retour veineux, et que la géométrie de la valve a le plus d'impact la dynamique et le drainage des sacs valvulaires.

Les perspectives de ces travaux sont nombreuses. Du point de vue biomécanique, on peut citer l'application de parois de veines déformables pour reproduire plus fidèlement les conditions de la pompe musculo-squelettique, l'utilisation de géométries spécifiques de patients ou encore l'effet de la jonction sapheno-fémorale sur la dynamique de la valve. Du point de vue numérique, on peut envisager une méthode de contact plus fidèle capable de gérer les contacts feuillet-feuillet.

Chapter1

Introduction

Chapter overview: *This introductory chapter aims to provide the reader with an overview of the thesis background. This PhD focuses on the study of the hemodynamics in the vicinity of deep vein valves. The clinical context around deep vein thrombosis, the mechanisms responsible for the disease and the implication of vein valves are first presented. The importance of the study of deep vein valve associated hemodynamics is then highlighted and placed in the context of the project "Dynamique des sacs valvulaires et complications aigües et chroniques de la maladie thrombo-embolique veineuse" (DYV-MTEV).*

Contents

1.1 Motivations

Cardiovascular diseases, particularly venous thromboembolism (VTE), are a leading cause of mortality in Western countries [1–3]. Wendelboe and Raskob [3] reported that the global incidence rate (per $100,000$) and mortality rate for VTE were between 115 to 269 and 9.4 to 32.3, respectively, positioning VTE as the third most common cardiovascular disease after myocardial infarction and stroke. In the UK, the total

cost to national public health resources for VTE events was estimated at €950 million in 2005 [4]. More recently, according to Grosse et al. [5], the annual cost of incident VTE events in the US is estimated to be between 7 and 10 billion dollars per year. Notably, one in ten hospital-acquired VTEs is preventable [5, 6]. A deeper understanding of the onset mechanisms of VTE could help reduce the number of VTE events and associated costs, which are substantial.

VTE encompasses both acute manifestations, such as deep vein thrombosis (DVT), and chronic conditions, such as post-thrombotic syndrome (PTS). DVT involves the formation of a thrombus, primarily in the leg, which can dislodge and lead to pulmonary embolism (PE), a potentially fatal complication. PTS, on the other hand, results in chronic pain due to residual venous obstruction and/or damage to the vein wall, causing venous hypertension.

The factors contributing to VTE have been extensively studied. Cohen et al. [4] noted that three-quarters of DVT-related deaths were caused by hospital-acquired DVT, often due to immobilization. The mechanisms leading to thrombosis can be grouped into Virchow's triad:

- **Blood stasis:** Blood flow can be reduced or stopped due to clinical conditions, bed rest, or immobility, enhancing the stagnation of prothrombotic factors.
- **Endothelium injury:** The endothelium, a layer of cells lining the vein wall, plays a crucial role in preventing thrombus formation. These cells can be damaged by surgery or injury, reducing their protective function.
- **Hypercoagulability:** An abnormal increase in prothrombotic factors is widely documented as playing a key role in the onset of DVT.

Hemostasis is a complex physiological process that prevents excessive bleeding following vascular injury and maintains blood fluidity within the circulatory system. It involves a tightly regulated balance between procoagulant and anticoagulant factors. Upon endothelial activation or damage, the coagulation cascade is initiated, leading to the formation of a fibrin clot. Two key proteins play crucial roles in this process: thrombomodulin (TM) and von Willebrand factor (vWf). TM is an integral membrane protein expressed on the surface of endothelial cells, acting as a cofactor for thrombin-mediated activation of protein C, an anticoagulant that inhibits further thrombin generation and fibrin formation [7, 8]. Conversely, vWf is a multimeric glycoprotein synthesized by endothelial cells and megakaryocytes, essential for platelet adhesion to the subendothelial matrix and platelet aggregation under high shear stress conditions [9, 10]. By modulating the expression of TM and vWf, endothelial cells can influence the coagulation mechanism, promoting either anticoagulant or procoagulant states depending on mechanical stimuli and pathological conditions.

The formation of a thrombus is thus a complex process involving interactions between blood flow, the vein wall, and blood components, making it difficult to predict. Thrombi are predominantly formed at the level of venous valves. Indeed, in most veins a series of bicuspid (two leaflets) valves are present to ensure the unidirectionality of the blood flow. They are particularly present in the deep venous system (popliteal and femoral veins) in greater number in proximity of the ankle,

and less present in superficial venous system (saphenous vein). Blood clots often onset in the valvular bags, as demonstrated by Sevitt [11], see Figure 1.1a. Venous valves, which are passive one-way valves that prevent the backflow of blood and ensure venous return to the heart, are critical in this process. However, the mechanisms leading to thrombus formation in this region remain unclear, with various hypotheses proposed. Among them, the hemodynamic modulation of the endothelial antithrombotic response in the venous valve sinus could play a decisive role. Brooks et al. [12] showed, using immunofluorescence in great saphenous veins, that endothelial cells (ECs) in the valve sinus exhibit greater thromboresistance compared to ECs in the lumen. Recently, the loss of the perivalvular antithrombotic phenotype in mice, due to a transition to non-oscillatory flow, was demonstrated by Welsh et al. [13]. This supports the link between blood flow patterns and the antithrombotic response of ECs near the valve, as emphasized by Welsh et al. [13]. Therefore, the role of the venous valve system, its environment, and the associated hemodynamics in the onset of DVT warrants further investigation.

DVT often leads to post-thrombotic syndrome, where the perivalvular endothelium could be damaged by thrombus formation, leading to chronic venous insuffi-

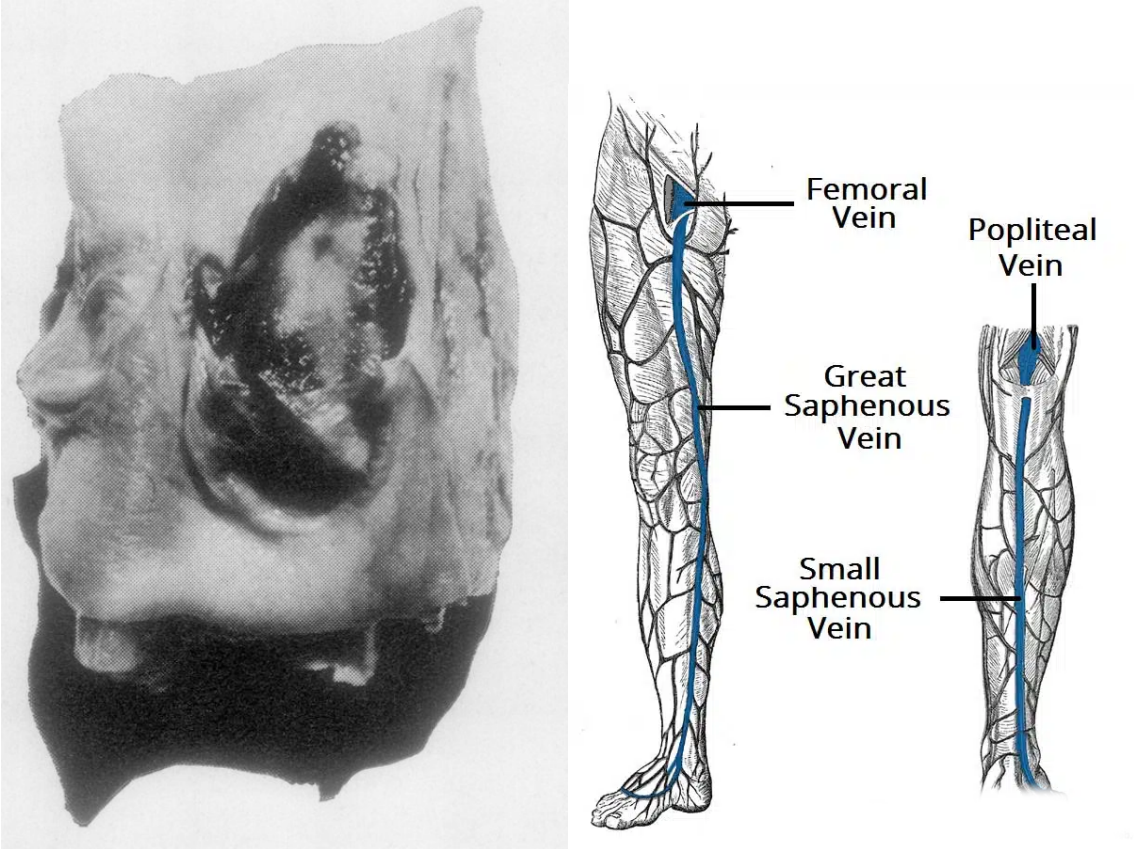

(a) (b)

Figure 1.1: (a) Image of a thrombus in a valve sac from a deceased individual, extracted from [11]. (b) Schematic representation of the veins in the leg.

ciencies. Valve dysfunction can induce altered hemodynamic patterns, increasing the risk of DVT recurrence, and the risk of post-thrombotic syndrome (PTS). PTS results either from valve efficiency loss or chronic vein thrombosis, both resulting in peripheral venous hypertension. Varicose veins lead to venous reflux and venous ulcers. Investigating the effect of blood flow pattern modulation on valve dynamics could provide new insights into the onset of chronic venous insufficiencies. Valves are present throughout the cardiovascular system, especially in the heart and veins. Since cardiac valves have been extensively studied in the literature [**astorino_fluid-structure_2008**, 14–24], they provide a valuable reference for comparison with vein valves. Hence, a brief introduction to the cardiovascular system is presented in the next section to provide context on the role of valves within the system.

1.2 The cardiovascular system

In this section, a general overview of the cardiovascular system, from the heart to the blood vessels, is presented. Further details are provided on the blood transport system, particularly focusing on the arteries and veins. The information provided in this section is primarily extracted from [25].

1.2.1 Generalities

The cardiovascular system is composed of the heart and blood vessels. It operates as a closed circuit with two distinct, but interconnected, parts: the pulmonary circulation and the systemic circulation. To function, body tissues and cells require oxygen, which is delivered by the blood in the systemic circulation. As cells use oxygen, they produce carbon dioxide, which is also removed by the blood. The pulmonary system is responsible for gas exchange, where oxygen is absorbed by the blood, and carbon dioxide is expelled.

The heart is a muscular organ that pumps blood throughout the body. It is divided into four chambers: the left and right atria, and the left and right ventricles. The left side of the heart pumps oxygenated blood to the body tissues, while the right side pumps deoxygenated blood to the lungs. The blood circulation through the heart is depicted in Figure 1.2. The direction of blood flow within the heart is regulated by four valves. The composition of these cardiac valves is similar to artery wall composition and includes endocardium reinforced with connective tissues such as smooth muscle cells and collagen. Cardiac valves are discussed in detail in Section 1.3.1.

1.2.2 Blood transport: arteries and veins

The blood vessels comprise arteries, veins, and capillaries. Arteries transport blood from the heart to the systemic (high pressure) and pulmonary circulations which are submitted to pulsatile flow, while veins carry blood back to the heart. Therefore, blood in the arteries of the systemic circulation is oxygen-rich, while blood in the

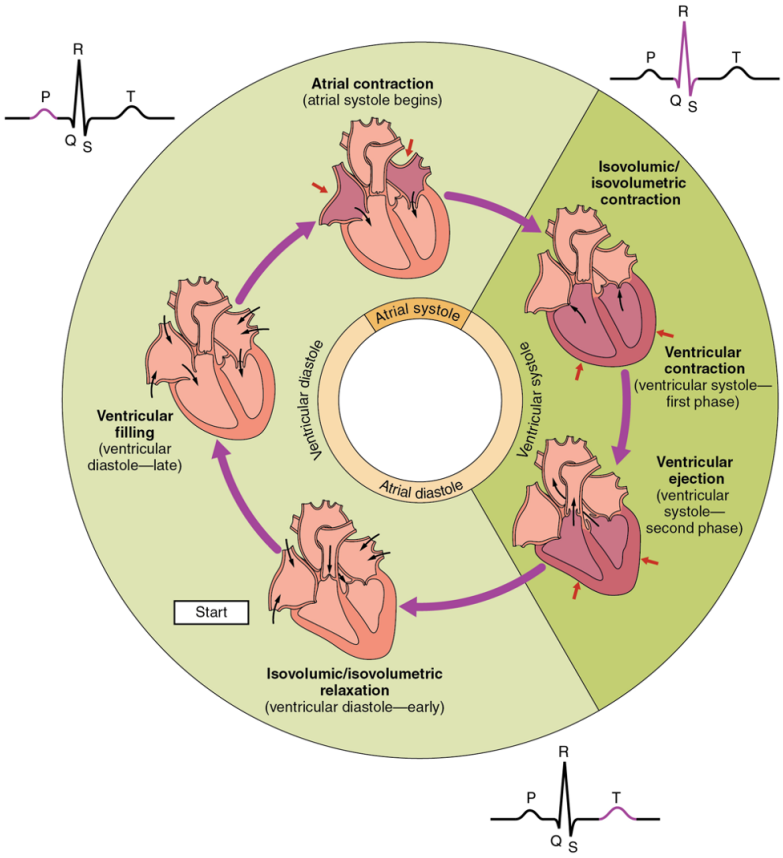

Figure 1.2: Detailed view of the cardiac cycle, linked with the heart's electrical activity. Extracted from [25]

arteries of the pulmonary circulation is carbon dioxide-rich, and the reverse is true for the veins. Capillaries, which connect arteries and veins, are the sites of gas exchange between blood and tissues. As this section focuses on arteries and veins, the reader is referred to Tuma, Duràn, and Ley [26] *Microcirculation* for a comprehensive analysis of the capillaries. The walls of arteries and veins share a common three-layer structure composed of the tunica intima, tunica media, and tunica externa [27]. Despite this common structure, the composition of each layer differs slightly between arteries and veins, as presented in Figure 1.3a. The following subsections provide more detail on these layers.

1.2.2.1 Tunica intima

The tunica intima is composed of the endothelium (the innermost layer) and a connective tissue layer. The endothelium, which is in direct contact with the blood, is continuous throughout the cardiovascular system, including the heart chambers. It is a dynamic structure capable of changing its phenotype in response to different stimuli. The endothelium rests on a basement membrane called the basal lamina, which provides strong yet permeable support, allowing materials to pass through.

Communication with the outer layers is essential for the endothelium to regulate blood flow through vasodilation and vasoconstriction, as well as to facilitate angiogenesis. The endothelium also plays a crucial role in regulating coagulation and inflammation. It is actively antithrombogenic, as demonstrated in [12, 13].

Under the microscope, the endothelium in arteries appears wavy due to the constriction of the smooth muscle cells in the tunica media, while in veins, it appears smooth Figure 1.3b

1.2.2.2 Tunica media

The tunica media is the middle layer of the artery and vein walls. It consists of smooth muscle cells, elastic and collagen fibers. The smooth muscle cells control vasodilation and vasoconstriction of the vessels, thereby regulating blood flow as needed. The elastic fibers are abundant in the artery media composition in contrast with the vein media composition. The opposite tendency is observed for collagen fibers, conferring strength to the vein wall. The tunica media is the thickest layer in arteries, enabling them to handle high pressures and maintain vessel shape. In contrast, this layer is much thinner in veins due to the lower blood pressure. In veins, the presence of the vasa vasorum (vessels of the vessels) and nervi vasorum (nerves of the vessels) ensures the supply of oxygen and nutrients to the innermost layers of the vessel wall. These structures are absent in the tunica media of arteries, making the supply of oxygen and nutrients to the inner layer more challenging, which may explain why arterial diseases are more common than venous diseases [25].

1.2.2.3 Tunica externa

The tunica externa is the outermost layer of the artery and vein walls. It is composed of collagen and elastic fibers. The tunica externa protects the vessel and anchors it to surrounding tissues. It is the thickest layer in veins, which gives the vein wall

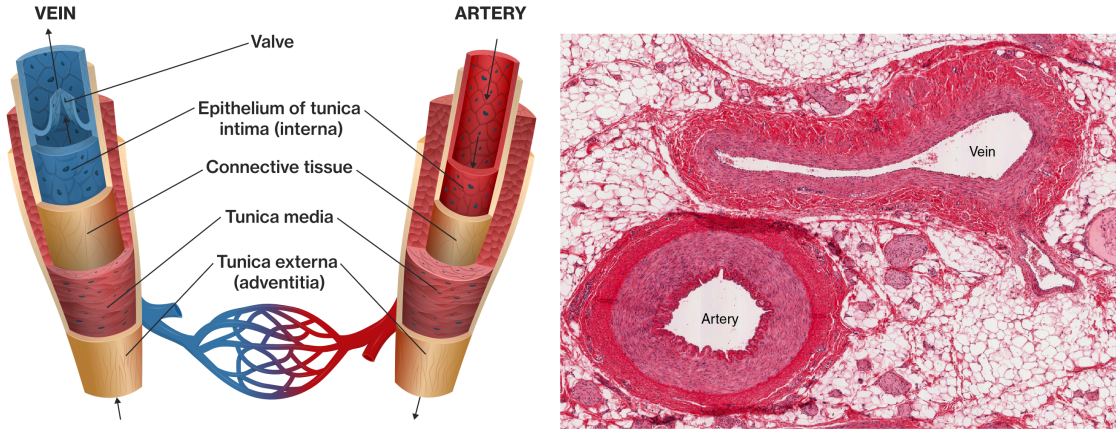

(a) (b)

Figure 1.3: (a): Layer composition of arteries and veins. (b): Micrograph showing the different layers of both artery and vein wall. Extracted from [25].

its flexibility, allowing it to deform under the influence of the calf muscle pump mechanism.

Having established a global understanding of the cardiovascular system, with a particular focus on the structural and functional aspects of arteries and veins, we now turn our attention to the critical role that valves play within this system. The following section delves into the specific function of valves within the cardiovascular system and examines the hemodynamics associated with their operation. Understanding these mechanisms is essential for appreciating the complexities of blood flow regulation and the prevention of conditions such as venous thromboembolism.

1.3 Valves in the cardiovascular system and associated hemodynamics

1.3.1 Cardiac valves

The unidirectional flow of blood within the heart is ensured by the presence of four valves. A overview of the blood flow in the heart and the disposition of the cardiac valves is presented in Figure 1.4.

Blood intake into the ventricles is regulated by the mitral and tricuspid valves, located between the atria and the ventricles on the left and right sides of the heart, respectively. The mitral valve is a bi-leaflet valve, while the tricuspid valve is a tri-leaflet valve. Each leaflet of these valves is attached to papillary muscles via the chordae tendineae, which control the opening and closing of the valves. A key function of the chordae tendineae is to prevent valve inversion during the systolic phase, when the valves are subjected to high-pressure conditions while in the closed position.

Blood outflow is controlled by the aortic and pulmonary valves, each composed of three leaflets. The aortic valve is situated between the left ventricle and the aorta, while the pulmonary valve is located between the right ventricle and the pulmonary artery. The leaflets of these valves are attached to the vessel wall by the sinuses of Valsalva, which are very stiff and do not deform significantly. These sinuses are crucial for valve closure, as they fill with blood during the systolic phase, aiding in the proper closure of the leaflets. The functioning of these two valves is closely related to that of vein valves. Due to their critical role in heart function and the potential for severe complications if they malfunction, aortic and pulmonary valves have been extensively studied in the literature from both clinical [15, 21, 23, 24, 28–34] and numerical perspectives [**astorino_fluid-structure_2008**, 16, 17, 20, 22, 35–41].

The aortic and pulmonary valves also play a key role in preventing the backflow of blood towards the ventricles during the diastolic phase. As these valves close under lower pressure conditions than the mitral and tricuspid valves, they do not require chordae tendineae to prevent inversion. Weind, Ellis, and Boughner [24] demonstrated the presence of microvessel structures in porcine aortic valves, noting that microvessels are present only in parts of the cusps with a thickness greater

than 0.5 mm, primarily at the base of porcine aortic valves. The mean thickness of human aortic valve cusps is 0.6 mm [23], indicating that the endothelium on aortic valve cusps receives oxygen and nutrients from their internal microvasculature.

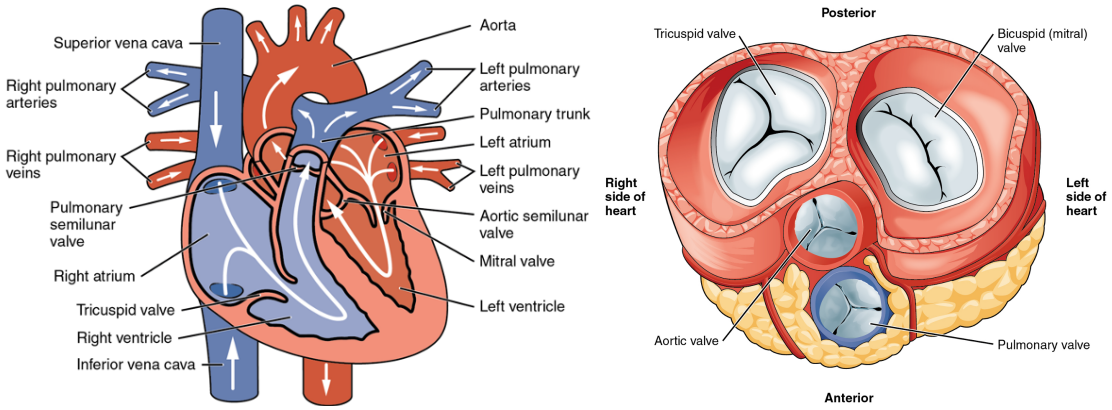

Figure 1.4: Blood flow in the heart (left) and disposition of the cardiac valves (right). Extracted from [25]

1.3.2 Comparison with vein valves

Vein valves are present throughout the venous system, predominantly in the lower limbs. They are bi-leaflet valves located approximately every 4 cm along the deep veins of the lower limbs [42]. The valves are less spaced in the calf compared to the thigh veins. A schematic 2D view of a vein valve is depicted in Figure 1.5. Thrombus formation is primarily located in the venous valve sinus. Similar to the sinuses of Valsalva in the aortic valve, the valve sinuses in veins are located behind the leaflets, where they are filled with blood during valve closure. However, the geometry of venous valves is highly dependent on their location and the individual patient. Moreover, as the vein wall deforms significantly due to the calf muscle pump mechanism (detailed in Section 3.1.2), the dynamics of the valves are also highly dependent on the deformation of the vein wall.

As illustrated in Figure 1.6, research on venous valves has received less interest in the computational community compared to aortic valve studies. The number of publications per year on the topic of aortic valves is significantly higher than those focused on vein valves.

1.3.2.1 Associated blood flow sequences

In veins, valve dynamics are primarily driven by the skeletal muscle pump (more details in Section 3.1.2). When the leg muscles contract, they compress the deep venous system between themselves and the bones, resulting in a pressure increase inside the deep veins. As the pressure is higher in the lower limbs than in the trunk, blood flows towards the heart, flushing the blood from the valve sinuses. When

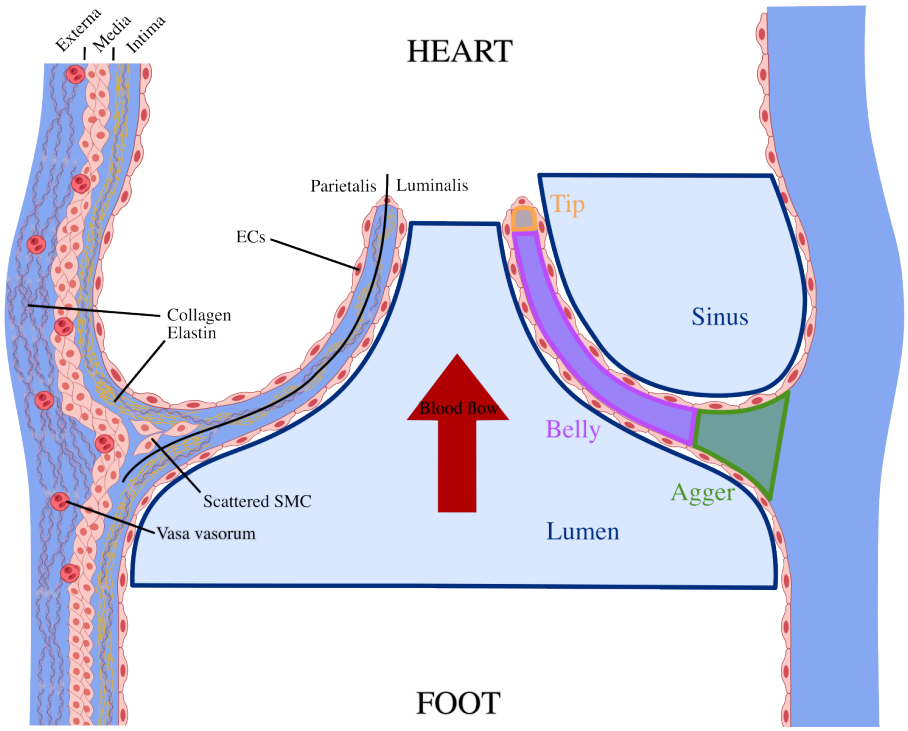

Figure 1.5: Left: Histological description of a vein valve. Right: Vein valve nomenclature. ECs: endothelial cells, SMC: smooth muscle cells. Created with Biorender [43].

the calf muscles relax, pressure in the deep veins drops, causing a reversal in blood flow direction, which fills the valve sinuses and closes the valves by pushing the leaflets together. During this phase, endothelial cells (ECs) are subjected to two mechanical stresses: stretch from the underlying tissues and shear stress from the blood entering the sinuses. This part of the dynamics is similar to that of the aortic valve. In the veins of the thorax and abdomen, this cycle is driven by the respiratory pump. During inhalation, pressure in the thorax drops below that in the abdominal veins, causing blood to flow from the abdomen to the thorax. The opposite occurs during exhalation. These mechanisms are typical for a person in a standing position. When a person is at bed-rest, blood flow is primarily driven by the respiratory pump, with the calf muscle pump remaining inactive. This leads to reduced blood flow in the deep veins, which is why patients are at increased risk of deep vein thrombosis (DVT) during extended periods of bed rest. The skeletal muscle pump is essential for the opening and closing of vein valves. In the ultrasound images of a femoral vein valve presented in Figure 1.7, the valves appear to "float" in the flow without opening or closing, indicating that the blood inside the sinuses is not being renewed. This stagnation can lead to the concentration of thrombogenic factors and the onset of thrombus formation if there is no movement for several hours.

In conclusion, vein valves are subjected to various blood flow patterns. A key question that arises is: How does the blood flow pattern in the vicinity of the valve

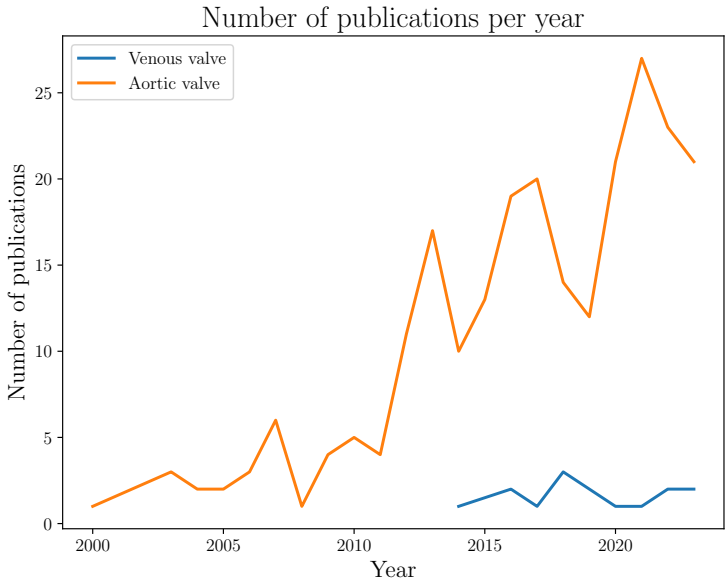

Figure 1.6: Number of publications in the field of cardiac and vein valves in the computational community (from PubMed [44]). The search terms used were "aortic valve fluid-structure interaction" and "vein valve fluid-structure interaction".

modulate the antithrombotic response of ECs? This is the main question that the DYV-MTEV project seeks to answer. The working hypotheses of the project and the objectives of this work are presented in the next section.

1.4 The DYV-MTEV project

1.4.1 Working hypotheses of the project

The DYV-MTEV project aims to investigate the role of hemodynamic modulation and its effect on the anti-thrombotic response of endothelial cells in the perivalvular region. This project is a collaboration between the CHU of Nîmes, the CBS (Centre de Biologie Structurale in Montpellier), and the IMAG (Institut Montpelliérain Alexander Grothendieck, University of Montpellier). The project is divided into three main parts, each led by one of the participating institutions.

The CHU of Nîmes is responsible for collecting medical imaging data from patients under different hemodynamic conditions. The dynamics of the vein valves in the popliteal and femoral veins are captured using ultrasound imaging. Doppler's ultrasound imaging is used to extract maximum velocities and cycle modulation of the blood flow under various conditions: bed-resting, with calf muscle contraction, and in a standing position. These data serve as essential inputs for the CBS and IMAG teams. Additionally, samples of vein valves are collected during surgery and analyzed by the CBS team.

The CBS is in charge of the experimental part of the project. This work was con-

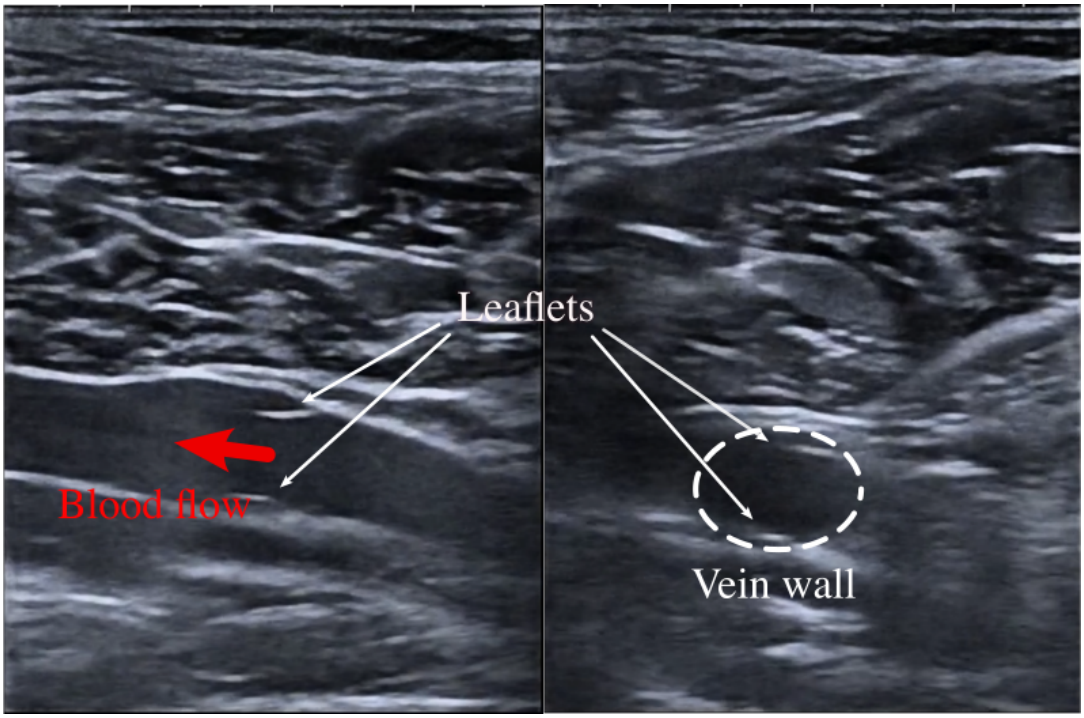

Figure 1.7: Ultrasound of a femoral vein valve in the sagittal (left) and transversal plane (right). The leaflets are indicated with white arrows, the sinus wall is in white dashed line and the blood flow direction with a red arrow.

ducted during the PhD of Arianna Gianetti [45], with the objective of characterizing the antithrombotic phenotype of human umbilical vein endothelial cells (HUVECs) under stretch, shear stress, or both, through experiments in a microfluidic device. The first part of this work focuses on a non-destructive protocol employing MRI and microCT scans to characterize a venous valve geometry. They reveal insights into the 3D structure of venous valves, particularly the thickening at the valve sinus. These findings already suggest that stretch plays a pivotal role in the mechanical conditions encountered by the leaflets, and that the hemodynamics within the sinus pocket exhibit a level of complexity beyond the traditional understanding. In the second part of this study, the response of a confluent layer of endothelial cells (ECs) to in-plane uniaxial cyclic stretching was explored. The activation state of ECs was monitored, and the expression of key anticoagulant proteins, thrombomodulin (TM) and von Willebrand factor (vWf) [12, 13], which play pivotal roles in hemostasis and platelet adhesion, was measured. Various factors, including topography, timescale, magnitude of stretch, and intermittent stretching, were investigated to unravel the intricate relationship between mechanical strain and the expression of TM and vWf. The findings revealed that cell alignment and the development of a thromboresistant phenotype were induced by uniaxial cyclic stretching, accompanied by an increase in TM expression. In contrast, the initiation of the coagulation cascade was brought about by discontinuous stretching which simulating stasis resulting in an elevated vWf presence on the EC surface.

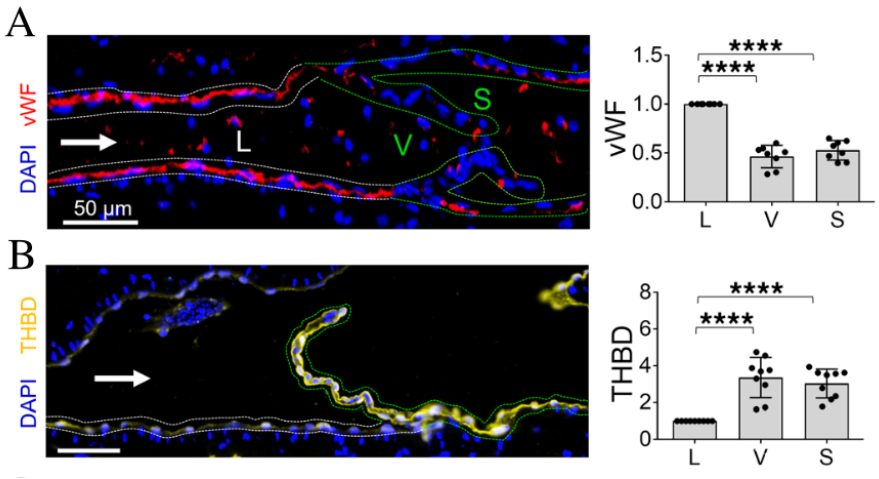

Figure 1.8: Immunostained mouse saphenous veins to detect expression of the prothrombotic protein von Willebrand factor (vWF in Figure A) and the antithrombotic protein thrombomodulin (THBD in Figure B). Relative quantitation of staining in luminal (L), valve (V) and sinus (S) endothelial cells is shown at right for each protein. Extracted from [13].

The third part of the project is conducted by the IMAG team as part of this PhD. The objectives of this thesis and the organization of the manuscript are presented in the next section.

1.4.2 Objectives of the thesis

The mechanical stresses applied to ECs in vein valves are primarily due to blood flow and the skeletal muscle pump. The main objectives of this thesis are to qualitatively assess the dynamics of vein valves and the associated hemodynamics under different blood flow conditions, valve geometries, and vessel sizes. As previously described, venous valves are biological tissues that are moved by blood flow. From a physical standpoint, this system represents a structure immersed in a fluid, both interacting dynamically. The natural tool to simulate this system is the fluid-structure interaction (FSI) technique.

Chapter 2 of the thesis is dedicated to the state of the art of FSI methods used for valve dynamics simulation, followed by a detailed description and validation of the numerical method employed in this work. Chapter 3 provides an overview of the current literature on vein valves (including geometry, mechanical features, and associated blood flow sequences), presents the obtained model geometry, and describes the simulation sequences used. Chapter 4 presents the results of the FSI simulations of the vein valve models. The thesis concludes with a discussion of the findings and perspectives for future work in Chapter 5.

Chapter2

Numerical Methods

Chapter overview: *The methods used to model the vein valves are detailed in this chapter. These methods are part of the YALES2BIO solver suite. The different approaches are introduced step by step, starting with the fluid solver, followed by the structure solver, and concluding with the coupling solver. The main achievements of this thesis, as presented in this chapter, include the implementation of a penalty-based algorithm for contact between the leaflets, the neo-Hookean model for structural deformation, and the Aitken method for coupling acceleration and stabilization. A suitable benchmark is also proposed to provide a complete validation of the solver in a valve-like configuration.*

Contents

2.1 Fluid-structure interaction simulations for vascular system

Computational fluid dynamics (CFD) has been extensively applied in various cardiovascular problems to estimate hemodynamics, including intracardiac blood flow [20, 46, 47], cardiac valves [22, 39, 41, 48–50], and arterial deformation [51–54]. Simulating cardiovascular systems requires solving a multiphysics problem, which may involve fluid dynamics, structural deformation, and electrical conduction. In the case of cardiac or venous valves, the interaction between blood flow and deformable structures, such as valve and vein tissues, is crucial. Fluid-structure interaction (FSI) methods are naturally suited for these kinds of problems. A brief introduction to the physics at stake in FSI simulations is presented next.

2.1.1 Fluids and solids

In this work, the physics of both fluids and solids are addressed, treating them as continuous media within the framework of continuum mechanics. Despite this commonality, their responses to applied stresses diverge fundamentally. For a solid Ω_s, the stress at any point depends on the deformation from a reference configuration; that is, stress is a function of how much the material has been stretched or compressed relative to its original, undeformed state. This relationship is characterized by constitutive laws such as Hooke's law for elastic materials, where stress is directly related to strain. In contrast, fluids lack a fixed reference configuration and continuously deform under applied stress. The stress in a fluid depends on the rate of deformation, specifically the strain rate tensor, which reflects how quickly the fluid elements are changing shape. This behavior is described by constitutive equations like Newton's law of viscosity, where stress is proportional to the rate of strain. Consequently, while both fluids and solids are continuous media, their differing stress-strain relationships necessitate distinct analytical approaches, detailed hereafter.

2.1.1.1 The Navier Stokes equations for a Newtonian incompressible fluid

Let consider a computational domain Ω_f filled with a Newtonian incompressible fluid. The set of differential equations governing the motion of a Newtonian incompressible fluid is known as the Navier-Stokes equations. These equations describe locally the conservation of momentum and mass for a fluid. The Navier-Stokes equations are derived from the conservation of mass and momentum, and they are given by:

$$\frac{\mathrm{d}\mathbf{v}}{\mathrm{d}t} = -\frac{\nabla P}{\rho_f} + \nu\Delta\mathbf{v} + \mathbf{f}_v \tag{2.1a}$$

$$\nabla \cdot \mathbf{v} = 0 \tag{2.1b}$$

where t is the time (> 0), $\mathbf{v}$ is the fluid velocity vector, P the pressure, ρ_f the fluid density, ν the kinematic viscosity, and $\mathbf{f}_v$ a volumetric force. From this point, initial conditions of the fluid velocity must be prescribed within Ω_f:

$$\mathbf{v}(\mathbf{x}, t = 0) = \mathbf{v}_0(\mathbf{x}) \tag{2.2}$$

The pressure do not need to be prescribed as it is determined by the incompressibility condition (2.1b) (detailed in Section 2.3.2). The Navier-Stokes equations are supplemented by boundary conditions on the fluid domain $\partial\Omega_f$, which can be of to types:

1. Dirichlet boundary conditions, where the fluid velocity is prescribed:

$$\mathbf{v} = \mathbf{v}_b \tag{2.3}$$

   where $\mathbf{v}_b$ is the prescribed velocity at the boundary.

2. Neumann boundary conditions, where the fluid stress is prescribed:

$$\mathbf{t}_b = -P\mathbf{n} + \mu\frac{\partial\mathbf{v}}{\partial n} + \mu\nabla\mathbf{v}^T\mathbf{n} \tag{2.4}$$

   where $\mathbf{t}_b$ is the prescribed stress at the boundary, $\mathbf{n}$ the outward unit normal vector, and μ the dynamic viscosity.

2.1.1.2 The Equations of Motion for a Linear Elastic Solid

Consider a computational domain Ω_s occupied by a linear elastic solid. The behavior of the solid is governed by the equations of continuum mechanics, specifically the balance of linear momentum and the constitutive relations for linear elasticity. These equations describe the conservation of momentum and the relationship between stress and strain within the solid. The equations of motion for a linear elastic solid are given by:

$$\rho_s \frac{\mathrm{d}^2 \mathbf{u}}{\mathrm{d}t^2} = \nabla \cdot \boldsymbol{\sigma} + \mathbf{f}_s \tag{2.5a}$$

$$\boldsymbol{\sigma} = \mathbf{C} : \boldsymbol{\varepsilon} \tag{2.5b}$$

$$\boldsymbol{\varepsilon} = \frac{1}{2}\left(\nabla \mathbf{u} + \nabla \mathbf{u}^\top\right) \tag{2.5c}$$

Where t is time ($t > 0$), $\mathbf{u}$ is the displacement vector, $\boldsymbol{\sigma}$ is the Cauchy stress tensor, ρ_s is the solid density, $\mathbf{f}_s$ is a body force per unit volume, $\mathbf{C}$ is the fourth-order elasticity tensor (material stiffness tensor), and $\boldsymbol{\varepsilon}$ is the linearized strain tensor.

The initial conditions for the solid displacement and velocity must be prescribed within Ω_s:

$$\mathbf{u}(\mathbf{x}, t = 0) = \mathbf{u}_0(\mathbf{x}) \tag{2.6a}$$

$$\frac{\mathrm{d}\mathbf{u}}{\mathrm{d}t}(\mathbf{x}, t = 0) = \mathbf{v}_0(\mathbf{x}) \tag{2.6b}$$

The equations of motion are supplemented by boundary conditions on the solid domain boundary $\partial\Omega_s$, which can be of two types:

1. Dirichlet boundary conditions, where the displacement is prescribed:

$$\mathbf{u} = \mathbf{u}_b \tag{2.7}$$

   where $\mathbf{u}_b$ is the prescribed displacement at the boundary.

2. Neumann boundary conditions, where the traction (stress vector) is prescribed:

$$\boldsymbol{\sigma} \cdot \mathbf{n} = \mathbf{f}_b \tag{2.8}$$

   where $\mathbf{f}_b$ is the prescribed force vector applied on the boundary, and $\mathbf{n}$ is the outward unit normal vector to the boundary $\partial\Omega_s$.

2.1.1.3 Coupling of the fluid and solid dynamics

In the context of FSI, the fluid and solid domains are coupled through the interface Γ, defined as the common boundary between the fluid and solid domains. The fluid force deforms the solid and as the solid moves, the fluid domain follows. The fluid-structure coupling is determined by the following kinematic and dynamic conditions:

$$\mathbf{v}_b = \dot{\mathbf{u}} \quad \text{on} \quad \Gamma \tag{2.9a}$$

$$\boldsymbol{\sigma} \cdot \mathbf{n} = \mathbf{t}_b \quad \text{on} \quad \Gamma \tag{2.9b}$$

where $\mathbf{v}_b$ is the fluid velocity at the interface, $\dot{\mathbf{u}}$ is the solid velocity at the interface, $\boldsymbol{\sigma}$ is the solid stress tensor, $\mathbf{n}$ is the outward unit normal vector to the interface, and $\mathbf{t}_b$ is the traction (force) applied on the interface. The coupling conditions are thus enforced as a Dirichlet-Neumann problem on the interface Γ. The fluid and solid

motion are solved simultaneously, ensuring that the interface conditions are satisfied at each time step. The influence of the fluid on the solid and vice versa depends greatly on the density ratio of the solid to the fluid. For example, in aerodynamics problems the density ratio is often very low, leading to a weak coupling between the fluid and the solid. In contrast, in problems like valve dynamics, the density ratio is close to 1, leading to a strong coupling between the fluid and the solid. Numerically solving cardiovascular problems requires a robust and stable algorithm to handle the strong coupling between the fluid and solid. The principal methods used to solve FSI cardiovascular problems are presented next.

2.1.2 Monolithic Approaches

Monolithic methods for Fluid-Structure Interaction (FSI) represent a comprehensive approach to solve coupled problems involving fluid and solid mechanics. Unlike partitioned methods, which solve the fluid and structure subproblems separately and iterate between them, monolithic methods solve the entire system (fluid, structure and coupling equations) simultaneously. This approach ensures strong coupling between the fluid and structure, leading to more stable and accurate solutions, especially for problems with significant interaction effects, such as valve dynamics. Monolithic methods are particularly advantageous in scenarios where the fluid-structure interface undergoes large deformations or when the fluid and structure have very close densities, leading to a strong "added mass effect." By formulating the FSI problem within a unified framework, these methods avoid the convergence issues and stability problems often encountered in partitioned approaches, making them a robust choice for complex FSI simulations.

As the work presented in this manuscript only treats of incompressible Newtonian fluids, solely monolithic methods involving this kind of fluid are described. Considering the incompressible fluid and structure physics within a single set of equations leads to solving a large-scale nonlinear and non-SPD system (symmetric positive definite) which is mathematically challenging. Geometric or algebraic multigrid methods have been used either as solvers or as preconditioners associated with Krylov subspace methods like GMRES (Generalized Minimal Residual) to construct monolithic methods, see [55–57] and [58–60], respectively. GMRES is an iterative method that minimizes the residual over a Krylov subspace [61]. Its flexibility and robustness make GMRES particularly suitable for solving the large, sparse, and non-SPD linear systems encountered in monolithic FSI approaches. Additionally, this method can be used with a variety of other preconditioners, such as domain decomposition [62–64] or LDU-factorization methods. In the context of biomechanics, these methods are particularly used for cardiovascular problems, such as the electro-fluid-structure simulation of the cardiac cycle [65, 66], and arterial deformation [67–69].

2.1.3 Partitioned Techniques

In partitioned methods, the fluid and structure subproblems are solved separately, and the solutions are iteratively exchanged between the two domains until convergence is reached. This approach is more flexible and modular than monolithic methods, as it allows for the use of different solvers well-suited for the fluid and structure subproblems. Different strategies can by employed to formulate the problem: body-fitted methods [16, 17, 20, 35, 36, 38, 40, 53, 70–75], non body-fitted methods [22, 39, 41, 48–50, 76, 77] or meshless methods.

In body-fitted methods, the fluid and structure are solved on non-overlapping meshes, communicating through the interface. This methodology is particularly suited to capture flow features close to the interface. To closely follow the movement of the interface and preserve mesh quality, the mesh needs to move accordingly, which increases the computational cost. Immersed boundary methods are more flexible and easier to implement, as the fluid is solved on a fixed mesh and the structure is immersed in the fluid domain, albeit at the expense of accuracy. These methods have been applied to a wide range of cardiovascular problems, such as arterial flow [**astorino_fluid-structure_2008**], vocal fold vibration [77], vein and lymphatic valves [48, 73, 76], and cardiac valves [22, 39, 41, 48–50]. For a complete overview of the state of the art on cardiac valve FSI simulation, the reader is referred to the work of [14] and the references therein.

The stability of FSI methods is greatly dependent on the density ratio of the solid to the fluid. This echoes with the weak and strong coupling presented in Section 2.1.1.3. The dynamic equilibrium for a weak coupling problem is easily obtained, as the fluid and the solid only need one solving on each side to converge. In contrast, from the inertial coupling of strongly coupled problems arises the added mass effect [78–87]. The added mass effect can lead to instabilities in the simulation, such as difficulties in achieving convergence or even non-converging algorithms. To ensure the convergence of the system, a subiterative procedure is usually required, often supplemented by stabilization techniques. Different stabilization techniques are presented hereafter.

2.1.4 Stabilizating iterative procedures

The artificial compressibility method [88–94] considers a pseudo-compressible fluid by adding a stabilization term to the mass conservation equation:

$$\nabla \cdot \mathbf{u} + C\frac{P_k - P_{k-1}}{\Delta t} = 0 \tag{2.10}$$

where $\mathbf{u}$ the fluid velocity, P the pressure, k the sub-iteration index, C the artificial compressibility coefficient, and Δt the time step. This term vanishes as the coupling converges towards equilibrium, ensuring the incompressibility condition is not violated. However, adding a term to the mass conservation equation can lead to difficulties in solving the fluid linear system.

Robin boundary conditions are mixed Dirichlet-Neumann conditions designed to stabilize the fluid-structure interface [80, 95–100]. These can be applied either

on the fluid or the structure interface boundary condition. For example, on the solid boundary condition Equation (2.9b), the fluid acts as a viscous damper on the structure through fluid forces. The main idea of the Robin condition is to divide the fluid force into two parts: the actual force from the fluid onto the solid and the force due to the solid's movement. The force due to the solid's movement is the added mass term; this part is deducted from the right-hand side of the momentum balance equation 2.5a and added to the mass term on the left-hand side. This type of boundary condition is closest to the reality of FSI physics; however, segregating the actual force and the added mass is not straightforward in the case of fluid governed by Navier-Stokes equations and requires solving an additional linear system.

The Aitken method is an acceleration technique used to speed up the convergence of a sequence [101–103], and is very popular in FSI partitioned methods [90, 104–109]. This method is of great interest as it does not require heavy implementation and accelerates or slows down the convergence when needed, stabilizing the algorithm. For these reasons, the Aitken method was chosen for implementation in the FSI solver of YALES2BIO, detailed in Section 2.6.5.

2.1.5 Validation Test Cases in the FSI World

FSI algorithms are employed in a wide range of engineering and biomedical problems, from flexible windmill blades [110] to red blood cell transport [111, 112]. Given this variety of applications, several benchmarks have emerged. Part of the work presented here involved finding a suitable benchmark to validate the FSI solver of YALES2BIO within the framework of vein valves.

In the context of arterial blood flow, Wall et al. [113] introduced the lid-driven cavity flow with a flexible bottom, later validated in [114, 115], to test their FSI algorithms in a deformable wall configuration. However, this test case does not test the ability of FSI algorithms to handle the presence of a deformable body fully immersed in the fluid, as is the case in the flow-induced vibration of structures. These configurations are characterized by the alignment of the main direction of the structure and the flow.

Within the scope of flow-induced vibration, several numerical benchmarks involve a rigid body with a flexible flap attached to its wake. Multiple forms have been used, such as in 2D: a square [115–118] or a cylinder [107, 119–121] with the extensively known and validated FSI2 benchmark, or its extension to 3D in turbulent cases [120, 122]. The FSI2 benchmark has already been validated with the YALES2 solver in [120]. Closer to valve configurations, 2D benchmarks with a deformable structure attached perpendicularly to the channel wall and subjected to a normal flow was first introduced by Baaijens [123] and extensively validated later on [124–129]. Adaptations of this benchmark to the contact framework have been realized in [130, 131]. Extensions to 3D are also proposed in [124, 131, 132]. These benchmarks are particularly suited to test the ability of the FSI solver to handle large deformations provoked by a normal fluid flow. The validation of the benchmark presented in [125] is reported in Section 2.6.6.

2.2 Presentation of the YALES2BIO solver suite

In this work, the YALES2BIO solver [133] suite is used to model the vein valves. This suite is an extension of the YALES2 solver suite. The YALES2 library (Yet Another LES Solver) [134] was initially developed to address low-Mach number Navier-Stokes equations, both in incompressible and variable density contexts, employing Large Eddy Simulation (LES) and Direct Numerical Simulation (DNS) methods within a finite-volume framework. YALES2 is capable of handling unstructured meshes and features adaptive grid refinement while ensuring excellent scalability. This scalability is achieved through a Double Domain Decomposition (DDD) strategy.

The DDD approach involves a two-step process. First, the mesh is partitioned into subdomains, each assigned to a different computational core. Next, these subdomains are further divided into groups of elements of a predetermined size, known as element groups (ELGRPs), as depicted in Figure 2.1. This method enables efficient memory usage for cache-aware algorithms and can be leveraged by deflation algorithms [135] to maximize performance on massively parallel computing systems.

However, implementing DDD necessitates specialized data structures. Each ELGRP functions as an independent mesh block, requiring a mechanism to connect elements at the interfaces of different ELGRPs, even within the same processor. An internal communicator is employed to manage the data for nodes, pairs, and faces at these interfaces. Similarly, external communicators handle communications at the interfaces between different processors. Additionally, a separate structure is used to manage elements located on boundaries, facilitating their specific treatment. This architecture is illustrated in Figure 2.1b. While this approach is highly effective, it introduces complexity when implementing new features within the existing code.

The YALES2BIO solver suite extends the capabilities of YALES2 to the fields of biomechanics developed at the IMAG. Through the last 13 years, numerous features have been added to the code to tackle different biomechanical configurations (Figure 2.2). In the context of patient-specific CFD simulations of the left ventricle,

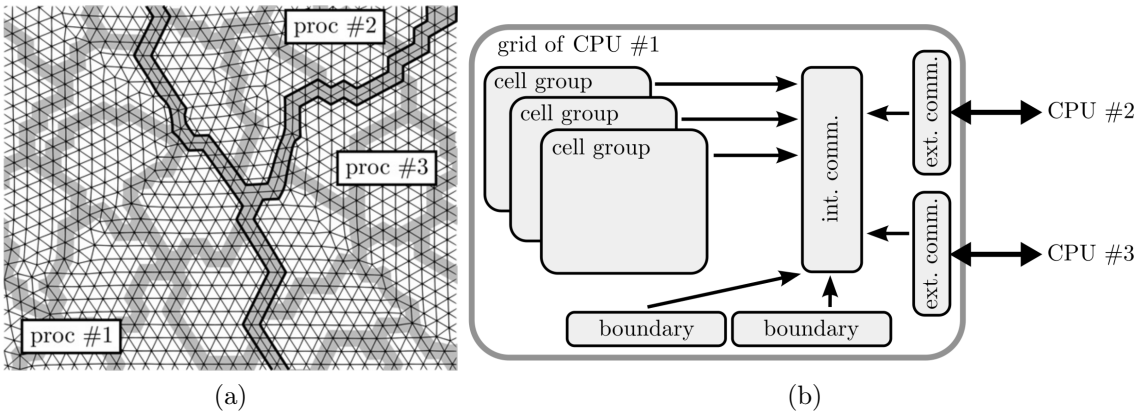

Figure 2.1: On the left, the Double Domain Decomposition (DDD) strategy used in YALES2. Extracted from [134]

an Arbitrary Lagrangian-Eulerian (ALE) method has been introduced [136]. An IBM-based FSI solver have been implemented with macroscopic [22] or microscopic applications [111, 112, 137, 138]. Noticeable contributions have been made in MRI quality control with a simulated MRI solver [139, 140] or in the field of airborne virus transmission [141].

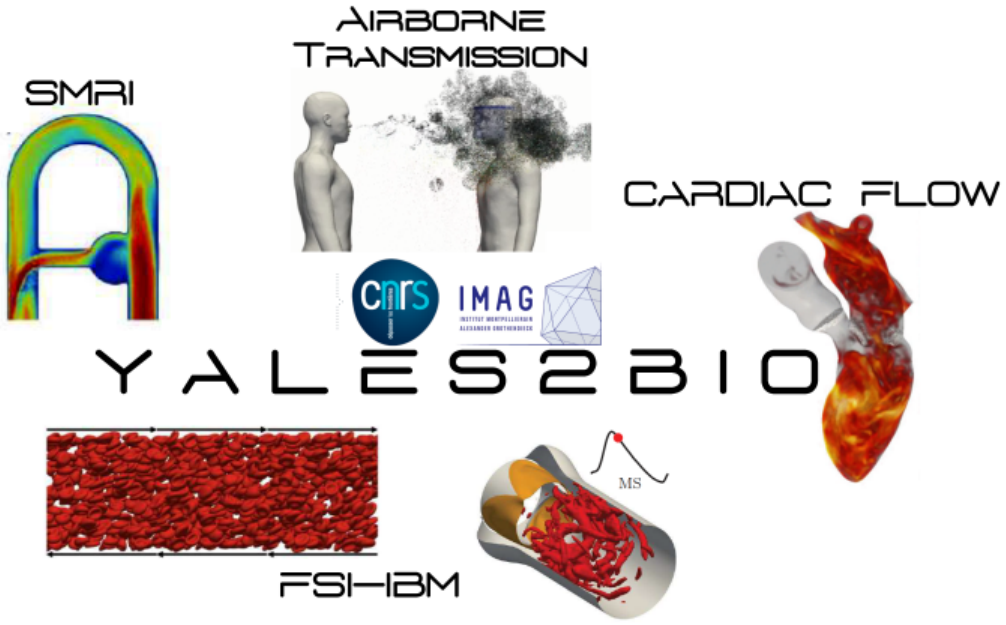

Figure 2.2: Examples of applications of the YALES2BIO solver suite in different fields of biomechanics.

2.3 Arbitrary Lagrangian-Eulerian Solver

2.3.1 Prediction Step in the ALE Framework

In this work, the blood is modeled as a Newtonian fluid and follows the Navier-Stokes equations:

$$\frac{\mathrm{d}\mathbf{v}}{\mathrm{d}t} = -\frac{\nabla P}{\rho_f} + \nu\Delta\mathbf{v} + \mathbf{f}_v \tag{2.11a}$$

$$\nabla \cdot \mathbf{v} = 0 \tag{2.11b}$$

where $\mathbf{v}$ is the velocity vector, P the pressure, ρ the fluid density, ν the kinematic viscosity, and $\mathbf{f}_v$ a volumetric force. To account for the movement of the leaflets, the Arbitrary Lagrangian-Eulerian (ALE) method is used. Integration of the fluid governing equations is done on deformable control volumes, while mesh nodes are

advected as Lagrangian points. The material time derivative $\frac{\mathrm{d}\mathbf{v}}{\mathrm{d}t}$ is written as follows:

$$\frac{\mathrm{d}\mathbf{v}}{\mathrm{d}t} = \frac{\partial \mathbf{v}}{\partial t} + \mathbf{v} \cdot \nabla \mathbf{v} \tag{2.12}$$

Equation (2.11a) has to be modified to take into account the movement of the grid. The control volumes are swept at the grid velocity $\mathbf{w}$. The ALE formulation of the Navier-Stokes equations is then:

$$\frac{\partial \mathbf{v}}{\partial t} + (\mathbf{v} - \mathbf{w}) \cdot \nabla \mathbf{v} = -\frac{\nabla P}{\rho_f} + \nu \Delta \mathbf{v} + \mathbf{f}_v \tag{2.13a}$$

$$\nabla \cdot \mathbf{v} = 0 \tag{2.13b}$$

The volume swept by the grid is substracted from the left-hand side. The time advancement scheme used in this work is a four-stage Low Storage Runge-Kutta method (LSRK4) [142] recast in ALE formalism. It is coupled to Chorin's projection method to solve the incompressibility constraint. The full methodology can be found in [136]. The projection method is broken down into two steps: a prediction step, which consists of fluid velocity advection and grid movement, followed by a correction step to enforce the incompressibility condition. The correction step is presented in the next section. The prediction step consists in integrating Equation (2.13a) between time t_n and t_{n+1} on a node-centered control volume $\omega(t)$:

$$\begin{aligned} \int_{t_n}^{t_{n+1}} \frac{\partial}{\partial t} \int_{\omega(t)} \mathbf{v} \, \mathrm{d}\omega \, \mathrm{d}t + \int_{t_n}^{t_{n+1}} \int_{\omega(t)} \nabla \cdot ((\mathbf{v} - \mathbf{w})\mathbf{v}) \, \mathrm{d}\omega \, \mathrm{d}t = \mathbf{RHS} \\ \mathbf{v}_{n+1} V_{n+1} - \mathbf{v}_n V_n + \int_{t_n}^{t_{n+1}} \int_{\omega(t)} \nabla \cdot ((\mathbf{v} - \mathbf{w})\mathbf{v}) \, \mathrm{d}\omega \, \mathrm{d}t = \mathbf{RHS} \end{aligned} \tag{2.14}$$

where V_n is the volume of the control volume at time t_n, **RHS** is the right-hand side of the Navier-Stokes equation, and $\mathbf{RHS} = \nu \Delta \mathbf{v} + \mathbf{f}_v$. In the following, the **RHS** is omitted for clarity. The four substeps of the Runge-Kutta method are computed as:

$$\begin{aligned} \mathbf{v}_0 &= \mathbf{v}_n \\ \mathbf{v}_i &= \mathbf{v}_n \frac{V_n}{V_i} - \frac{\alpha_i \Delta t}{V_i} \int_{\omega(t_i)} \nabla \cdot ((\mathbf{v}_{i-1} - \mathbf{w}_{n+1})\mathbf{v}_{i-1}) \, \mathrm{d}\omega \quad \text{for} \quad i = 1, \ldots, 4 \\ \mathbf{v}^*_{n+1} &= \mathbf{v}_4 \end{aligned} \tag{2.15}$$

where α_i are the Runge-Kutta coefficients for each substep, $\alpha = [1/4, 1/3, 1/2, 1]$ and $\mathbf{w}_{n+1}$. The LSRK4 method is recovered if $\mathbf{w} = 0$ as $V_n = V_i$. In addition, $\mathbf{w}$ is considered constant during the timestep and the mesh nodes are advected at each substep as follows:

$$\begin{aligned} \mathbf{x}_0 &= \mathbf{x}_n \\ \mathbf{x}_i &= \mathbf{x}_{i-1} + \beta_i \Delta t \mathbf{w}_{n+1} \quad \text{for} \quad i = 1, \ldots, 4 \\ \mathbf{x}_{n+1} &= \mathbf{x}_4 + \beta_f \Delta t \mathbf{w}_{n+1} \end{aligned} \tag{2.16}$$

where β_i are the Runge-Kutta coefficients for the grid velocity substeps, $\beta = [1/8, 1/24, 1/12, 1/4]$. These coefficients are chosen to place the grid at the midpoint configuration, e.g.:

$$\mathbf{x}_i = \mathbf{x}_n + \frac{\alpha_i}{2}\Delta t \mathbf{w}_{n+1} \tag{2.17}$$

The grid is at $\mathbf{x}_{n+\frac{1}{2}}$ at the end of the substeps as confirmed by the summation of the β_i coefficients. Then, a final step is needed with $\beta_f = 1/2$ to get the grid at the correct final position $\mathbf{x}_{n+1} = \mathbf{x}_n + \Delta t \mathbf{w}_{n+1}$.

The time advancement presented above has to verify the Discrete Geometric Conservation Law (DGCL) [143, 144]. This condition ensures that the mesh nodes are advected in a way that the volume swept by the mesh nodes is equal to the volume change between t_n and t_i. In other words, the constant velocity solution has to be preserved even if the grid moves. The DGCL condition in the case of LSRK4 is written as:

$$V_i - V_n = -\alpha_i \Delta t \int_{\omega(t_i)} \nabla \cdot \mathbf{w}_{n+1} \, \mathrm{d}\omega \quad \text{for} \quad i = 1, \ldots, 4. \tag{2.18}$$

The grid nodal position and the metrics evolve linearly through the timestep. This means that the integration domain $\omega(t)$ cannot be equal to V_i to satisfy Equation (2.18). The midpoint configuration is chosen to compute $\omega(t)$ for each substep as given by Equation (2.17). The **RHS** at time t_i is also computed on the midpoint mesh configuration. This method ensures that the DGCL is satisfied at each substep for velocity prediction computation.

2.3.2 Correction Step

At the end of the prediction step, the grid has reached its final position for the timestep. However, the fluid velocity field is not yet divergence-free. The correction step is needed to enforce the incompressibility condition. The Chorin projection method [**chorin_numerical_1997**] is presented by writing Equation (2.13a) with an explicit Euler scheme:

$$\frac{\mathbf{v}_{n+1} - \mathbf{v}_n}{\Delta t} = -\left((\mathbf{v}_n - \mathbf{w}_{n+1}) \cdot \nabla\right) \mathbf{v}_n + \nu \Delta \mathbf{v}_n + \mathbf{f}_v - \frac{\nabla P_{n+\frac{1}{2}}}{\rho_f} \tag{2.19a}$$

$$\frac{\mathbf{v}_{n+1} - \mathbf{v}_n}{\Delta t} = -((\mathbf{v}_n - \mathbf{w}_{n+1}) \cdot \nabla)\mathbf{v}_n + \mathbf{RHS} - \frac{\nabla P_{n+\frac{1}{2}}}{\rho_f} \tag{2.19b}$$

$$\mathbf{v}_{n+1} = \mathbf{v}_n - \Delta t \left((\mathbf{v}_n - \mathbf{w}_{n+1}) \cdot \nabla\right) \mathbf{v}_n + \Delta t \mathbf{RHS} - \Delta t \frac{\nabla P_{n+\frac{1}{2}}}{\rho_f} \tag{2.19c}$$

$$\mathbf{v}_{n+1} = \mathbf{v}^*_{n+1} - \Delta t \frac{\nabla P_{n+\frac{1}{2}}}{\rho_f} \tag{2.19d}$$

where $\mathbf{v}^*_{n+1}$ correspond to the velocity computed by the prediction step Section 2.3.1. Equation (2.19d) must satisfy the incompressibility condition Equation (2.13b). By taking the divergence of Equation (2.19d), the Poisson equation for the pressure is obtained:

$$\Delta P_{n+\frac{1}{2}} = \frac{\rho_f}{\Delta t} \nabla \cdot \mathbf{v}^*_{n+1} \tag{2.20}$$

The linear system Equation (2.20) is solved using a Deflated Preconditioned Conjugate Gradient (DPCG) method [135]. With this newly obtained pressure field $P_{n+\frac{1}{2}}$, the velocity $\mathbf{v}_{n+1}$ is corrected to obtain the divergence-free velocity:

$$\mathbf{v}_{n+1} = \mathbf{v}^*_{n+1} - \frac{\Delta t}{\rho_f} \nabla P_{n+\frac{1}{2}} \tag{2.21}$$

2.4 Structural Mechanics Solver

This solver has been designed to solve the structural deformations of a solid undergoing finite deformation. The solid responds to the momentum balance equation from continuum mechanics. Here is presented its discretized version solved with the Finite Element Method (FEM):

$$\mathbf{M}\ddot{\mathbf{u}} + \mathbf{C}\dot{\mathbf{u}} + \mathbf{K}\mathbf{u} = \mathbf{f} \tag{2.22}$$

where $\mathbf{d}$ is the displacement vector, $\mathbf{M}$ the mass matrix, $\mathbf{C}$ the damping matrix, $\mathbf{K}$ the stiffness matrix, and $\mathbf{f}$ the external forces. More details are given later.

2.4.1 The Finite Element Method: Interpolation and Integration

The Finite Element Method (FEM) is a numerical method used to solve partial differential equations. The main idea is to transform a continuous problem into a discrete problem, to be solved on a finite number of elements. This method was developed in parallel by mathematicians and engineers during the nineteenth and twentieth centuries. The main idea is to divide the domain of the problem into a finite number of elements and solve the problem on each of these elements. The solution is then assembled to provide the global solution of the problem. FEM is a powerful tool for solving complex problems and is widely used for structural analysis.

The method has been introduced and developed in the YALES2 solver suite during the work of Fabbri [120]. The presentation made in this work focuses only on the main aspects of the FEM used in the YALES2BIO solver suite. The reader is referred to the work of [145, 146] for a more complete description of the method.

2.4.1.1 Continuous Field Representation

FEM is based on the discretization of the continuous domain Ω into a finite number of subdomains. Ω is then approximated by a finite number of nodes $\mathbf{x}_i$ and elements Ω^e which form the mesh. The field of interest, taken as an example, is the structural displacement. To determine the displacement on this mesh and inside each element, it is approximated by interpolation functions and field values at the element nodes $\mathbf{u}_a$. The displacement $\mathbf{u}$ inside an element is then approximated as $\hat{\mathbf{u}}$:

$$\mathbf{u} \approx \hat{\mathbf{u}} = \sum_{a=1}^{n} \mathbf{N}_a \mathbf{u}_a^e \tag{2.23}$$

$\mathbf{N}_a$ are the so-called shape functions. Great care must be taken to choose the shape functions to provide an appropriate approximation of the displacement. They must satisfy:

$$\mathbf{N}_a(\mathbf{x}_b) = \delta_{ab}\mathbf{I} \tag{2.24}$$

where $\mathbf{I}$ is the identity matrix. In this work, only linear elements are used, such as 3-node triangles and 4-node tetrahedra. The next section presents the shape functions used in these elements.

2.4.1.2 Area Coordinates

The shape functions are expressed in terms of the area coordinate system in the reference frame of the element. This new set of coordinates, L_1, L_2, and L_3 for a triangle with vertices 1, 2, 3 (Figure 2.3), follows a linear relation between these and the Cartesian system:

$$x = L_1 x_1 + L_2 x_2 + L_3 x_3 \tag{2.25a}$$
$$y = L_1 y_1 + L_2 y_2 + L_3 y_3 \tag{2.25b}$$
$$1 = L_1 + L_2 + L_3 \tag{2.25c}$$

At point 1, $L_1 = 1$ and $L_2 = L_3 = 0$. They can also be seen as the area formed by the point A_{P23} relative to the area of the triangle A_{123}, and so on for L_2 and L_3. In

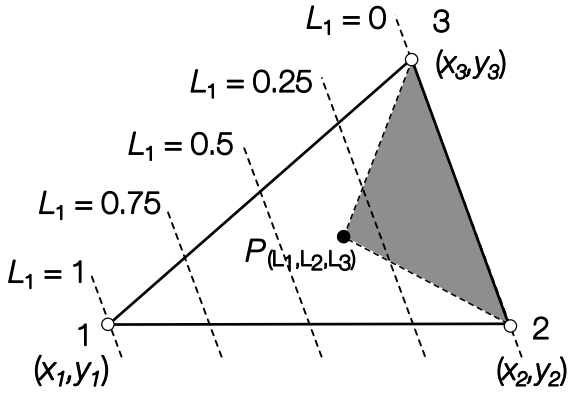

Figure 2.3: Area coordinate system in a 2D triangle element.

global coordinates, the area coordinates are then:

$$A_{123} = \frac{1}{2}\left[(x_2 - x_1)(y_3 - y_1) - (x_3 - x_1)(y_2 - y_1)\right] \tag{2.26a}$$
$$L_1 = \frac{1}{2A_{123}}\left[(x_2 - x_P)(y_3 - y_P) - (x_3 - x_P)(y_2 - y_P)\right] \tag{2.26b}$$
$$L_2 = \frac{1}{2A_{123}}\left[(x_3 - x_P)(y_2 - y_P) - (x_2 - x_P)(y_3 - y_P)\right] \tag{2.26c}$$
$$L_3 = 1 - L_1 - L_2 \tag{2.26d}$$

2.4.1.3 Shape Functions

The shape functions are then expressed in terms of the area coordinates. For a 3-node triangle, the shape functions are simply the area coordinates:

$$N_1 = L_1 \qquad N_2 = L_2 \qquad N_3 = L_3 \tag{2.27}$$

Equation (2.25c) allows us to express L_1 in terms of L_2 and L_3. The shape functions are then:

$$N_1 = 1 - L_2 - L_3 \qquad N_2 = L_2 \qquad N_3 = L_3 \tag{2.28}$$

These can be easily extended to a 4-node tetrahedron giving the following:

$$N_1 = 1 - L_2 - L_3 - L_4 \qquad N_2 = L_2 \qquad N_3 = L_3 \qquad N_4 = L_4 \tag{2.29}$$

Each individually gives a value of 1 at one node and 0 at the others, and varies linearly everywhere. The shape functions are then used to interpolate the displacement field inside the element.

2.4.1.4 Gaussian Quadrature

The integrals over the element are computed using Gaussian quadrature. The integral I of a function f over the element in terms of area coordinates is then approximated as:

$$I = \int_0^1 \int_0^{1-L_1} f(L_1, L_2, L_3)\, \mathrm{d}L_2\, \mathrm{d}L_1 \qquad \text{with } L_3 = 1 - L_1 - L_2 \tag{2.30}$$

The function f is evaluated at the Gaussian points, and I becomes the sum of f evaluated at these points:

$$I = \sum_{i=1}^{n} f(L_1^i, L_2^i, L_3^i) W_i \tag{2.31}$$

where W_i are the weights of the quadrature. The number of points n is chosen according to the order of the quadrature. The placement for the 3-node triangle and 4-node tetrahedron are given in Table 2.1.

Table 2.1: Gaussian quadrature points, positions, and weights for 3-node triangles and 4-node tetrahedra. $\alpha = (5 - \sqrt{5})/20$ and $\beta = (5 + 3\sqrt{5})/20$.

2D Triangle			
Points	L_1	L_2	Weights
a	0.5	0.5	1/3
b	0.5	0	1/3
c	0	0.5	1/3

3D Tetrahedron				
Points	L_1	L_2	L_3	Weights
a	α	α	α	1/24
b	α	α	β	1/24
b	α	β	α	1/24
c	β	α	α	1/24

In the following, we shall introduce the main concepts used in the FEM formulation for the structural problem. The biological tissues forming the leaflets and the vein wall are subjected to large deformations leading to non-linear behavior. Basics and notations of solid mechanics with a linear elasticity problem are first presented. Next, we will transition to the non-linear case and its implementation in the YALES2BIO solver suite.

2.4.2 Linear elasticity

Let's consider a solid Ω delimited by its boundary Γ_Ω (Figure 2.5). In this section we will present the linear elasticity problem to introduce the FEM formulation of a structural analysis problem.

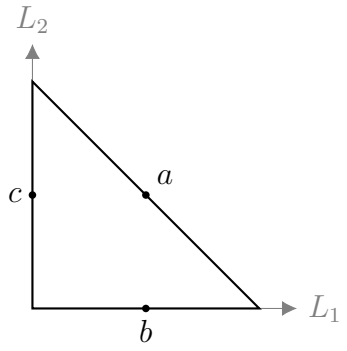

Figure 2.4: Gaussian quadrature points for a 2D triangle.

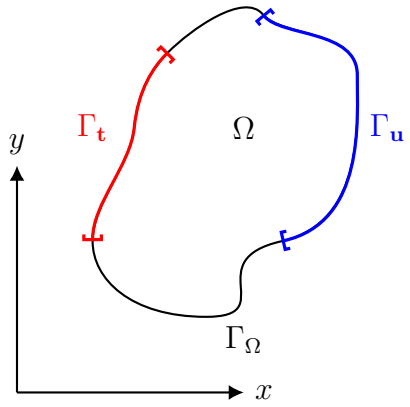

Figure 2.5: 2D solid Ω and its boundary Γ_Ω.

2.4.2.1 Coordinates and displacement

Let's consider a fixed Cartesian coordinate system with associated unit base vectors $\mathbf{e}_i$. The vector of coordinates is then $\mathbf{x} = x_i\mathbf{e}_i$ using the Einstein summation convention. Similarly, the displacement vector is $\mathbf{u} = u_i\mathbf{e}_i$. Is is defined as the difference between the current position and the initial position of a point in the solid. In the following, all quantities will be expressed by their components in the Cartesian coordinate system.

2.4.2.2 Strain-displacement relation

The following convention will often be used for the derivatives:

$$\frac{\partial u_i}{\partial x_j} = u_{i,j}$$

The strain tensor ε is defined as the symmetric part of the displacement field gradient:

$$\varepsilon_{ij} = \frac{1}{2}\left(u_{i,j} + u_{j,i}\right) \tag{2.32}$$

This relation provides valid measures of the deformation of the solid as long as the deformation is small, in other words:

$$\|\varepsilon_{ij}\| \ll 1 \quad \text{and} \quad \|\omega_{ij}^2\| \ll \|\varepsilon_{ij}\| \tag{2.33}$$

where ω_{ij} is a small rotation, defined as the antisymmetric part of the displacement field gradient:

$$\omega_{ij} = \frac{1}{2}\left(u_{i,j} - u_{j,i}\right) \tag{2.34}$$

The displacement gradient can be expressed in terms of the strain tensor and the rotation tensor:

$$u_{i,j} = \varepsilon_{ij} + \omega_{ij} \tag{2.35}$$

2.4.2.3 Balance of momentum and constitutive relation: strong form

Newton's second law of motion for a continuous medium is expressed as the momentum balance equation:

$$\rho\ddot{u}_i + \sigma_{ij,j} = b_i \tag{2.36}$$

where σ_{ij} is the stress tensor, ρ the density and b_i the body forces. $\ddot{u}_i$ corresponds to the second time derivative of the displacement or the acceleration. The stress tensor in the following is symmetric, meaning that $\sigma_{ij} = \sigma_{ji}$. The constitutive relation between the stress and the strain is given by Hooke's law:

$$\sigma_{ij}(t) = C_{ijkl}\varepsilon_{kl}(t) \tag{2.37}$$

where C_{ijkl} are elastic moduli of the material. As Equation (2.37) is linear, the elastic moduli are constant and do not depend on the strain. The stress varies linearly with the strain, meaning we can drop the explicit inclusion of time.

2.4.2.4 Boundary conditions

Two types of boundary conditions are used here. The first type is a Dirichlet boundary condition, where the displacement is imposed on a part of the boundary $\Gamma_{\mathbf{u}}$:

$$u_i = \bar{u}_i \tag{2.38}$$

All quantities noted with a bar are imposed values. The second type is a Neumann boundary condition, where the traction is imposed on $\Gamma_{\mathbf{t}}$:

$$t_i = \sigma_{ij}n_j = \bar{t}_i \tag{2.39}$$

where n_j is the normal vector to the boundary. Later, this boundary condition will be extended to the fluid forces applied on the solid where a tangential component due to shear stress is added.

2.4.2.5 Matrix notations

In the following we will often use the matrix form of the equations seen above to simplify the notation. In the three-dimensionnal case, the stress and strain tensor can be expressed as a 6×1 vector:

$$\begin{aligned} \boldsymbol{\sigma} &= \begin{bmatrix} \sigma_{11} & \sigma_{22} & \sigma_{33} & \sigma_{12} & \sigma_{23} & \sigma_{31} \end{bmatrix}^T \qquad \text{with} \quad \sigma_{ij} = \sigma_{ji} \\ \boldsymbol{\varepsilon} &= \begin{bmatrix} \varepsilon_{11} & \varepsilon_{22} & \varepsilon_{33} & 2\varepsilon_{12} & 2\varepsilon_{23} & 2\varepsilon_{31} \end{bmatrix}^T \qquad \text{with} \quad \varepsilon_{ij} = \varepsilon_{ji} \end{aligned} \tag{2.40}$$

The strain-displacement relation in matrix notation becomes:

$$\boldsymbol{\varepsilon} = \mathbb{B}\mathbf{u} \tag{2.41}$$

where $\mathbb{B}$ is the 3D strain operator given by:

$$\mathbb{B}^T = \begin{bmatrix} \dfrac{\partial}{\partial x_1} & 0 & 0 & \dfrac{\partial}{\partial x_2} & 0 & \dfrac{\partial}{\partial x_3} \\ 0 & \dfrac{\partial}{\partial x_2} & 0 & \dfrac{\partial}{\partial x_1} & \dfrac{\partial}{\partial x_3} & 0 \\ 0 & 0 & \dfrac{\partial}{\partial x_3} & 0 & \dfrac{\partial}{\partial x_2} & \dfrac{\partial}{\partial x_1} \end{bmatrix} \tag{2.42}$$

This operator is used to write the linear momentum equation in Cartesian coordinates under its matrix form:

$$\rho\ddot{\mathbf{u}} + \mathbb{B}^T\boldsymbol{\sigma} = \mathbf{b} \tag{2.43}$$

The constitutive relation in matrix form is then:

$$\boldsymbol{\sigma} = \mathbf{D}\boldsymbol{\varepsilon} \tag{2.44}$$

where $\mathbf{D}$ is the 6×6 elasticity matrix, representing the elastic moduli of the material. It is a symmetric matrix. For an isotropic linear material:

$$\mathbf{D} = \frac{E}{(1+\nu)(1-2\nu)} \begin{bmatrix} 1-\nu & \nu & \nu & 0 & 0 & 0 \\ \nu & 1-\nu & \nu & 0 & 0 & 0 \\ \nu & \nu & 1-\nu & 0 & 0 & 0 \\ 0 & 0 & 0 & (1-2\nu)/2 & 0 & 0 \\ 0 & 0 & 0 & 0 & (1-2\nu)/2 & 0 \\ 0 & 0 & 0 & 0 & 0 & (1-2\nu)/2 \end{bmatrix} \tag{2.45}$$

where E is the Young's modulus and ν the Poisson's ratio. They are specific to the material taken into consideration. The linear momentum equation can then be written as:

$$\rho\ddot{\mathbf{u}} + \mathbb{B}^T\mathbf{D}\mathbb{B}\mathbf{u} = \mathbf{b} \tag{2.46}$$

2.4.2.6 FEM formulation of the linear problem

The ideas developed in Section 2.4.1 lead to discretize Ω by a finite number of elements:

$$\Omega \approx \hat{\Omega} = \sum_e \Omega^e \tag{2.47}$$

as well as its boundary Γ_Ω:

$$\Gamma_\Omega \approx \hat{\Gamma}_\Omega = \sum_e \Gamma_\Omega^e \tag{2.48}$$

Ω^e and Γ_Ω^e are the interior and the boundary elements. The objective now is to express the linear momentum equation 2.46 on the approximated domain $\hat{\Omega}$ and its boundary $\hat{\Gamma}_\Omega$. Using the Galerkin method the problem becomes:

$$\begin{aligned} \mathrm{G}_{eq} \approx \hat{\mathrm{G}}_{eq} =& \sum_e \left[\int_{\Omega^e} \delta\mathbf{u}^T \rho \ddot{\mathbf{u}} \mathrm{d}\Omega^e + \int_{\Omega^e} \delta\mathbf{u}^T \mathbb{B}^T \mathbf{D} \mathbb{B} \mathbf{u} \mathrm{d}\Omega^e - \int_{\Omega^e} \delta\mathbf{u}^T \mathbf{b} \mathrm{d}\Omega^e \right] \\ & - \sum_{et} \left[\int_{\Gamma_{et}} \delta\mathbf{u}^T \bar{\mathbf{t}} \mathrm{d}\Gamma_{et} \right] = 0 \\ =& \sum_e \hat{\mathrm{G}}^e + \sum_{et} \hat{\mathrm{G}}_t^e = 0 \end{aligned} \tag{2.49}$$

where $\delta\mathbf{u}$ is the virtual displacement, $\hat{\mathrm{G}}^e$ and $\hat{\mathrm{G}}_t^e$ are terms within the domain Ω^e of each element or those which belong to the traction boundary surface Γ_{et} respectively. The first term of Equation (2.49) is the inertial force, the second term is the internal force, the third term is the volumetric force and the last the external load. The problem is then to find the displacement field $\mathbf{u}$ that satisfies the variational form in Equation (2.49). The displacement field is then approximated by the shape functions as in Equation (2.23):

$$\mathbf{u}(\mathbf{x}, t) \approx \hat{\mathbf{u}} = \sum_{a=1}^{n} N_a(\mathbf{x}) \tilde{\mathbf{u}}_a(t) = \mathbf{N}(\mathbf{x}) \tilde{\mathbf{u}}(t) \tag{2.50}$$

where $\tilde{\mathbf{u}}_a$ are the nodal displacements and $\mathbf{N}(\mathbf{x})$ is the matrix of shape functions. This expression can be written in terms of area coordinates with $\mathbf{L}$ the area coordinates vector:

$$\mathbf{u}(\mathbf{L}, t) \approx \hat{\mathbf{u}} = \mathbf{N}(\mathbf{L}) \tilde{\mathbf{u}}(t) \tag{2.51}$$

The virtual displacement is then approximated in the same way:

$$\delta\mathbf{u}(\mathbf{x}, t) \approx \hat{\delta\mathbf{u}} = \sum_{a=1}^{n} N_a(\mathbf{x}) \delta\tilde{\mathbf{u}}_a(t) = \mathbf{N}(\mathbf{x}) \delta\tilde{\mathbf{u}}(t) \tag{2.52}$$

We also need the displacement gradient as it appears in Equation (2.49), meaning that we have to compute the shape function gradient. The shape functions gradient relation is then in matrix form:

$$\frac{\partial N_a}{\partial \mathbf{L}} = \mathbf{J}^{-1} \frac{\partial N_a}{\partial \mathbf{x}} \tag{2.53}$$

where:

$$\frac{\partial N_a}{\partial \mathbf{L}} = \begin{Bmatrix} N_{a,L_1} \\ N_{a,L_2} \\ N_{a,L_3} \end{Bmatrix}, \quad \frac{\partial N_a}{\partial \mathbf{x}} = \begin{Bmatrix} N_{a,x_1} \\ N_{a,x_2} \\ N_{a,x_3} \end{Bmatrix}, \quad \mathbf{J} = \frac{\partial \mathbf{x}}{\partial \mathbf{L}} = \begin{bmatrix} x_{1,L_1} & x_{2,L_1} & x_{3,L_1} \\ x_{1,L_2} & x_{2,L_2} & x_{3,L_2} \\ x_{1,L_3} & x_{2,L_3} & x_{3,L_3} \end{bmatrix} \tag{2.54}$$

J is the Jacobian matrix of the transformation from the area coordinates to the Cartesian coordinates. Using Equation (2.50) in Equation (2.41), the strain tensor can be expressed as:

$$\boldsymbol{\varepsilon} = \mathbb{B}\mathbf{u} \approx \sum_a (\mathbb{B}N_a)\tilde{\mathbf{u}}_a = \sum_a \mathbf{B}_a \tilde{\mathbf{u}}_a = \begin{bmatrix}\mathbf{B}_1 & \mathbf{B}_2 & \dots\end{bmatrix} \begin{Bmatrix}\tilde{\mathbf{u}}_1 \\ \tilde{\mathbf{u}}_2 \\ \vdots\end{Bmatrix} = \mathbf{B}\tilde{\mathbf{u}} \tag{2.55}$$

where $\mathbf{B}_a = \mathbb{B}N_a$ the strain operator at each node of the element:

$$\mathbf{B}_a^T = \begin{bmatrix} N_{a,x_1} & 0 & 0 & N_{a,x_2} & 0 & N_{a,x_3} \\ 0 & N_{a,x_2} & 0 & N_{a,x_1} & N_{a,x_3} & 0 \\ 0 & 0 & N_{a,x_3} & 0 & N_{a,x_2} & N_{a,x_1} \end{bmatrix} \tag{2.56}$$

$\hat{\mathrm{G}}^e$ and $\hat{\mathrm{G}}_t^e$ terms from Equation (2.49) can be formulated for a single element:

$$\begin{aligned} \hat{\mathrm{G}}^e =& \delta\tilde{\mathbf{u}}^T \left[\int_{\Omega^e} \mathbf{N}^T \rho \mathbf{N} \mathrm{d}\Omega^e \ddot{\tilde{\mathbf{u}}} + \int_{\Omega^e} \mathbf{B}^T \mathbf{D}\mathbf{B} \mathrm{d}\Omega^e \tilde{\mathbf{u}} - \int_{\Omega^e} \mathbf{N}^T \mathbf{b} \mathrm{d}\Omega^e \right] \\ \hat{\mathrm{G}}_t^e =& -\delta\tilde{\mathbf{u}}^T \int_{\Gamma_{\mathbf{t}}^e} \mathbf{N}^T \bar{\mathbf{t}} \mathrm{d}\Gamma_{\mathbf{t}}^e \end{aligned} \tag{2.57}$$

The physical meaning of each term of Equation (2.57) are:

1. $\int_{\Omega^e} \mathbf{N}^T \rho \mathbf{N} \mathrm{d}\Omega \ddot{\tilde{\mathbf{u}}}$ is the inertial force acting on the element. $\int_{\Omega^e} \mathbf{N}^T \rho \mathbf{N} \mathrm{d}\Omega$ is the mass matrix of the element and will be noted $\mathbf{M}^e$.
2. $\int_{\Omega^e} \mathbf{B}^T \mathbf{D}\mathbf{B} \mathrm{d}\Omega \tilde{\mathbf{u}}$ is the internal force acting on the element as well. $\int_{\Omega^e} \mathbf{B}^T \mathbf{D}\mathbf{B} \mathrm{d}\Omega$ is the stiffness matrix of the element and will be noted $\mathbf{K}^e$.
3. $\int_{\Gamma_\Omega^e} \mathbf{N}^T \mathbf{b} \mathrm{d}\Gamma_\Omega$ is the external force acting on the element boundaries. It is the equivalent of the traction force acting on the element boundaries.

The sum over all the elements is performed to obtain the discrete linear momentum equation. The global mass and stiffness matrices are then obtained by assembling the mass and stiffness matrices of each element. Concerning the virtual displacement $\delta\mathbf{u}^T$, as they are completely arbitrary in this case, one can drop then. The global linear momentum equation becomes the following set of ordinary differential equations:

$$\mathbf{M}\ddot{\tilde{\mathbf{u}}} + \mathbf{K}\tilde{\mathbf{u}} = \mathbf{f} \tag{2.58}$$

where:

$$\mathbf{M} = \sum_e \mathbf{M}^e \,, \quad \mathbf{K} = \sum_e \mathbf{K}^e \,, \quad \mathbf{f} = \sum_e \mathbf{f}^e \tag{2.59}$$

Equation (2.58) is the non-viscous formulation of the balance momentum Equation (2.22). From this point, we will introduce the non-linear elasticity problem and its FEM formulation in the next section.

2.4.3 Geometrically non-linear Problem

2.4.3.1 Reference and Current Frame

In Section 2.4.2, the stress depends only on the deformation from the initial state of the solid Ω, which is referred to as the *reference configuration*. Additionally, shape functions were computed and integrated in the reference configuration. In the non-linear case, the deformation is large, and the stress depends on the deformation from the *current configuration* of the solid, denoted as ω. The two configurations are illustrated in Figure 2.6.

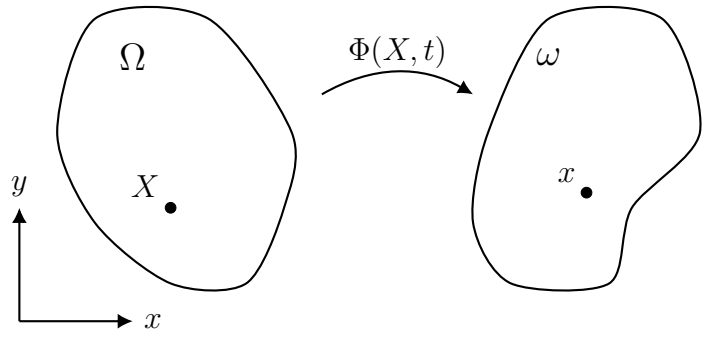

Figure 2.6: Reference and current configuration of the solid.

2.4.3.2 Deformation Gradient

In the following, uppercase letters will refer to the reference configuration, and lowercase letters will refer to the current configuration. To change from the reference coordinates to the current coordinates, the displacement vector is used:

$$\mathbf{x} = \Phi(\mathbf{X}, t) = \mathbf{X} + \mathbf{u}(\mathbf{X}, t) \tag{2.60}$$

$\Phi(\mathbf{X}, t)$ is the deformation of the solid from the reference configuration to the current configuration. The deformation gradient tensor $\mathbf{F}$ is then defined as:

$$\mathbf{F} = \frac{\partial \mathbf{x}}{\partial \mathbf{X}} = \mathbf{Id} + \nabla \mathbf{u} \tag{2.61}$$

where $\nabla \mathbf{u}$ is the displacement gradient tensor. $\mathbf{F}$ contains information about both the *strain* and the rigid motion of the solid. The strain is defined as the deformation excluding the rigid motion. The strain gradient tensor $\mathbf{C}$ is then defined as:

$$\mathbf{C} = \mathbf{F}^T\mathbf{F} = \mathbf{Id} + \nabla \mathbf{u} + \nabla \mathbf{u}^T + \nabla \mathbf{u}^T \nabla \mathbf{u} \tag{2.62}$$

To eliminate $\mathbf{Id}$, we define the Green-Lagrange strain tensor $\mathbf{E}$ as:

$$\mathbf{E} = \frac{1}{2}(\mathbf{C} - \mathbf{Id}) = \frac{1}{2}(\nabla \mathbf{u} + \nabla \mathbf{u}^T + \nabla \mathbf{u}^T \nabla \mathbf{u}) \tag{2.63}$$

Comparing Equation (2.63) to the small strain tensor in Equation (2.32), we observe that the Green-Lagrange strain tensor is an extension of the small strain tensor to

the large deformation case, incorporating the non-linear term $\nabla \mathbf{u}^T \nabla \mathbf{u}$. The non-linear 3D strain operator $\hat{\mathbf{B}}_a$ becomes, using Equation (2.56):

$$\hat{\mathbf{B}}_a = \mathbf{B}_a + \mathbf{B}_a^{NL} \tag{2.64}$$

where:

$$\mathbf{B}_a^{NL} = \begin{bmatrix} u_{1,1}N_{a,1} & u_{2,1}N_{a,1} & u_{3,1}N_{a,1} \\ u_{1,2}N_{a,2} & u_{2,2}N_{a,2} & u_{3,2}N_{a,2} \\ u_{1,3}N_{a,3} & u_{2,3}N_{a,3} & u_{3,3}N_{a,3} \\ u_{1,1}N_{a,2} + u_{1,2}N_{a,1} & u_{2,1}N_{a,2} + u_{2,2}N_{a,1} & u_{3,1}N_{a,2} + u_{3,2}N_{a,1} \\ u_{1,2}N_{a,3} + u_{1,3}N_{a,2} & u_{2,2}N_{a,3} + u_{2,3}N_{a,2} & u_{3,2}N_{a,3} + u_{3,3}N_{a,2} \\ u_{1,3}N_{a,1} + u_{1,1}N_{a,3} & u_{2,3}N_{a,1} + u_{2,1}N_{a,3} & u_{3,3}N_{a,1} + u_{3,1}N_{a,3} \end{bmatrix} \tag{2.65}$$

2.4.3.3 Hyperelastic Material

In the hyperelastic framework, stress is expressed as the derivative of a strain energy density function W with respect to the Green strain tensor $\mathbf{E}$:

$$\mathbf{S} = \frac{\partial W}{\partial \mathbf{E}} = \frac{\partial W}{\partial \mathbf{C}} \frac{\partial \mathbf{C}}{\partial \mathbf{E}} = 2\frac{\partial W}{\partial \mathbf{C}} \tag{2.66}$$

where $\mathbf{S}$ is the second Piola-Kirchhoff stress tensor, or the stress tensor in the reference configuration. The strain energy density function W depends on the Green-Lagrange strain tensor $\mathbf{E}$ and measures the energy stored in the solid due to deformation. The constitutive relation between stress and strain is then:

$$S_{IJ} = \mathbb{C}_{IJKL} E_{KL} \quad \text{with} \quad \mathbb{C}_{IJKL} = 4\frac{\partial^2 W}{\partial C_{IJ} \partial C_{KL}} \tag{2.67}$$

where $\mathbb{C}_{IJKL}$ is the fourth-order elasticity tensor and has the same form as the elasticity matrix $\mathbf{D}$ in Equation (2.45). To express the relation between the stress $\mathbf{S}$ and the pure strain $\mathbf{C}$, derivatives of W are necessary. Instead of deriving directly with respect to $\mathbf{C}$, the first, second, and third invariants of the isochoric strain tensor $\hat{\mathbf{C}} = J^{-2/3}\mathbf{C}$ are used, where J is the determinant of the deformation gradient. The invariants of $\mathbf{C}$ are defined as:

$$\begin{aligned} \hat{I}_1 &= J^{-2/3}\mathrm{tr}(\mathbf{C}) \\ \hat{I}_2 &= J^{-4/3}\frac{1}{2}\left[\mathrm{tr}(\mathbf{C})^2 - \mathrm{tr}(\mathbf{C}^2)\right] \\ \hat{I}_3 &= \det(\mathbf{C}) = J^2 \end{aligned} \tag{2.68}$$

We will use J as the third invariant. The derivatives with respect to C_{IJ} are:

$$\begin{bmatrix} \frac{\partial \hat{I}_1}{\partial C_{IJ}} \\ \frac{\partial \hat{I}_2}{\partial C_{IJ}} \\ \frac{\partial J}{\partial C_{IJ}} \end{bmatrix} = \begin{bmatrix} J^{-2/3}\delta_{IJ} \\ J^{-4/3}\frac{1}{2}(\delta_{IJ}I_1 - C_{IJ}) \\ \frac{1}{2}JC_{IJ}^{-1} \end{bmatrix} \tag{2.69}$$

W can then be expressed as a function of the invariants: $W = W(\hat{I}_1, \hat{I}_2, J)$. The stress tensor $\mathbf{S}$ is then expressed as:

$$\begin{aligned}\mathbf{S} &= 2\left[\frac{\partial W}{\partial \hat{I}_1}\frac{\partial \hat{I}_1}{\partial C_{IJ}} + \frac{\partial W}{\partial \hat{I}_2}\frac{\partial \hat{I}_2}{\partial C_{IJ}} + \frac{\partial W}{\partial J}\frac{\partial J}{\partial C_{IJ}}\right] \\ &= 2\begin{bmatrix} J^{-2/3}\delta_{IJ} & J^{-4/3}\frac{1}{2}(\delta_{IJ}I_1 - C_{IJ}) & \frac{1}{2}JC^{-1}_{IJ}\end{bmatrix}\begin{bmatrix}\frac{\partial W}{\partial \hat{I}_1}\\ \frac{\partial W}{\partial \hat{I}_2}\\ \frac{\partial W}{\partial J}\end{bmatrix}\end{aligned} \tag{2.70}$$

The elasticity tensor terms are expressed as:

$$\begin{aligned}\mathbb{C}_{IJKL} = 4&\begin{bmatrix} J^{-2/3}\delta_{IJ} & J^{-4/3}(I_1\delta_{IJ} - C_{IJ}) & \frac{1}{2}JC^{-1}_{IJ}\end{bmatrix} \\ &\times\begin{bmatrix}\frac{\partial^2 W}{\partial \hat{I}_1{}^2} & \frac{\partial^2 W}{\partial \hat{I}_1 \partial \hat{I}_2} & \frac{\partial^2 W}{\partial \hat{I}_1 \partial J}\\ \frac{\partial^2 W}{\partial \hat{I}_2 \partial \hat{I}_1} & \frac{\partial^2 W}{\partial \hat{I}_2{}^2} & \frac{\partial^2 W}{\partial \hat{I}_2 \partial J}\\ \frac{\partial^2 W}{\partial J \partial \hat{I}_1} & \frac{\partial^2 W}{\partial J \partial \hat{I}_2} & \frac{\partial^2 W}{\partial J^2}\end{bmatrix}\begin{bmatrix} J^{-2/3}\delta_{KL} \\ J^{-4/3}(I_1\delta_{KL} - C_{KL}) \\ \frac{1}{2}JC^{-1}_{KL}\end{bmatrix} \\ &+ 4\begin{bmatrix}\frac{\partial W}{\partial \hat{I}_2} & \frac{\partial W}{\partial J}\end{bmatrix}\begin{bmatrix} J^{-4/3}\left(\delta_{IJ}\delta_{KL} - \frac{1}{2}(\delta_{IK}\delta_{JL} + \delta_{IL}\delta_{JK})\right) \\ J(C^{-1}_{IJ}C^{-1}_{KL} - 2\mathbb{C}^{-1}_{IJKL})\end{bmatrix}\end{aligned} \tag{2.71}$$

with:

$$\mathbb{C}^{-1}_{IJKL} = \frac{1}{2}\left[C^{-1}_{IK}C^{-1}_{JL} + C^{-1}_{IL}C^{-1}_{JK}\right] \tag{2.72}$$

The strain energy density function W is required to compute all the components listed above. The elasticity tensor $\mathbb{C}_{IJKL}$ will be denoted as $\hat{\mathbf{D}}$ to maintain the notation introduced in Section 2.4.2.6. In this work, a neo-Hookean material model is used:

$$W = G(\hat{I}_1 - 3) + K(J^2 - 1) \tag{2.73}$$

where G is the shear modulus, and K is the bulk modulus. The shear and bulk moduli are related to the Young's modulus E and the Poisson's ratio ν by:

$$\begin{aligned} G &= \frac{E}{2(1+\nu)} \\ K &= \frac{E}{3(1-2\nu)}\end{aligned} \tag{2.74}$$

To understand what a geometrically non-linear problem implies computationally, we will now describe the FEM formulation of the stationary non-linear problem.

2.4.3.4 Stationary Non-linear Problem

The linear momentum equation in Equation (2.58) in the stationary case is taken as a starting point to express the stationary non-linear problem. With the inertial term dropped, Equation (2.58) is simplified to:

$$\mathbf{Ku} = \mathbf{f} \tag{2.75}$$

In the non-linear case, the stress term $\mathbf{Ku}$ depends on the deformation of Ω. In the reference frame Equation (2.75) becomes:

$$\int_{\Omega} \hat{\mathbf{B}}^T \mathbf{S} \mathrm{d}\Omega = \mathbf{f} \tag{2.76}$$

This problem can be seen as a function to minimize. Therefore, the residual of Equation (2.76) is introduced:

$$\mathbf{\Psi}(\mathbf{u}) = \mathbf{f} - \mathbf{Ku} \tag{2.77}$$

and the Newton-Raphson method is used. This requires computation of the first-order Taylor expansion of Equation (2.77) which is expressed as:

$$\mathbf{\Psi}(\mathbf{u}^{i+1}) \approx \mathbf{\Psi}(\mathbf{u^i}) + \left(\frac{\partial \mathbf{\Psi}}{\partial \mathbf{u}}\right)^i \delta\mathbf{u} = 0 \tag{2.78}$$

where $\mathbf{u}^{i+1}$ is the solution at the $(i+1)^{th}$ iteration, $\mathbf{u}^i$ is the solution at the i^{th} iteration, and $\delta\mathbf{u}$ is the increment of the solution. Solving one Newton-Raphson iteration is equivalent to solving the following linear system:

$$\mathbf{\Psi}(\mathbf{u}^i) = -\left(\frac{\partial \mathbf{\Psi}}{\partial \mathbf{u}}\right)^i \delta\mathbf{u} \tag{2.79}$$

To solve this equation, the derivative of the residual with respect to the displacement field is needed. The derivative of the residual is defined as the tangent stiffness matrix $\mathbf{K_T}$ with the iteration subscript i dropped:

$$\mathbf{K_T} = -\frac{\partial \mathbf{\Psi}}{\partial \mathbf{u}} \tag{2.80a}$$

$$\mathbf{K_T} = \int_{\Omega} \hat{\mathbf{B}}^T \hat{\mathbf{D}}_\mathbf{T} \hat{\mathbf{B}} \mathrm{d}\Omega + \int_{\Omega} \frac{\partial \hat{\mathbf{B}}^T}{\partial \mathbf{u}} \mathbf{S} \mathrm{d}\Omega - \frac{\partial \mathbf{f}}{\partial \mathbf{u}} \tag{2.80b}$$

$$\mathbf{K_T} = \mathbf{K_M} + \mathbf{K_G} + \mathbf{K_L} \tag{2.80c}$$

The first term in Equation (2.80b) is the material stiffness matrix $\mathbf{K_M}$, and the third term is the load stiffness matrix $\mathbf{K_L}$. The material stiffness matrix has the same form as the stiffness matrix in Equation (2.57). $\hat{\mathbf{D}}_\mathbf{T}$ is computed at every Newton iteration as it is the second derivative of the neo-Hookean strain energy density function W. The second term is the geometric stiffness matrix $\mathbf{K_G}$ which

arises from the nonlinear form of the strain-displacement equations. Its expression can be easily constructed from the indicial form:

$$\mathbf{K}_{\mathbf{G}}^{ab} = \int_{\Omega} \frac{\partial \hat{\mathbf{B}}^T}{\partial \mathbf{u}} \mathbf{S} \mathrm{d}\Omega = \quad = \left[\int_{\Omega} \mathbf{N}_a \mathbf{S} \mathbf{N}_b \mathrm{d}\Omega \right] \times \mathbf{Id} \tag{2.81}$$

The third term, the load stiffness matrix $\mathbf{K_G}$, arises from forces dependent on boundary deformation, e.g. following forces like pressure. The computation of this term typically results in an asymmetric matrix [146, p. 174], which complicates solving the linear system using a Preconditioned Conjugate Gradient (PCG) method. Therefore, since forces $\mathbf{f}^i$ are updated at each Newton iteration, the load stiffness matrix can be dropped. The process is repeated until the convergence criterion ϵ_n is reached, i.e., $||\mathbf{\Psi}^{i+1}||_\infty \leq \epsilon_n$.

2.4.4 Transient Non-linear Problem

In this section, we define the complete set of equations for the transient non-linear problem. Since the problem depends on time, a time discretization must be defined. The Newmark scheme is employed to discretize the problem in time, and we will discuss how it modifies the Newton-Raphson iteration computation. In the following, tildes are omitted for the sake of notational simplicity.

2.4.4.1 Generalities

Equation (2.58) is again taken as basis to express the transient problem in the non-linear case. Numerical damping is introduced into the equation to stabilize the system. Rayleigh damping is used [147, 148], and the equation becomes:

$$\mathbf{M}\ddot{\mathbf{u}} + \mathbf{C}\dot{\mathbf{u}} + \mathbf{K}\mathbf{u} = \mathbf{f} \tag{2.82}$$

where $\mathbf{C}$ is the damping matrix, defined as:

$$\mathbf{C} = \alpha_m \mathbf{M} + \alpha_k \mathbf{K} \tag{2.83}$$

Here, α_m and α_k are the mass and stiffness damping coefficients, respectively. These are user-defined parameters. Since $\mathbf{K}$ exhibits non-linear behavior, the damping matrix varies in time. Various strategies can be employed to compute the damping matrix: it can be computed at the beginning of the simulation and either kept constant, updated at each time step, or updated at each Newton-Raphson iteration. In this work, the second strategy is used.

2.4.4.2 Newmark Scheme

The Newmark scheme is widely used to discretize dynamic problems in time. It belongs to a family of implicit time integration methods. The Newmark scheme expresses the velocity $\dot{\mathbf{u}}_{n+1}$ and acceleration $\ddot{\mathbf{u}}_{n+1}$ as:

$$\dot{\mathbf{u}}_{n+1} = a_1(\mathbf{u}_{n+1} - \mathbf{u}_n) + a_4\dot{\mathbf{u}}_n + a_5\ddot{\mathbf{u}}_n \tag{2.84a}$$

$$\ddot{\mathbf{u}}_{n+1} = a_0(\mathbf{u}_{n+1} - \mathbf{u}_n) + a_2\dot{\mathbf{u}}_n + a_3\ddot{\mathbf{u}}_n \tag{2.84b}$$

where:

$$\begin{aligned} a_0 &= \frac{1}{\alpha \Delta t^2}, \quad a_4 = \frac{\delta}{\alpha} - 1, \quad a_5 = \frac{\Delta t}{2}\left(\frac{\delta}{\alpha} - 2\right) \\ a_1 &= \frac{\delta}{\alpha \Delta t}, \quad a_2 = \frac{1}{\alpha \Delta t}, \quad a_3 = \frac{1}{2\alpha} - 1 \end{aligned} \tag{2.85}$$

Here, α and δ are the Newmark parameters, where δ controls numerical dissipation. To ensure unconditional stability, the following condition must be satisfied:

$$\begin{aligned} \delta &\geq \frac{1}{2}, \\ \alpha &\geq \frac{1}{4}\left(\frac{1}{2} + \delta\right)^2. \end{aligned} \tag{2.86}$$

In this work, we follow the ANSYS implementation of the Newmark scheme by introducing the amplitude decay factor γ:

$$\begin{aligned} \delta &= \frac{1}{2} + \gamma, \\ \alpha &= \frac{1}{4}\left(\frac{1}{2} + \delta\right)^2, \\ \gamma &\geq 0. \end{aligned} \tag{2.87}$$

When $\gamma = 0$, the Newmark scheme becomes the average acceleration method, meaning no numerical damping is applied.

We can now express the transient non-linear problem. The non-linear momentum equation in Equation (2.82) leads to the residual $\mathbf{\Psi}^i_{n+1}$:

$$\mathbf{\Psi}^i_{n+1} = \mathbf{f}^i_{n+1} - \mathbf{M}\ddot{\mathbf{u}}_{n+1} - \mathbf{C}\dot{\mathbf{u}}_{n+1} - \mathbf{K}\mathbf{u}_{n+1}. \tag{2.88}$$

In Equations (2.84a) and (2.84b), the term $\mathbf{u}_{n+1} - \mathbf{u}_n$ appears, which inside a Newton-Raphson iteration becomes the increment of the solution $\delta\mathbf{u}$. In $\dot{\mathbf{u}}_{n+1}$ and $\ddot{\mathbf{u}}_{n+1}$ expressions (Equation (2.84)), only the first term depends on the increment of displacement $\mathbf{u}_{n+1} - \mathbf{u}_n$. Therefore the derivative of the residual with respect to the displacement (see Equation (2.79)) can be expressed as:

$$-\left(\frac{\partial \mathbf{\Psi}}{\partial \mathbf{u}}\right)^i = \mathbf{K}^i_{\mathbf{T}} + a_0\mathbf{M}^i + a_1\mathbf{C}^i \tag{2.89}$$

The linear system to solve at each Newton-Raphson iteration becomes:

$$\left(\mathbf{K}^i_{\mathbf{T}} + a_0\mathbf{M}^i + a_1\mathbf{C}^i\right)\delta\mathbf{u}^i = \mathbf{\Psi}^i_{n+1}. \tag{2.90}$$

The methodology used to solve the solid transient non-linear problem has been provided. During this work, only linear tetrahedra have been used. Initially, quadratic tetrahedra were tested, but showed poor stability in FSI simulations. According to Zhang et al. [149], this instability was due to the original formulation of the shape functions of these elements, which could not handle high mesh distortion.

The contact procedure used in this work is then presented.

2.5 Contact methodology

2.5.1 Contact model

Leaflets are deformable bodies facing one another as described in Section 1.3.2. During opening and closing phases, contact may occur, and if it is not handle properly, leaflets can overlap one another in the simulation. With IBM methods, this problem does not affect the global stability of the method as the fluid interacts with the structures through source terms. However, in an FSI body-fitted method, as used in this work, the interface has to be defined at all time during the simulation. Overlapping in this case, as the elements in between cannot be suppressed, causes the fluid mesh elements to turn inside out. Numerically this corresponds to switching the ordering convention of the element nodes, causing miscalculation. To prevent this to happen, a contact method has to be employed. Different methods to compute contact between deformable bodies exist. Contact algorithms mainly work with a slave body contacting a master body. The penalty method consists in computing a contact force as a function of the penetration of the slave body into the master body [150–152]. The force is then applied to the nodes of the slave and master bodies. On one hand the penalty method is trivial to implement, and the resulting contact force is smooth, helping stabilization of the computation. On the other hand, the penalty method is not conservative, as the calculated contact force does not accurately reflect the true interaction forces. This can result in unrealistic behavior of the system if the penalty parameter is not carefully calibrated. The Lagrange multipliers method introduces additional degrees of freedom to enforce contact constraints between the slave and master bodies without penetration [153]. The Lagrange multiplier technique does not approximate the contact force but computes it directly by solving a system of equations that represent the contact constraints. This approach ensures the contact force remains physically realistic and adheres to the principle of conservation, as it directly enforces the no-penetration condition. The Lagrange multiplier method is more robust for problems where high accuracy in the contact force is necessary, such as in the analysis of friction, wear, and lubrication in tribological systems. However, its implementation is more complex and computationally demanding due to the need to solve an augmented system of equations that includes both the original equations of motion and the contact constraints. The reader is referred to [154, 155] for extensive reviews of contact methods.

The penalty method has been chosen in this work for different reasons. First is the simplicity of implementation. Second is the fact that the penalty method gives a smooth contact force leading to the minimization of discontinuities. The penalty method chosen for implementation does not compute directly the contact between the two leaflets. Instead, the symmetry of the leaflets is used to compute the contact between a deformable body and a rigid plane, which is the symmetry plane in between the leaflets (see Figure 3.8). The contact force computation is defined as:

$$f_c(\gamma_x) = \frac{F_{max}}{2}\left(1 + \tanh\left(6\frac{\gamma_x - \gamma_0}{w}\right)\right)\mathbf{n} \tag{2.91}$$

and represented in Figure 2.7. γ_x is the distance from the plane, γ_0 the offset

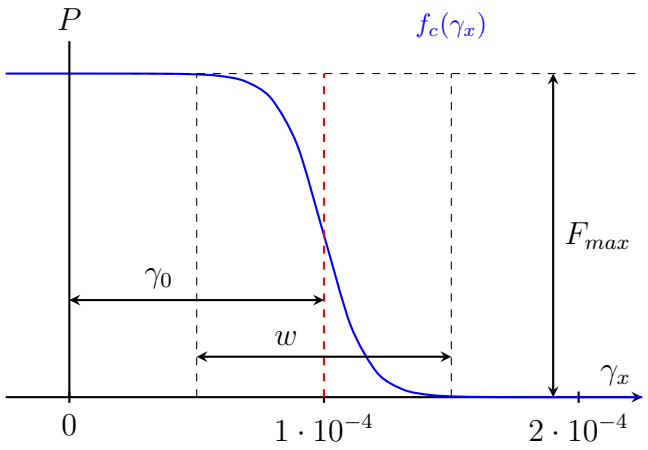

Figure 2.7: Contact force as a function of the distance from the symmetry plane.

from the wall where to activate contact, $\mathbf{n}$ is the contact plane outward normal, $F_{max} = 200$ Pa the maximal contact surfacic force, w the activation width of the contact force. Even if the contact force is chosen to be as smooth as possible to avoid discontinuities, w needs to remain small so as not to overestimate the contact force and F_{max} needs to be large enough to force the structure to deform. If it is too small the structure will penetrate too much without deforming and the amount of energy restituted will be too high as it will be shown in Section 2.5.2. To meet all these agreements, the timestep has to be adapted to ensure stability of the computation. In other words, the timestep has to be small enough to ensure the increase of contact force is handled correctly by the solver. This leads to the following condition on the timestep:

$$\Delta t = \min\left(\alpha_c \Delta_{\text{pair}} \frac{\|\langle \gamma_x, \mathbf{n}\rangle\|}{\|\langle \dot{\mathbf{u}}_x, \mathbf{n}\rangle\|}, \Delta t_{max}\right) \tag{2.92}$$

where α_c is a user-defined parameter, Δ_{pair} the length of the pair connected to the node, $\langle \gamma_x, \mathbf{n}\rangle$ the distance from the symmetry plane and $\langle \dot{\mathbf{u}}_x, \mathbf{n}\rangle$ the velocity component normal to the symmetry plane. The timestep is then adapted to the smallest value between the timestep computed with the contact force and the smallest timestep form the other stability conditions Δt_{max}.

2.5.2 Validation of the contact method: 3D bouncing ball

2.5.2.1 Presentation of the case

The bounce of a ball has been studied in the literature from both the experimental and numerical point of view. Hubbard and Stronge [156] have studied the ball during contact by filming from the bottom the ball bounce on a transparent glass plate. The contact region is at first flattened and after a critical deformation, the ball surface is snapped through as illustrated in Figure 2.9. On the numerical side, some authors showed interest in the contact of a rigid ball submitted to gravity over

a wall surrounded by fluid. The choice has been made for this work to concentrate on the simplest case, considering only structural deformation and contact forces on the bounce of a hollow ball on a rigid surface. The configuration is described in Figure 2.8. The internal and external radius are $R = 0.009$ m and $R = 0.01$ m and the material density equals $\rho = 1050$ kg/m^3. The ball is deformable and modelled as neo-Hookean hyperelastic material. The Young modulus and Poisson ratio of the ball are 100 kPa and 0.4. This set of parameter is chosen as a step towards the valve FSI simulation to ensure the contact is handled properly. The ball is subjected to gravity $g = -9.81$ m/s^2 and is moving normal to the contact plane. The ball is dropped from a height $h = 0.05$ m and bounces over a rigid plane. The adaptive timestep parameters are $\alpha_c = 0.01$ and $\Delta t_{max} = 0.001$ s. Concerning the Newmark decay factor γ, the value of 0.15 has been chosen in this case.

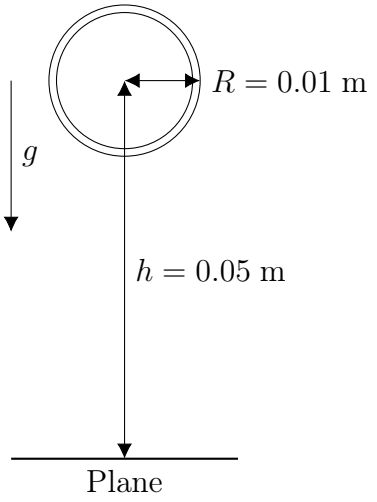

Figure 2.8: Case configuration.

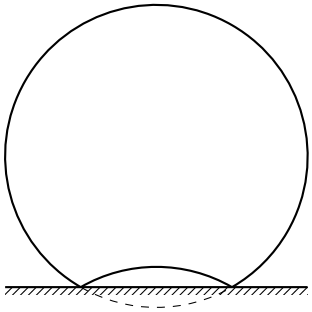

Figure 2.9: Ball snap-through on a rigid surface.

2.5.2.2 Results and discussion

The results of the bouncing ball are presented in Figure 2.11 and compared to both the results of Hubbard and Stronge [156] for the snap-through and a video of a tennis ball shown for reference. The results are in good qualitative agreement with the literature. The snap-through is well captured and the dynamics of the ball is well represented. This can be seen on Figure 2.11 on column 2 where the computed contact force is exhibited. As the ball is still not too much smashed in the wall, the contact remains moderate. After reaching the critical state of deformation, the contact region is pushed back inside the ball, corresponding on the views where the contact force acts on the ball as a ring. Next to lay out the dynamics of the ball, the vertical velocity is plotted in column 3. On the top 4 images, one can see the first phase of the bounce where the ball is compressed and the contact force increases. After reaching the peak of deformation, the ball is pushed back as on the bottom 4 images. The dynamics of the tennis ball is well represented in the video showing at

first a compression wave followed by an expansion wave which matches the dynamics found in the simulation.

The total energy of the system has been computed to ensure consistency of the method. The total energy of the system is defined as:

$$E = \int_\Omega \frac{1}{2}\rho\|\dot{\mathbf{u}}\|_2^2 \mathrm{d}\Omega + \int_\Omega W \mathrm{d}\Omega + mgz \tag{2.93}$$

where each term are respectively the kinetic energy, the strain energy and the potential energy of the ball. The total energy of the system is plotted in Figure 2.10 and shows a good conservation of the energy. The energy is not perfectly conserved during the bounce as the decay factor γ is not zero. This can be seen after each bounce where the remaining strain energy is dissipated.

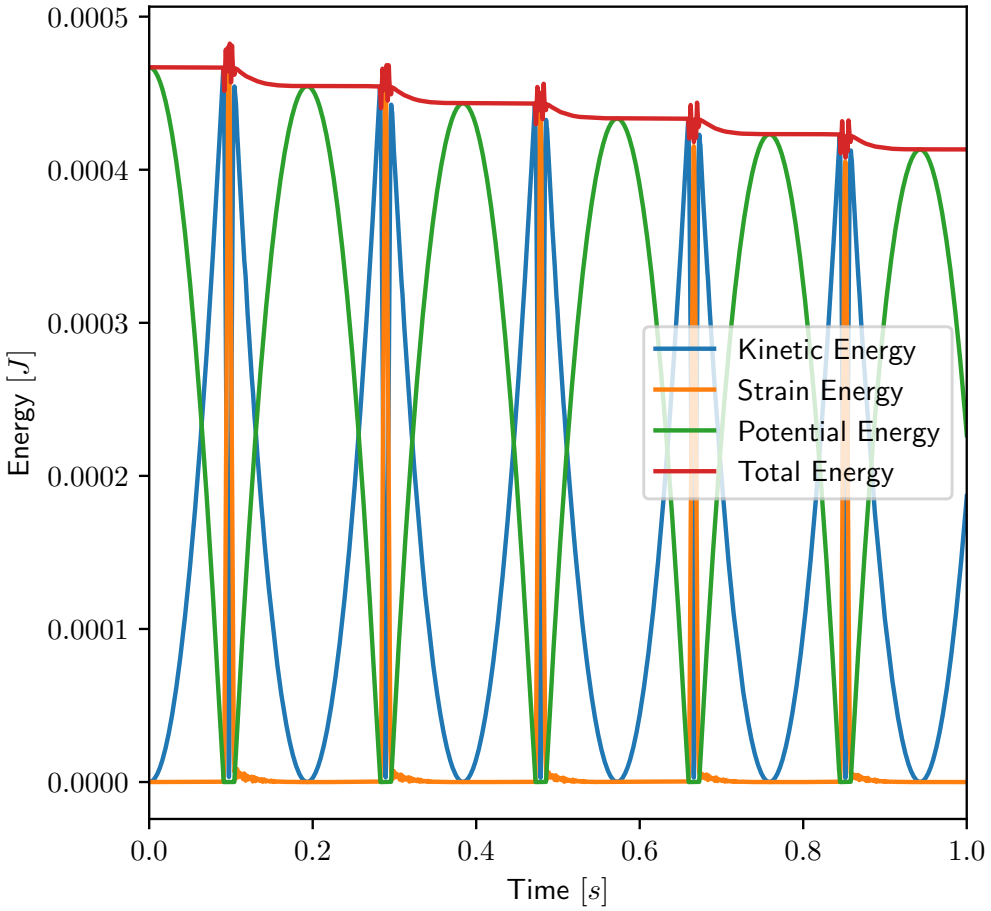

Figure 2.10: Plot of the total energy of the system with each component as a function of time.

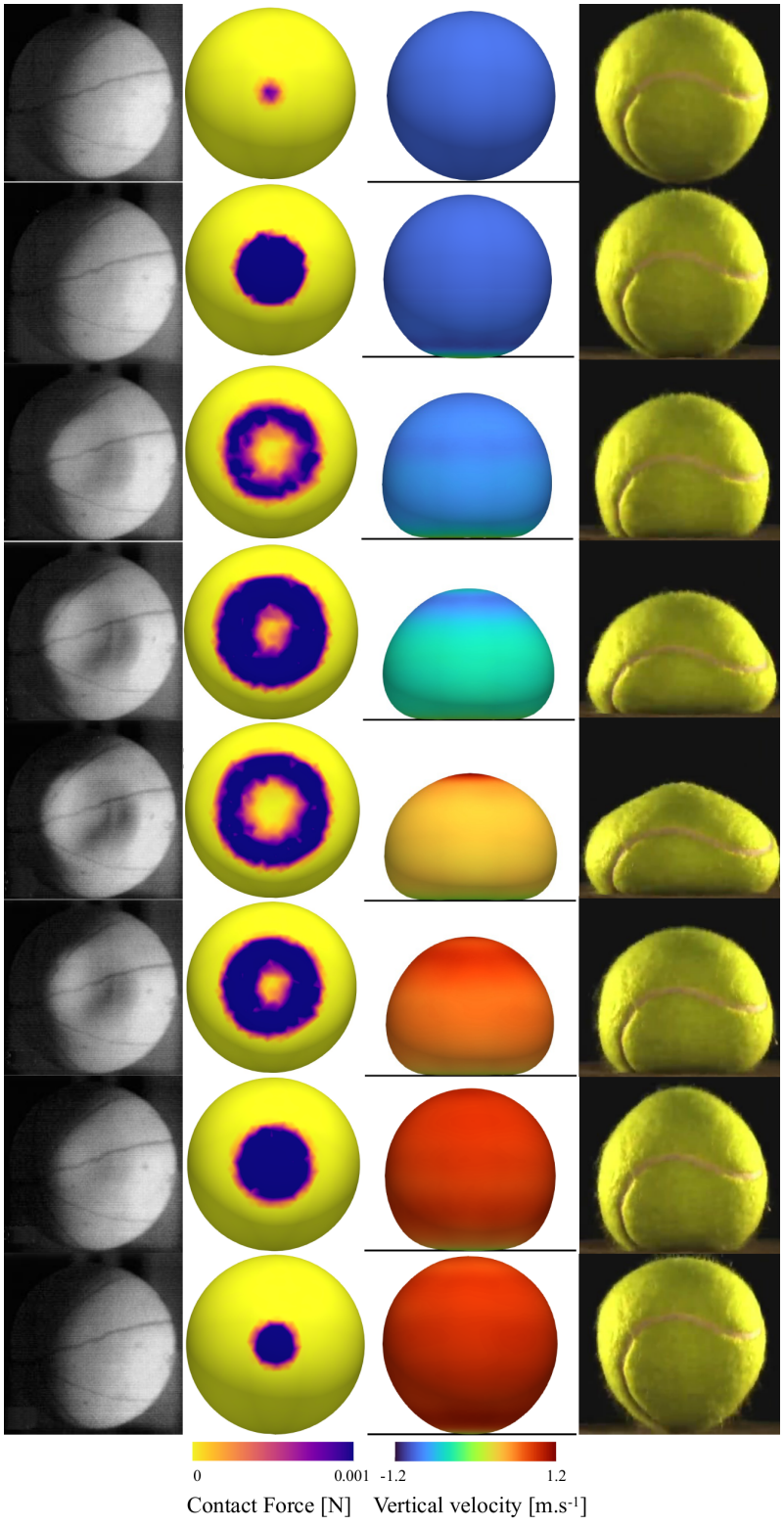

Figure 2.11: Illustration of the bouncing ball dynamics. From left to right: images from Hubbard and Stronge [156], view from the bottom of the ball showing the contact force (present simulation), view from the side of the ball showing the vertical velocity (presented simulation), images extracted from YouTube video `https://www.youtube.com/watch?v=1yT0hxplVBg`.

2.6 FSI method

The FSI method used in this work is a body-fitted partitioned semi-implicit predictor-corrector coupling scheme, developed in [120], accelerated with Aitken's method.

2.6.1 Fluid mesh movement: Pseudo-solid method

As an FSI body-fitted method is of use here, the fluid domain has to follow the leaflets' movement, and the deformation of the fluid grid has to be computed. The grid is then considered as a linear elastic material, where the displacement of the nodes inside the domain obeys the static equilibrium equation written in FEM formalism (detailed in Section 2.4.1):

$$\mathbf{K}^{ps}\mathbf{u}^{ps} = \mathbf{f}^{ps} \tag{2.94}$$

where $\mathbf{K}^{ps}$ is the stiffness matrix of the pseudo-solid grid, $\mathbf{u}^{ps}$ the displacement vector of the pseudo-solid grid and $\mathbf{f}^{ps}$ the internal forces. This method is called the pseudo-solid method (hence the superscript ps). This equation is solved using the algorithm presented in Section 2.4.2.6 with imposed displacement at the boundaries of the domain. $\mathbf{u}^{ps}$ is then used to update the grid velocity $\mathbf{w}_{n+1}$:

$$\mathbf{w}_{n+1} = \frac{\mathbf{u}^{ps}_{n+1} - \mathbf{u}^{ps}_{n}}{\Delta t} \tag{2.95}$$

where n corresponds to the temporal iteration index. The grid deformation needs to follow the displacement of the interface. Close to the interface, the grid deformation has to preserve a good quality of the mesh to capture precisely the forces of the fluid onto the structure. But far from the interface, the grid has to handle the deformation of the structure. As the grid deformation is dependent on its elements' stiffness, e.g. the Young modulus, the grid has to have different stiffness as a function of the distance from the interface. The pseudo-Young modulus of the grid is then adjusted with the following equations as a function of the distance from the interface R:

$$\begin{cases} E(R < R_{min}) = 100E_{int} \\ E(R_{min} < R < R_{max}) = E_{int} - \dfrac{(R_{min} - R_{max})(E_{int} - E_{min})}{R_{max} - R_{min}} \\ E(R > R_{max}) = E_{min} \\ E_{int} = E_{min}y_r \end{cases} \tag{2.96}$$

Where the pseudo-Young modulus ratio y_r, R_{min} and R_{max} the minimal and maximal distance from the interface, are user-defined parameters. The Young modulus of the elements close to the interface is 100 times higher than the elements in the rest of the domain. This preserves the quality of the mesh close to the interface and allows the grid to deform with the structure. The transition zone is set between R_{min} and R_{max}, this is where the elements will deform to handle the structure deformation.

At this point, the grid deformation can be computed, but the quality of some elements may be degraded. To keep the quality of the mesh as good as possible, the

pseudo-Young modulus of elements already strongly distorted has to be adjusted to strengthen them. The pseudo-Young modulus is then scaled by the distortion rate of the elements:

$$E(t_{n+1}, S(t_n)) = \frac{[E_{int} - E(t_0)][(S_k(t_n) - S_k(t_0)]}{S_{k,max} - S_k(t_0)} + E(t_0) \tag{2.97}$$

where $S_k(t_n)$ is the skewness of the elements at the current time step, $S_{k,max} = 0.91$ the maximal skewness allowed and $E(t_0)$ the pseudo-Young modulus at the beginning of the simulation. S_k is defined as:

$$S_k = \frac{V_{ref} - V_c}{V_{ref}} \tag{2.98}$$

V_c is the volume of the current element and V_{ref} the volume of the equivalent *perfect* element (the one that fits in the circumscribed sphere as the original element, see the principle in 2D in Figure 2.12a).

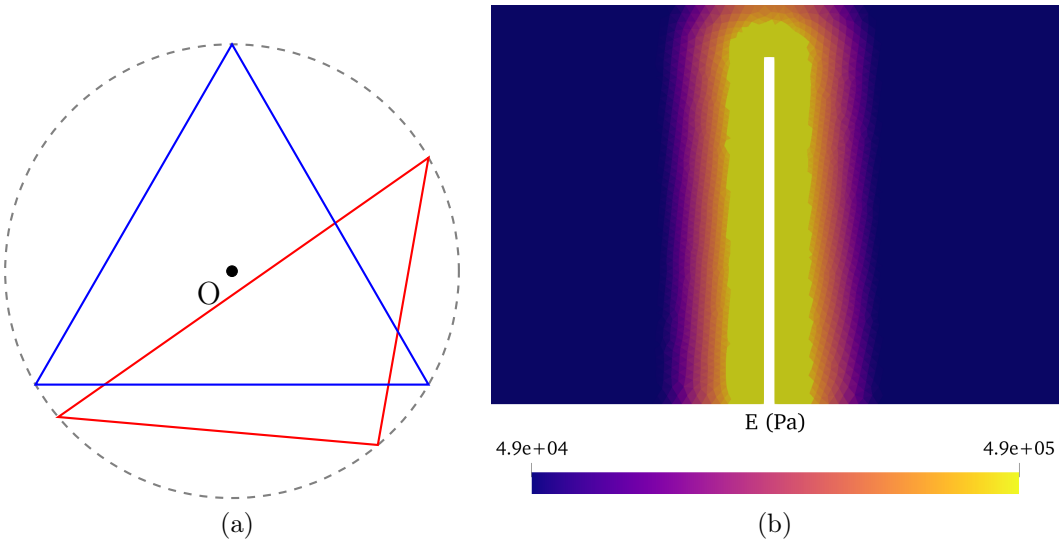

(a) (b)

Figure 2.12: (a) 2D representation of the skewness of a triangle (red) and its reference triangle (blue). (b) Pseudo-Young modulus of the validation case presented in Section 2.6.6.

2.6.2 Dynamic mesh adaptation

As described previously, in the context of biomechanical FSI simulations, mesh movement on one boundary of the domain at least is prescribed. For this purpose, the mesh movement algorithm has been presented in Section 2.6.1. However, the mesh movement algorithm may not be always able to preserve the mesh quality; in this case, a complete new mesh has to be generated i.e. with Dynamic Mesh Adaptation (DMA). Such a method has been implemented in YALES2 using MMG, the sequential anisotropic mesh adaptation library for tetrahedral (3D) and triangle

element (2D) [157, 158]. The parallel strategy proposed by Benard et al. [159] is used. The advantages of DMA have already been explored in a variety of configurations, including simulations of multiphase flows [160, 161] and moving bodies [162]. Performing mesh adaptation at every timestep would be too computationally expensive. A maximum criterion of the mesh distortion is then defined to trigger the mesh adaptation. This criterion is based on the skewness of the elements defined in Equation (2.98). At each timestep, the maximum skewness among all the elements is computed, and the mesh adaptation is triggered if the skewness of the elements is greater than a user-defined threshold. If the adaptation loop is triggered, the grid is adapted successively to reduce the skewness until the desired skewness is reached, and all data are interpolated onto the new grid. The size of the cells is preserved thanks to a metric field computed on the previous mesh.

2.6.3 Coupling equations and boundary conditions

In the following, the fluid domain is denoted Ω_f and the solid domain Ω_s. The interface between the fluid and the solid is denoted Γ_i. The fluid and mesh velocities are respectively $\mathbf{v}$ and $\mathbf{w}$, and the solid displacement $\mathbf{u}$. The force acting on the solid is $\mathbf{f}$. At the interface the following conditions hold:

$$\mathbf{v}_{n+1} = \mathbf{w}_{n+1} = \dot{\mathbf{u}}_{n+1} \tag{2.99a}$$

$$\mathbf{f}_{n+1} = \int_{\Gamma_i} \left(\mu \frac{\partial \mathbf{v}_{n+1}}{\partial \mathbf{n}} - p_{n+1}\mathbf{n} \right) d\Gamma_i \tag{2.99b}$$

where Γ_i is an element of the interface Γ_i, μ is the dynamic viscosity, p_{n+1} the pressure at the interface and $\mathbf{n}$ the normal direction to Γ_i pointing outward of the solid domain. This leads to a Dirichlet-Neumann boundary condition at the fluid-structure interface. Data transfer through the interface is done thanks to the CWIPI library [163, 164]. The density ratio $\frac{\rho_s}{\rho_f}$ in the cases considered in this works equals 1, which implies using a semi-implicit coupling scheme, presented hereafter.

2.6.4 Coupling algorithm

The coupling algorithm used in this work is a semi-implicit predictor-corrector scheme. The fluid and solid problems are solved separately with the methods presented in Section 2.3 and Section 2.4, respectively. It can be split into the following steps:

1. Iteration $n+1$ starts with Δt_f computation from the stability condition of the Runge-Kutta method used by the fluid solver. As the solid solver uses a Newmark scheme, which is unconditionally stable (see Section 2.4.4.2), Δt_f is sent to the solid solver to impose $\Delta t_s = \Delta t_f$.

2. The solid displacement $\mathbf{u}^*_{n+1}$ is estimated with a first-order extrapolation:

$$\mathbf{u}^*_{n+1} = \mathbf{u}_n + \Delta t \dot{\mathbf{u}}_n \tag{2.100}$$

3. $\mathbf{u}^*_{n+1}$ is transferred to the fluid with the CWIPI library.

4. Fluid mesh displacement is solved with the method explained in Section 2.6.1. $\mathbf{u}^*_{n+1}$ is used as a boundary condition. The fluid mesh velocity $\mathbf{w}_{n+1}$ is computed to perform the fluid velocity prediction $\mathbf{v}^*_{n+1}$ (Equation (2.15)).

5. $\mathbf{v}^*_{n+1}$ is corrected with Chorin's projection method (Equation (2.19d)). The new pressure field is computed with Equation (2.20) to correct the velocity $\mathbf{v}^k_{n+1}$ (Equation (2.21)).

6. The fluid force $\mathbf{f}^k_{n+1}$ is then transferred to the solid by the CWIPI library.

7. The displacement $\mathbf{u}^k_{n+1}$ in the solid is solved using the method detailed in Section 2.4.

8. The solid and fluid problems have been solved at least once at this point. The dynamic equilibrium of the FSI system is checked for consistency with the following:

$$\frac{||\mathbf{u}^k_{n+1} - \mathbf{u}^{k-1}_{n+1}||}{\delta_s} \leq \epsilon_s \tag{2.101a}$$

$$\frac{||\mathbf{f}^k_{n+1} - \mathbf{f}^{k-1}_{n+1}||}{||\mathbf{f}_{n+1} - \mathbf{f}_n||} \leq \epsilon_f \tag{2.101b}$$

   where ϵ_f and ϵ_s are chosen convergence tolerances for the fluid and solid problems respectively, δ_s is the solid thickness. If the convergence criterion is reached, the algorithm starts next time iteration.

9. Otherwise, the solid displacement is under-relaxed on the interface Γ_i:

$$\tilde{\mathbf{u}}^k_{n+1} = \alpha \mathbf{u}^k_{n+1} + (1-\alpha)\mathbf{u}^{k-1}_{n+1} \tag{2.102}$$

   where α is the dynamic under-relaxation factor computed with the Aitken method, further presented in Section 2.6.5.

10. $\tilde{\mathbf{u}}^k_{n+1}$ is transferred to the fluid boundary with the CWIPI library.

11. A new field of $\mathbf{w}_{n+1}$ is obtained with the pseudo-solid solver.

With the initial velocity prediction $\mathbf{v}^*_{n+1}$ and the updated $\mathbf{w}_{n+1}$, a new pressure field can be computed, and the algorithm goes back to step 5. Step 5 to 11 are repeated until the convergence is reached. Then the algorithm is then ready for the next time iteration. The whole procedure is detailed in Figure 2.13.

2.6.5 Acceleration with Aitken's method

Aitken developed his delta-squared method in 1937 to accelerate the rate convergence of a series [102]. His method was extended to the vector case by Irons and Tuck [103]. It has been proven very efficient in the acceleration of the convergence

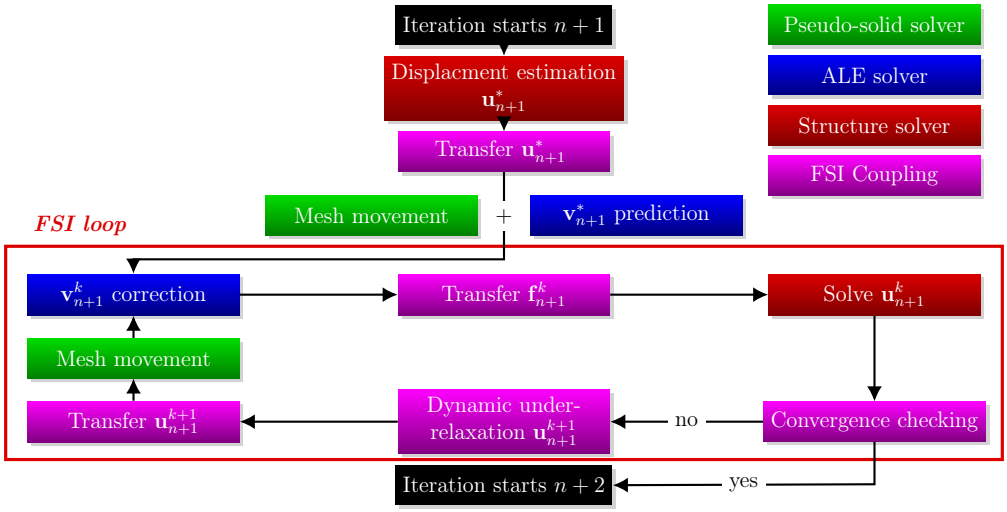

Figure 2.13: FSI coupling algorithm.

of strong coupling FSI algorithms by Mok [109] and is now commonly used in the field [90, 104, 106–108]. In this work we retain the formulation of the method as presented in [109]. It consists in evaluating the Aitken's acceleration factor γ_{k+1} at each FSI subiteration as:

$$\gamma_{k+1} = \gamma_k + (\gamma_k - 1)\frac{\int_{\Gamma_i}\langle \Delta\mathbf{u}_{k+1} - \Delta\mathbf{u}_k, \Delta\mathbf{u}_k\rangle \mathrm{d}S}{\int_{\Gamma_i} ||\Delta\mathbf{u}_{k+1} - \Delta\mathbf{u}_k||^2 \mathrm{d}S} \tag{2.103}$$

where $\Delta\mathbf{u}_{k+1} = \mathbf{u}^{k+1}_{n+1} - \mathbf{u}^k_{n+1}$. The convergence under-relaxation equals then $\alpha_{k+1} = 1 - \gamma_{k+1}$. The solid displacement is then corrected with the Aitken's acceleration factor:

$$\mathbf{u}_{n+1} = \mathbf{u}^{k+1}_{n+1} + \gamma_{k+1}(\mathbf{u}^{k+1}_{n+1} - \mathbf{u}^k_{n+1}) \tag{2.104}$$

2.6.6 Validation of the FSI method

The benchmark used to validate the method is extracted from Boilevin-Kayl, Fernández, and Gerbeau [125] a slightly modified version of the benchmark proposed in [40, 126, 127] which originated from [123]. This case is of primary interest in the context of valve simulations as the main directions of the solid and the fluid flow are orthogonal, as in biological valves. It consists of a straight beam inside a channel, analogous to a blood vessel, a flow parallel to the channel (and orthogonal to the beam). A sketch of the case is depicted in Figure 2.14. The dimension of the channel and beam are $(l \times h) = (0.08\ m \times 0.00805\ m)$ and $(e \times h_1) = (0.000212\ m \times 0.007\ m)$, respectively. The beam base is located at $l_1 = 0.019788\ m$ from the inlet.
x is the axial coordinate. The fluid density is $100,000\ \mathrm{kg \cdot m^{-3}}$ as well as the solid density. The kinematic viscosity equals $1 \times 10^{-5}\ \mathrm{m^2 \cdot s^{-1}}$. A no-slip boundary condition is imposed at the bottom wall and a symmetry condition at the top boundary. The velocity at the inlet is imposed as a Dirichlet condition, with the following profile:

$$\mathbf{v}_y(t) = 500(1.1 + \sin 2\pi t)y(h - y) \tag{2.105}$$

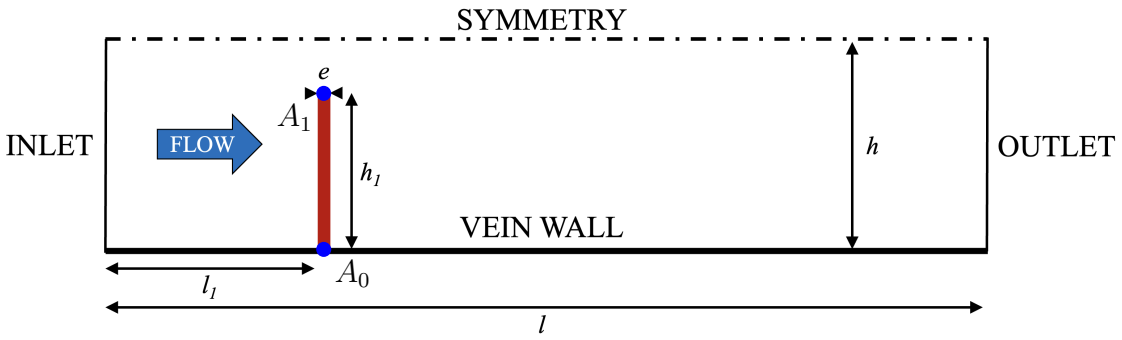

Figure 2.14: Benchmark schematic illustration

The solid is modeled as a neo-Hookean material with Young modulus $E = 5.7$ MPa and Poisson ratio $\nu = 0.4$. It is embedded at point A_0. Point A_1 marks the beam tip. At the initial time, the fluid is at rest and the solid is in its reference, stress-free, position. In this configuration, the channel height is $2h = 1.61$ cm and the bulk velocity is $6.8\ \text{cm} \cdot \text{s}^{-1}$, leading to a Reynolds number of 110.

We compare the result obtained with the present body-fitted method to the results of Boilevin-Kayl, Fernández, and Gerbeau [125]. The axial and radial displacement of point A_1 are drawn in Figure 2.15, showing a good agreement with the results from Boilevin-Kayl, Fernández, and Gerbeau [125]. The dynamics of the beam is reproduced accurately. To illustrate the dynamics of the system, snapshots of the fluid velocity magnitude around the beam and the fluid traction at the interface can be found in Figure 2.16.

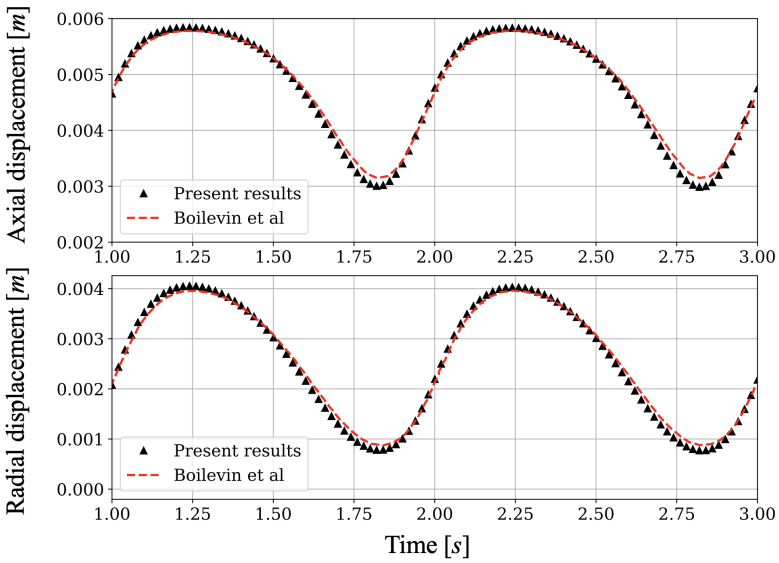

Figure 2.15: Displacement of point A_1 against time

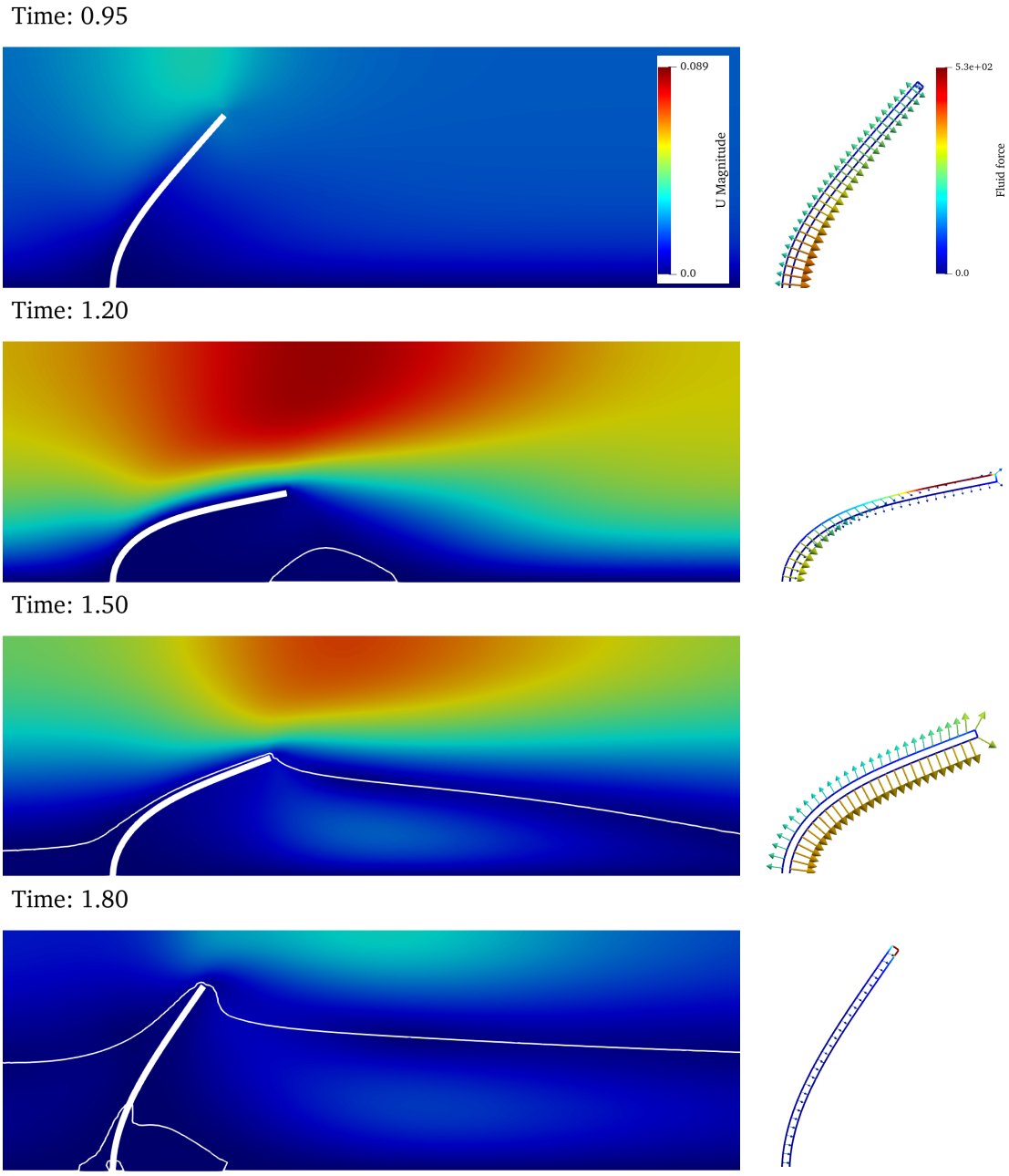

Figure 2.16: On the left: snapshots of the fluid velocity magnitude at different times, the white line shows the isocontour of $u_{axial} = 0$. On the right: fluid traction at the interface

Chapter3

Analysis of Vein Valve Dynamics and Associated Hemodynamics

Chapter overview: *This chapter introduces the anatomy and physiology of venous valves, offering an overview of their geometry, composition, and blood flow dynamics within the deep venous system. We provide a review of recent numerical studies on venous valves. The geometric model of the femoral venous valve developed in this work, based on the surface reserve hypothesis, is described in detail. This is followed by a comprehensive structural analysis and a fluid-structure interaction (FSI) simulation of the valve under respiratory pump conditions.*

Contents

3.1 Vein valves in the lower limbs

3.1.1 General anatomy

The venous system is divided into two main components: the superficial and deep veins. The superficial veins are located within the subcutaneous tissues and comprise the great and small saphenous veins (GSV and SSV), along with their tributaries, which extend from the foot to the mid-thigh. These veins collect deoxygenated blood from the muscles, which is then transferred to the deep veins, located between the muscles and bones, either via perforating veins or the sapheno-femoral junction.

The deep venous system in the legs is composed of four groups, extending from the pelvis to the foot: the iliac, femoral, popliteal, and tibial veins. Valves are found in all of these systems except the iliac [27]. As hospital-acquired deep vein thrombosis (DVT) primarily occurs in the popliteal and femoral systems, or near the sapheno-femoral junction, this study focuses on these specific regions.

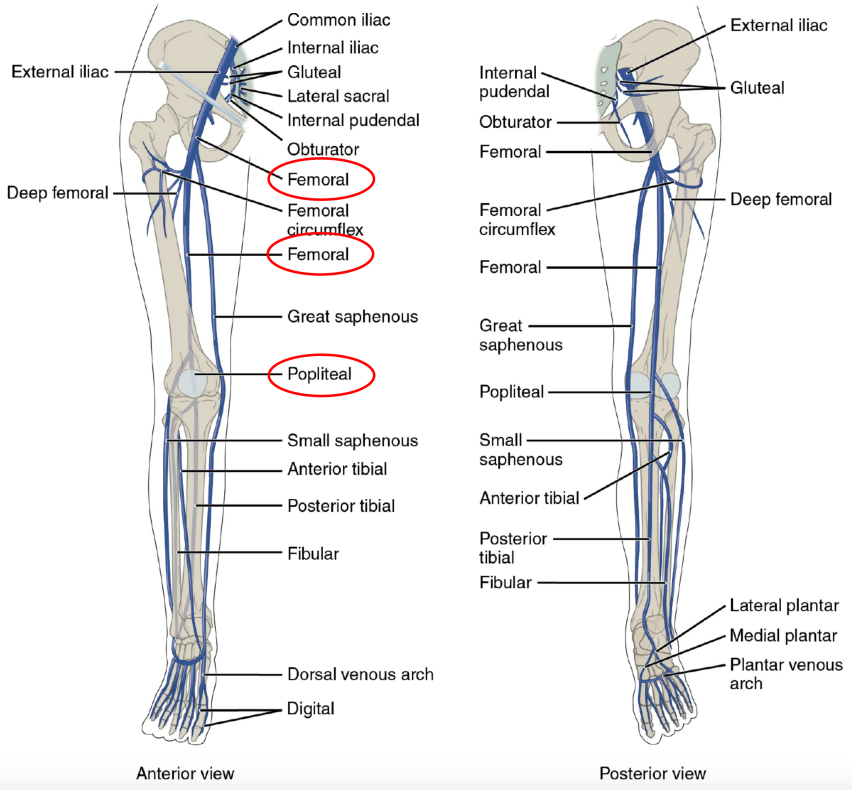

Figure 3.1: Main veins serving the lower limbs. The veins circled in red will are the one of interest in this work. Extracted from [25].

In the context of the DYV-MTEV project, the CHU of Nîmes provided an ex vivo sample of a great saphenous vein to the CBS team for analysis. The vein valve was obtained from a patient who had undergone surgical artery bypass with autologous vein graft and was subsequently imaged using magnetic resonance imaging (MRI)

and micro-computed tomography (Micro-CT) techniques in collaboration with the BioNanoImaging Foundry in Montpellier. The imaging techniques employed permitted the generation of a three-dimensional reconstruction of the vein valve with high resolution (50 μm/px for the MRI and 20 μm/px for the Micro-CT scan). The anatomy of great saphenous vein valves is analogous to that of deep veins, rendering them a suitable model for studying deep vein valves, which are only accessible through extensive surgeries like amputations.

The MRI data and key measurements are displayed in Figures 3.2 and 3.3, respectively. The average diameter of the vein is approximately 6 mm, calculated from the average vein perimeter (Figure 3.3.A, 20 mm), with an increase at the valve location. A comparison of the eighth and ninth MRI slices in Figure 3.2.A of Giannetti [45] reveals that the leaflet is not visible at the midpoint of the tip in the ninth slice. This indicates that the midpoint of the leaflet lies between 3.5 mm and 4 mm from the bottom of the valve.

The sinus length increases asymptotically towards the half perimeter of the vein, approximately 10 mm (Figure 3.3.B), with a similar trend observed for the leaflet (towards the vein diameter, 6 mm). The thickness of the leaflet decreases from 300 µm at the base to 200 µm at the tip, exhibiting a 50% increase in thickness at the base (Figure 3.3.C).

The final measurement to be considered is that of the valve leaflet length in comparison to its theoretical length. If we assume that the perimeter of the vein is a circle and that the sinus length is the corresponding arc on this circle, then the theoretical leaflet length is the straight line connecting the endpoints of the arc. A visual representation of the "ideal" valve configuration is provided in Figure 3.2.D. This measurement serves as a useful indicator of leaflet surface reserve. Two distinct regimes were identified: the measured leaflet length was observed to be shorter than the theoretical length in the region of the sinus base, and longer in the region of the leaflet tip. The maximum surface reserve is observed at the tip, where the measured length exceeds the theoretical length by approximately 10%. At a critical height of approximately 1.5 mm, the measured length exceeds the theoretical length, indicating the presence of additional extension or surplus length in this section. Figure 3.3.D (left) depicts the ratio between the theoretical and measured length for each z-cut derived from the MRI scan. It should be noted that in the region closer to the leaflet tip, the sinus and leaflet exhibit a greater degree of folding, which may increase the likelihood of measurement error. However, this potential source of error was not quantified in the study by Giannetti [45]. Additionally, the thickening of the leaflet near its insertion was also observed by [165] and referenced therein.

In a recent publication, [28] reported a mean vein diameter of 8 mm for four valves. Other studies have yielded higher mean values for the common femoral vein, with measurements ranging from 11.8 mm [166] to 14.3 mm during the Valsalva maneuver, and up to 16.4 mm in an upright position [167]. The Valsalva maneuver involves forced expiration against a closed glottis, which increases both intra-thoracic and venous pressure.

With regard to the GSV diameter in women, the mean was found to be 6.5 mm

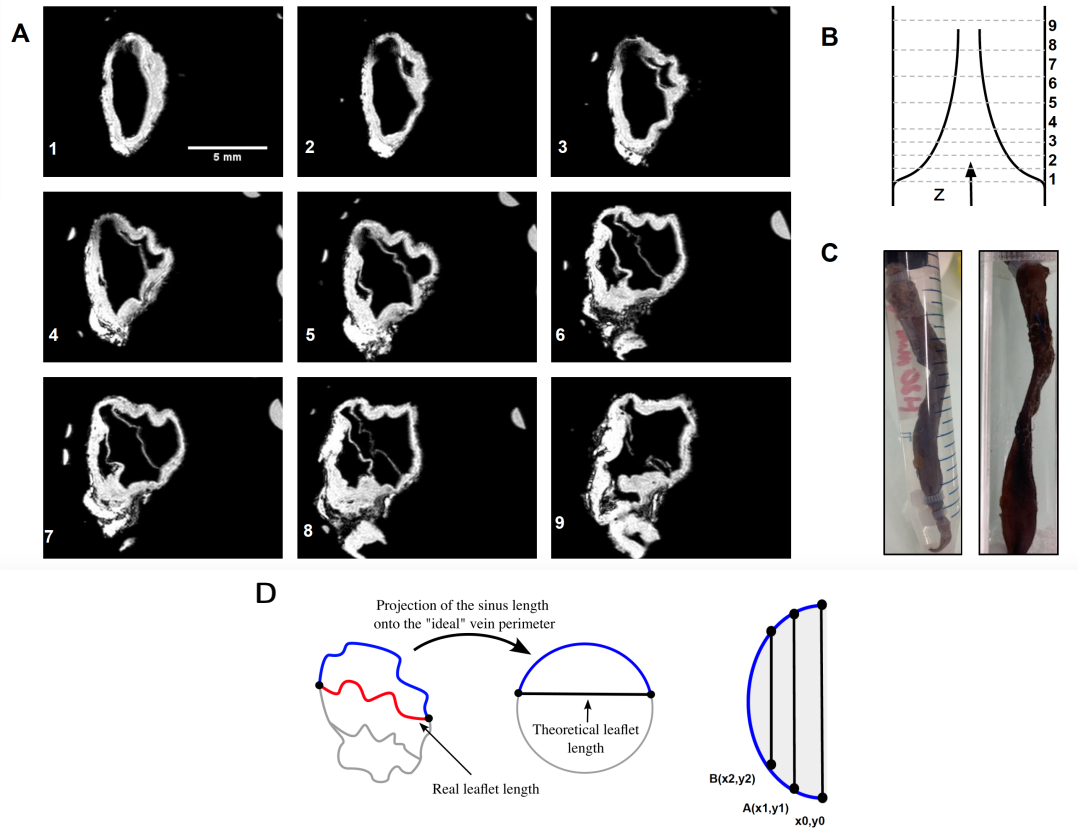

Figure 3.2: (A) Z-normal slices from the MRI acquisition of the valve region, and (B) schematic representation of the cut positions along the z-axis from the bottom of the sacs (1) to the leaflet tips (9). (C) Photograph of the preserved GSV valve used in the study. (D) Schematic representation of the post-processed MRI measurements. The sinus is indicated in blue, the projected leaflet in the Z-plane in red, and the theoretical leaflet projection in the Z-plane in black (the straight line between the insertion points). Courtesy of Giannetti [45].

by [168], while [169] reported diameters between 5 and 6 mm. Accordingly, for the veins studied throughout this work, the diameter ranges from 5 to 14 mm. According to [170], the mean diameter of the popliteal vein is 6.08 mm. The thickness of vein walls varies from 300 to 1000 μm, as reported in [171–173]. Leaflet thickness also varies significantly, with 100 μm commonly used in bioprosthetic valves [28, 174]. In a study of the popliteal vein, [175] found leaflet thicknesses of 350 μm in young adults and 590 μm in elderly subjects. It should be noted that there was an increased standard deviation with age. In their study of a bioprosthetic femoral vein valve, Pavcnik et al. [176] reported a leaflet thickness of 30 μm.

A key question is to determine the shape of the leaflet insertion on the sinus. Caggiati [165] described the insertion as "*shaped like a double horseshoe with the convex sides arranged distally*". However, no physiological representation of the insertion was provided until the work by Hofferberth et al. [28], who designed a

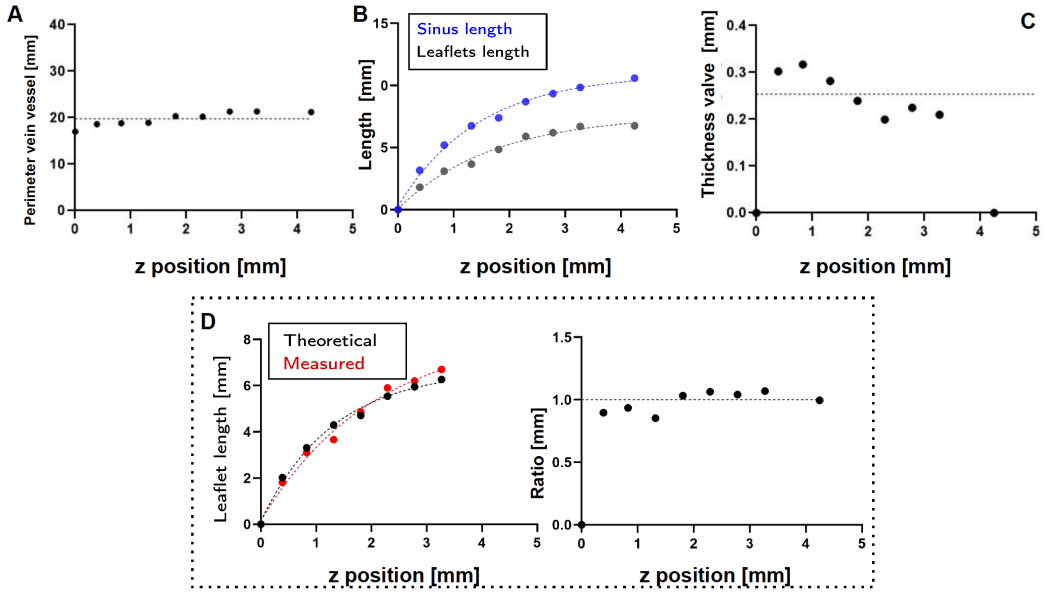

Figure 3.3: Key measurements for each z-cut from the MRI acquisition of the preserved saphenous vein valve. (A) Vein perimeter, with the average indicated by the dashed line. (B) Measurements for the sinus and leaflet lengths. (C) Leaflet thickness, with the average (dashed line). (D) Leaflet length and theoretical length, with their ratio plotted on the right. The blue, red, and black lines represent the sinus, leaflet, and theoretical lengths, respectively. Courtesy of Giannetti [45].

novel bioprosthetic replacement cardiac valve inspired by venous valves. Due to their high compliance, vein valves are excellent candidate of study for bioprosthetic valve design. Such valves can be implanted in pediatric patients without the need for future surgeries [18, 28]. Hofferberth et al. [28] studied four cryopreserved femoral veins were analyzed, and two key parameters were retained to characterize venous valve dimensions (see Figure 3.4):

$$\Phi_v = \frac{h}{d} \tag{3.1}$$

$$\Phi_l = \frac{h}{h_{1/2}} \tag{3.2}$$

where Φ_v and Φ_l are the valve and leaflet ratios, respectively. Φ_v was found to be 2, while Φ_l was 0.5. The variable h represents the valve height, d the vein diameter, and $h_{1/2}$ the leaflet mid-height. The blue line in Figure 3.4 represents the leaflet insertion, projected onto the vein wall as a quarter ellipse with major axis $4R$ and minor axis R, where R is the vein radius. The red line illustrates the position of the leaflet tip. It is worth noting that the leaflets fully contact the vein wall once the valve is cut open and unrolled, as observed by Hofferberth et al. [28].

The mechanical properties of vein valves were first studied in the 1980s by Ackroyd, Pattison, and Browse [177], who conducted an analysis of the ultimate tensile strength and strain of preserved human superficial femoral vein valves at different

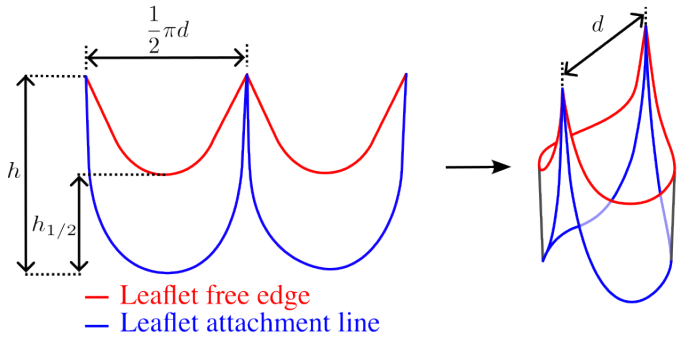

Figure 3.4: Key dimensions and geometrical description of a vein valve and its leaflets. The blue line represents the leaflet insertion (horseshoe shape), and the red line represents the leaflet's free edge. Extracted from [28].

locations. The ultimate tensile strength of the valve leaflets was found between 8 and 10 MPa, significantly higher than that of the vein wall (4.5 to 5.5 MPa in the circumferential direction and 3 MPa in the axial direction [177]), with an associated strain of 35%. There has been a recent increase in interest in vein valve mechanics. In recent studies such as Huang and Lu [178], Lu and Huang [179], and Benson and Huang [180] bovine jugular vein valves were characterized. As demonstrated in [178, 179], these valves exhibit pronounced mechanical anisotropy and non-linear behavior, with a 3:1 stiffness ratio between the circumferential and radial directions. This finding was later confirmed by Benson and Huang [180]. In a notable contribution to the field, Holzapfel [181] developed a non-linear material model for aortic valve leaflets. This model splits the energy strain density function into isotropic and orthothropic contributions, following neo-Hookean and Fung-type models, respectively. Subsequently, the methodology was later adapted by Herrera, Fortuny, and Marimón [182] for application to femoral vein walls.

3.1.2 Blood flow in the deep venous system

In the supine position, the venous waveform is primarily controlled by the respiratory pump [183]. During inspiration, the decrease in thoracic cavity pressure activates venous return from the lower limbs. The opposite phenomenon arises during exhalation. The pressure at the ankle in the supine position is 20 mmHg, which is sufficient to ensure optimal blood return. The pressure gradient is oriented toward the foot, with blood flowing in the opposite direction of the pressure gradient.

In contrast, while standing, the pressure ranges from 90 to 120 mmHg [184] because of gravity. Giving that the average distance between valves in deep veins is approximately 4 cm [42] and the average leg length for men is 81 cm [185], approximately 20 valves must be traversed by the blood. To ensure efficient venous return, the pressure drop across each valve must be less than 1 mmHg. It is therefore essential that the design, positioning and associated blood flow of the valves are carefully considered.

The calf muscle pump mechanism plays a crucial role in facilitating blood circu-

lation in the leg venous system, as evidenced by studies such as those conducted by Lurie [186] and Tauraginskii et al. [187]. The gastrocnemius muscle (GCM), which is responsible for foot extension, and the anterior tibial muscle (ATM), which is responsible for foot flexion, are the primary muscles involved. This mechanism is primarily engaged during walking and comprises two phases: stance and swing. This is illustrated in Figure 3.5. During the stance phase, the foot makes contact with the ground, beginning with heel strike, when the GCM is relaxed. As the center of mass shifts forward, the GCM contracts, resulting in a pressure peak ranging from 128 to 148 mmHg, depending on the walking pace [187]. The GCM contraction continues until the foot lifts off the ground. During the swing phase, the GCM relaxes while the ATM contracts to flex the ankle. The minimum venous pressure, corresponding to the GCM relaxation, varies from 17 mmHg at a quicker pace to 29 mmHg at a slower pace, indicating more frequent GCM relaxation and contraction during faster walking.

The physiological mechanisms that regulate venous blood flow in the legs have been delineated, including the associated pressure values and waveforms. The subsequent inquiry pertains to the typical velocities and flow rates in the perivalvular area, which have been the subject of extensive investigation. This topic has been explored in several studies [42, 166, 170, 186, 188–192]. In [188], the objective was to identify potential indicators of iliac vein obstruction or deep vein thrombosis (DVT) in the thigh, utilizing the waveform as a diagnostic tool in the common femoral vein

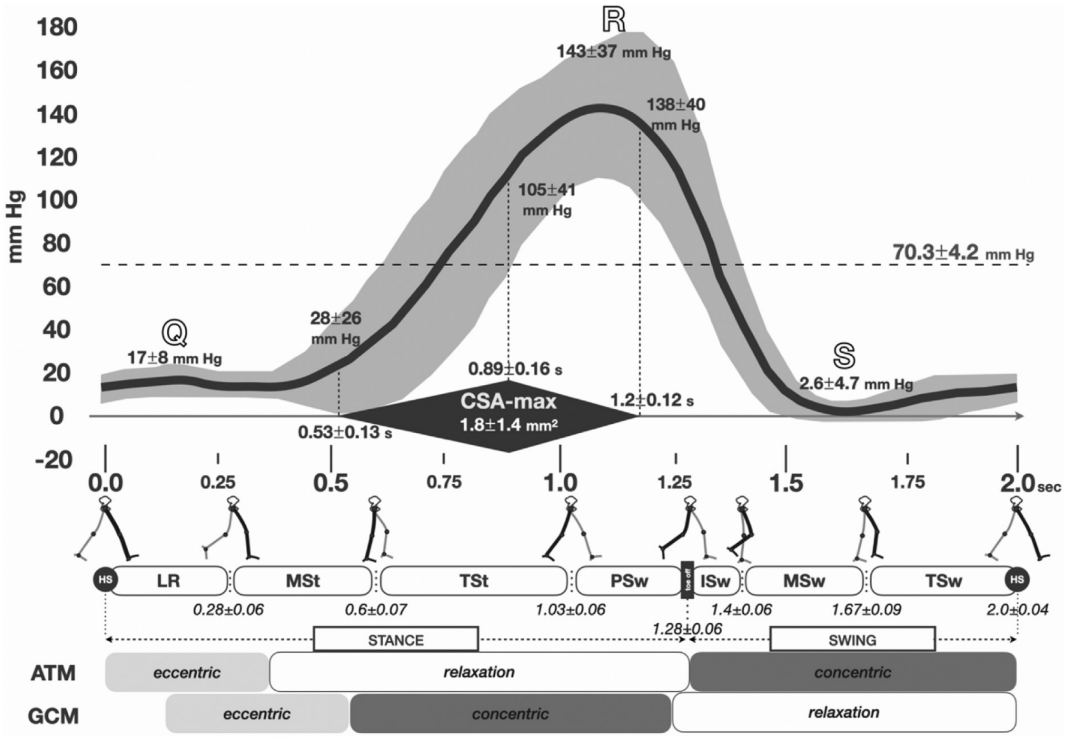

Figure 3.5: Schematic representation of the calf muscle pump and associated pressure waveform. Extracted from [187].

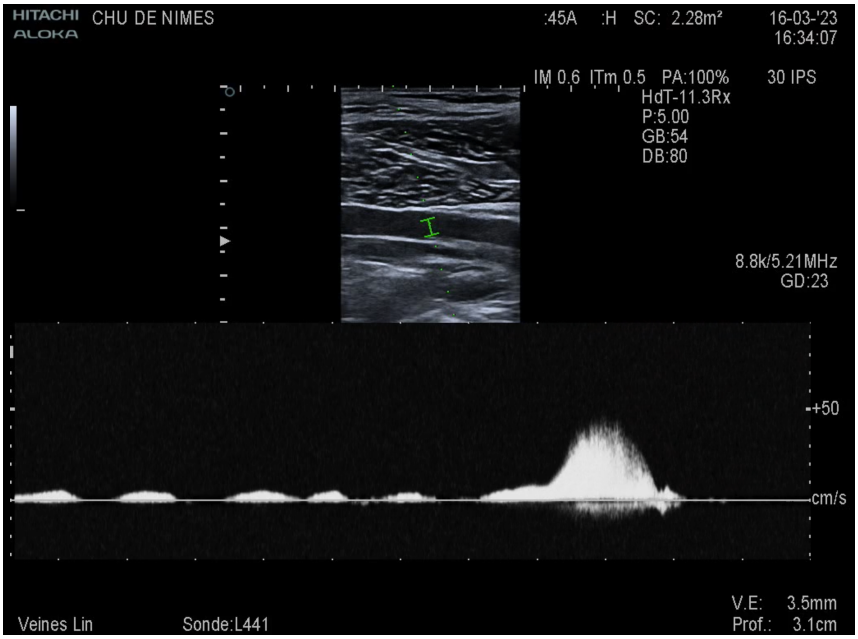

Figure 3.6: Doppler ultrasound of the femoral vein valve highlighting respiratory pump and flush velocity waveforms. Courtesy of A. Perez-Martin from the CHU of Nîmes.

(CFV). A monophasic waveform is characteristic of normal blood flow in the CFV, whereas continuous flow is observed in veins with proximal obstruction.

Furthermore, as indicated in Section 1.4.1, medical imaging of venous valves has been provided by the CHU of Nîmes, as illustrated in Figure 3.6. The Doppler ultrasound images of a femoral vein valve reveal two distinct phases. The initial phase aligns with respiratory pump cycles, while the subsequent phase is attributable to the voluntary contraction of the GCM to induce a flush. The average velocity during the respiratory pump cycle in the femoral vein ranges from 6 to 14 cm/s at rest, 23 cm/s during the Valsalva maneuver [166] and 40 cm/s with a GCM contraction (see Figure 3.6). In the case of the popliteal vein, Kalayci et al. [170] reported an average velocity of 16 cm/s for a 6 mm diameter vein, with an associated flow rate of 100 mL/min.

With regard to flow structures in the vicinity of the valves, the only assessment of hemodynamics in the great saphenous vein (GSV) at the ankle has been conducted by [192], as presented in Figure 3.7 which illustrates ultrasound images of the perivalvular region. The time-varying hemodynamics in the vicinity of the valve suggests the formation of a vortex at the leaflet tips, which contrasts with the findings of [190], who reported the presence of a vortex inside the sinus.

Another crucial parameter for assessing the performance of bioprosthetic valves in comparison to natural valves is the effective orifice area (EOA). The EOA is defined as the ratio of the cross-sectional area of the distal vein to the cross-sectional area of the valve [19, 193, 194]. However, direct measurement of this ratio is challenging. To address this issue, [19] approximated the EOA as the ratio of distal

velocity to velocity between the leaflets:

$$\text{EOA} = \frac{v_{distal}}{v_{valve}} \tag{3.3}$$

The locations of v_{distal} and v_{valve} are indicated in Figure 3.7a.c. This approximation is valid if the flow profile at the valve location is parabolic. Nevertheless, as will be discussed in the following section, the flow profile in the vicinity of the valve is markedly non-parabolic, making this formulation questionable.

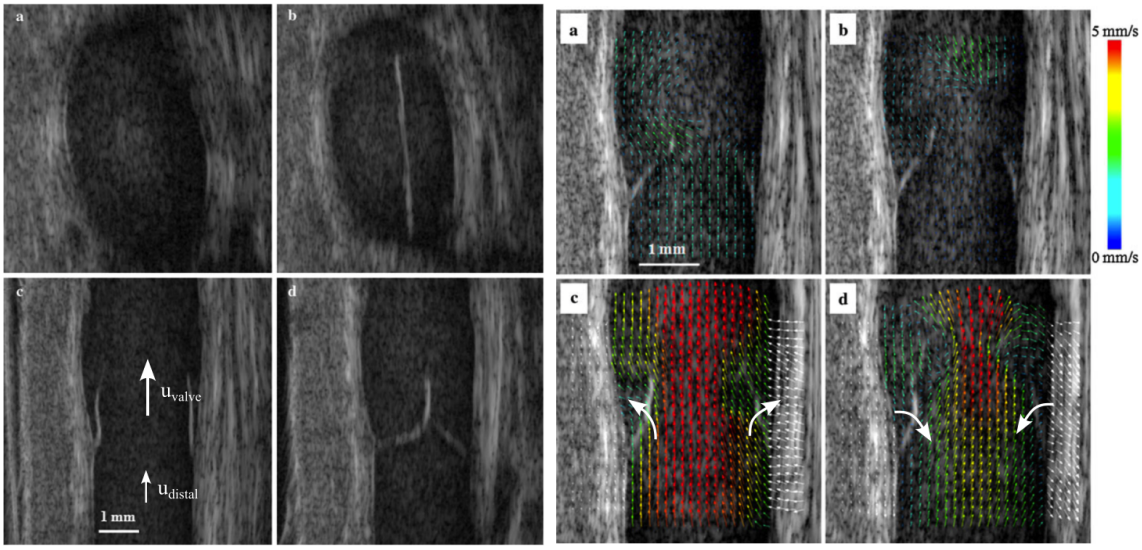

(a) (b)

Figure 3.7: (a) Ultrasound images of a valve in the GSV at the ankle, in cross-sectional and sagittal views for fully open (a, c) and fully closed configurations (b, d). The contact plane between the leaflets in the closed position is visible in (b). (b) The velocity field in the perivalvular area at different times shows the formation of a vortex at the leaflet tips. Extracted from [192].

The following section presents an overview of the numerical studies conducted on venous valves in recent years.

3.1.3 In silico simulations of vein valves

In recent decades, there has been a growing interest in numerical studies on vein valves. Computational fluid dynamics (CFD) simulations have been used to evaluate the hemodynamics of paired valve systems [195] and 2D replicas of microchip valves [196]. In [197], a system of two ball valves was employed to emulate a vein valve, with the latter being simulated through a body-fitted fluid-structure interaction (FSI) method. However, the rigidity of the valves in [195, 196] precluded the possibility of examining variable flow conditions. Moreover, the pressure dynamics and hemodynamics of a ball valve are not representative of the physiological valve

geometry. A characterization and comparison of bi-, tri-, and quad-cuspid valves was conducted in [15]. However, this study focused solely on the structural deformation of the leaflets and did not provide information on the associated hemodynamics.

In order to model the physical processes involved in valve dynamics more accurately, FSI methods have increasingly been used to simulate the behavior of vein valves. A variety of hypotheses have been proposed regarding the structural components of the system. Some studies have focused exclusively on leaflet deformation [36, 37, 75, 198–203]. Some studies incorporate both leaflet and vein wall deformations [73, 74, 76, 204–215].

A number of studies have employed two-dimensional models with either rigid walls [75, 198–201] or deformable walls [73, 212–215]. These studies were conducted to examine the effects of vessel geometry, leaflet geometry, or elasticity on hemostasis within the sinus. While two-dimensional approaches offer valuable insights into the simulation of vein valves, it is essential to recognize that real venous valves are three-dimensional and exhibit complex flow patterns. This necessitates the use of three-dimensional modeling to accurately represent the intricate dynamics of these structures.

To address these limitations, 3D vein valve models have been developed with various leaflet and sinus geometries. Some studies have elected to exclude the sinus from their models [36, 37, 50, 74, 202, 203, 205, 207]. Nevertheless, a common assumption across these studies is that the leaflets exhibit curvature in a single direction. Consequently, the leaflets deform through stretching, necessitating either a considerable force to open or highly extensible leaflets. In both instances, the requisite strain to attain the optimal effective orifice area (EOA) is approximately 25%, which is close to the ultimate strain capacity of leaflet tissues, as evidenced by Ackroyd, Pattison, and Browse [177]. The pressure necessary to induce such deformation, assuming an ultimate tensile strength of 8 MPa (Section 3.1.1) and based on Hooke's law, would be approximately 2300 mmHg—approximately 20 times the systolic pressure in the aorta. This observation is incompatible with the hypothesis that valve opening is primarily driven by tissue stretching. This is the reason why an alternative scenario is considered in this thesis: that the valve opens thanks to surface reserve rather than tissue stretching, with the leaflets exhibiting a 3D curvature. The following section presents the geometric model derived from the literature review, followed by a structural simulation study.

3.1.4 Presentation of the leaflet model

It is important to note that there is currently no consensus regarding the shape, dimensions, stress-free shape, or mechanical properties of vein valves. In a recent study by Hofferberth et al. [28], a geometrical characterization of venous bi-leaflet valves was provided. These features have been used to construct the model depicted in Figure 3.8. The valve model was developed using FreeCAD computer-aided design software, with the vein diameter set to 14 mm. The valve was positioned in a closed state, which represents its stress-free configuration. The ratios Φ_v and Φ_l were set to 1 and 0.5, respectively (see Equation (3.1)).

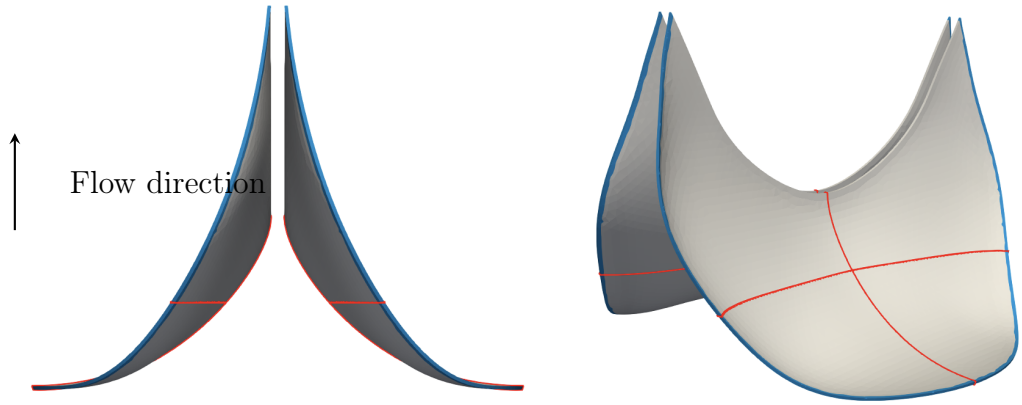

Figure 3.8: Description of the geometry of the leaflets used throughout this work. The blue lines represent leaflet insertion points, while the red lines illustrate the curvature of the leaflets.

With regard to the ratio of vein diameter to vein length, it was assumed that veins are dilated in vivo due to the presence of blood. The 2:1 ratio was determined by measuring the valve in a flat, unrolled configuration, which differs significantly from its in situ configuration. Accordingly, a lower value for Φ_v was selected to account for the dilation. The leaflet thickness was maintained at a constant value of 100 μm. The blue line in Figure 3.8 represents the insertion points of the leaflets on the vein wall. This line was constructed in accordance with the methodology outlined in Section 3.1.1, representing the projection of a quarter ellipse (with a minor radius of 7 mm and a major radius of 14 mm) onto the vein wall.

The red lines in Figure 3.8 illustrate the leaflet curvature in three dimensions, which contributes to the surface reserve. To quantify this curvature, the ratio of valve leaflet length to the theoretical length was employed (see Section 3.1.1). The surface reserve ratio was approximately 10% along the y-axis, which is consistent with the findings of Giannetti [45].

3.2 Structural analysis of the vein valve

3.2.1 Numerical set-up

The deformation of the leaflets was addressed through the application of the finite element method (FEM) structural solver within YALES2 (see Section 2.4). The computational mesh was generated using GMSH meshing software and consists of isotropic first-order tetrahedral elements with four nodes. Two mesh sizes, 200 and 300 micrometers, were employed to assess spatial convergence. A neo-Hookean material model with parameters $E = 0.1$ MPa and $\nu = 0.4$ was employed. The leaflets were subjected to a pressure load on their luminal side, which simulates the fluid load that would be experienced in fluid-structure interaction (FSI) simulations.

The leaflets were fully clamped at their insertion points along the vein wall. The total pressure load applied was 5 Pa, which corresponds to a velocity of 10 cm.s^{-1}, with a loading time of 5 s. The simulations were conducted in a time-resolved manner using the Newmark method, with damping parameters set to $\alpha_m = 1 \times 10^{-6}$ and $\alpha_k = 1 \times 10^{-3}$. The time step for the simulations was set to 1×10^{-4} s.

3.2.2 Leaflets undergoing a pressure load

The results are presented in Figure 3.9, where the energy stored by the leaflets is plotted against the displacement of the tip midpoint (Figure 3.9a). The energy storage exhibits a markedly nonlinear relationship with displacement, manifesting three discernible regimes of energy storage. Each regime was associated with a distinct configuration of the leaflets (Figures 3.9b and 3.9c). In phase I, the curvature of the leaflets had not yet undergone inversion in any direction, while in phase III the curvature was fully inverted. Phase II served as a transitional phase, during which buckling occurs in one direction only.

As the displacement of the tip midpoint can be used to quantify the effective orifice area (EOA), it can be seen that the majority of the EOA was achieved during phase II. However, this configuration lacked sufficient stability to withstand high pressures, resulting in a transition to the final configuration (phase III). The pressure threshold for transitioning from phase II to phase III was approximately 1.5 Pa. In contrast, the transition from phase I to phase II is continuous.

The final configuration permitted greater energy storage with less deformation than the preceding phases. Furthermore, the dynamics of energy storage and pressure threshold transitions were analogous for both mesh sizes, indicating that spatial convergence was achieved for this geometry. Consequently, the coarser mesh (300 μm) was selected for subsequent FSI simulations due to its adequate capture of leaflet dynamics and reduced computational cost.

3.3 Venous valve dynamics under realistic blood flow conditions

3.3.1 Numerical simulation set-up

This study presents a three-dimensional venous valve simulation using the FSI method, with an inflow rate corresponding to supine position. This configuration represents a femoral vein valve with radius $R = 5$ mm. The leaflet model (Figure 3.10) was integrated into a fluid domain, as presented in Figure 3.10, for the FSI simulation. The sinus length is equal to one diameter, and its depth is 1.2 times the radius. In this scenario, the movement of the vein wall is considered to be negligible based on Doppler ultrasound observations of patients in a supine position. This is consistent with the fact that vein wall movement is restricted by surrounding tissues. Therefore, only the deformation of the leaflets is solved, while the sinus and vein walls are considered to be rigid.

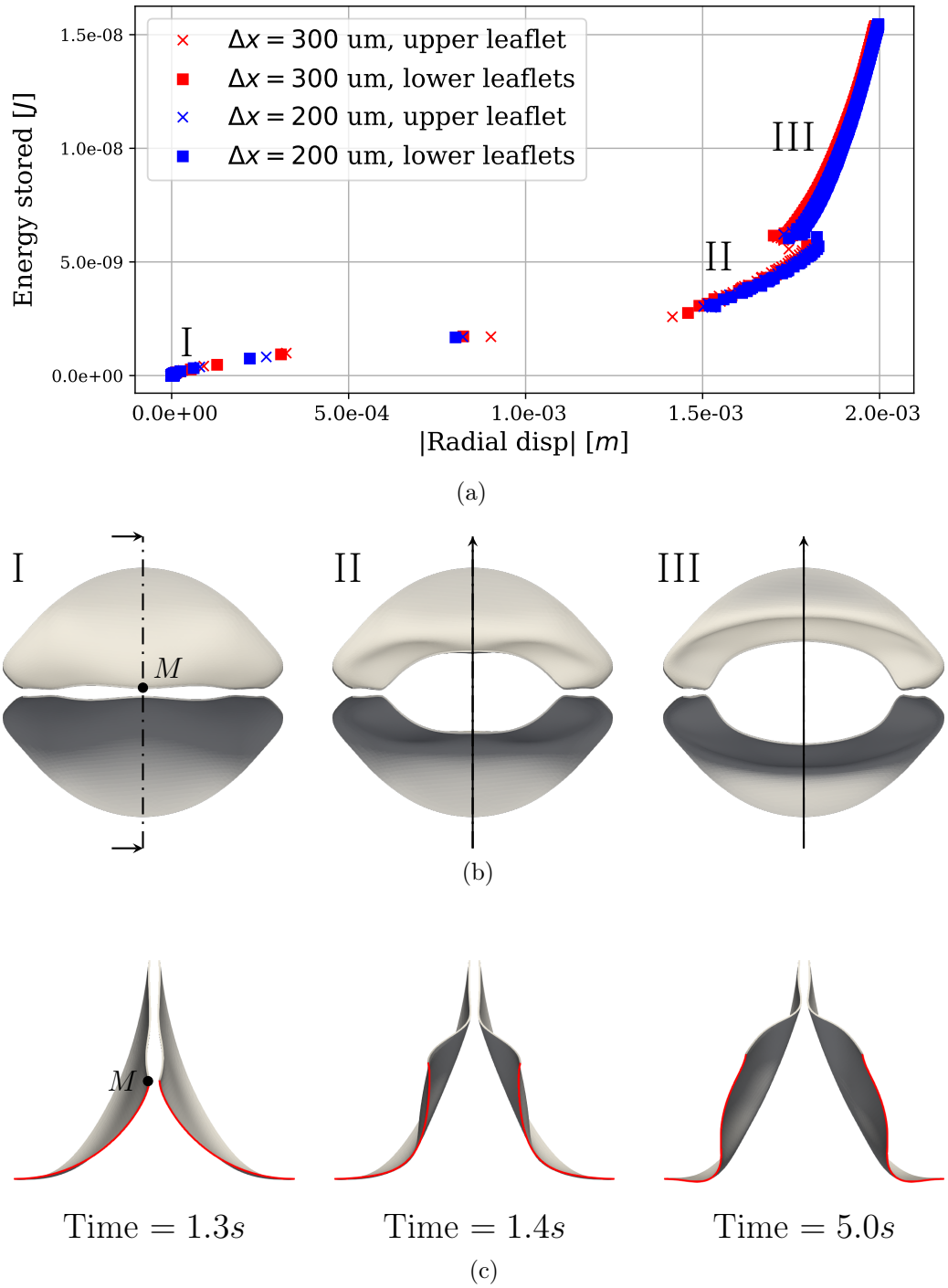

Figure 3.9: The above graph represents the energy stored by the leaflets relative to the displacement of the middle point of the free edge. Below, the corresponding leaflet shapes are illustrated for each phase (I, II, III).

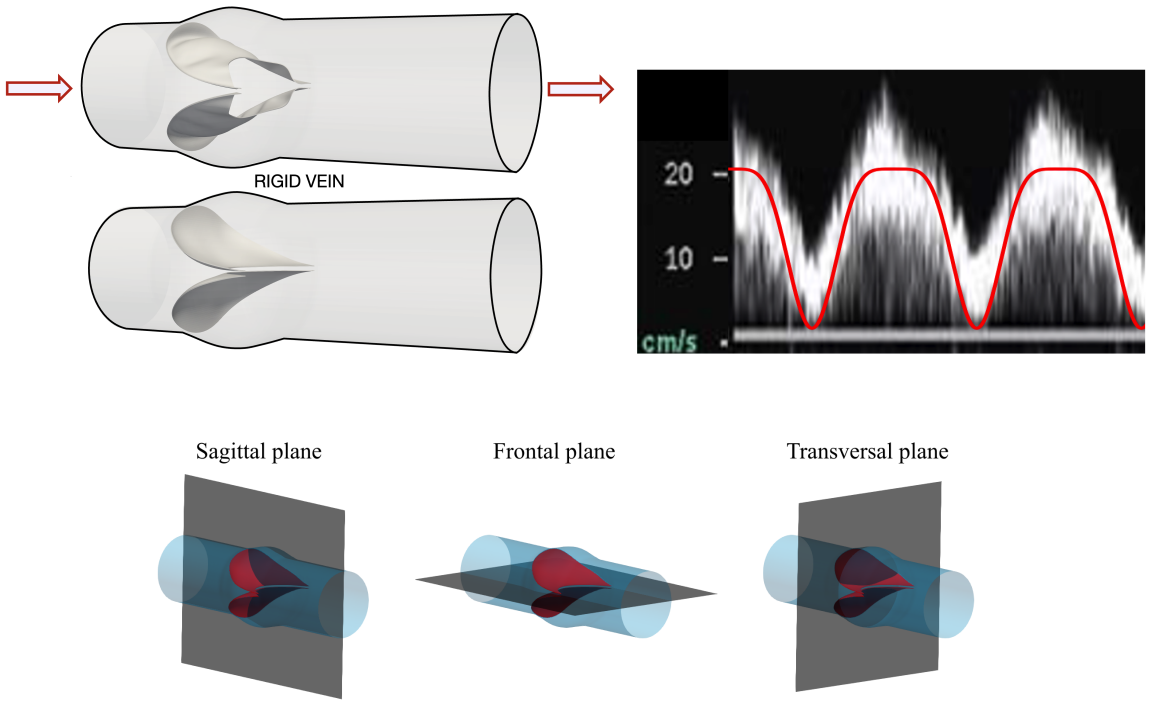

Figure 3.10: Fluid and structural configuration. The inlet is located on the left, and the outlet on the right. Arrows indicate the flow direction.

The leaflets are modeled as a neo-Hookean material with Young's modulus $E = 0.1$ MPa and Poisson coefficient $\nu = 0.4$. A no-slip condition was imposed to both the vein wall and the leaflets. The blood is treated as an incompressible Newtonian fluid with density $\rho_f = 1050$ kg.m^{-3} and dynamic viscosity 3.3×10^{-3} Pa.s. The flow rate is 315 mL.s^{-1}, which is consistent with the findings of Kalayci et al. [170]. To match the observations in Section 3.1.2, the following temporal and spatial profile has been used for the velocity at the inlet:

$$\mathbf{v}_{axial}(r,t) = v_{max}(1 - r^2/R)(1.01 - |\cos^5(\pi t/T)|) \tag{3.4}$$

with period $T = 1$ s and peak velocity $v_{max} = 0.2$ m.s^{-1}. This temporal profile replicates a short respiratory pump cycle (see Figure 3.10), and the spatial profile is parabolic. The Reynolds number at v_{max} is 300, and the associated Womersley number is 2.8. Six cycles were simulated, and the valve dynamics stabilized after the first cycle. To ensure that the influence of initial conditions is negligible, the third cycle was used for analysis. The labeling of the planes used in subsequent analyses is illustrated in Figure 3.10c.

3.3.2 Global description of the valve dynamics

The overall dynamics of the valve cycle is presented in Figure 3.11. The top-left graph depicts the pressure loss across the valve, which is calculated as the pressure difference between two points: one situated three diameters downstream from the

valve and the other one diameter upstream. The maximum pressure loss across the valve is $\Delta p_{v,max} = 40$ Pa (0.3 mmHg), which corresponds to a bulk velocity of 0.27 m.s^{-1}. Once the valve is opened, the pressure loss stabilizes at approximately 25 Pa (0.20 m.s^{-1}).

Based on the mean leg length of 0.89 m [216] and the average valve spacing of 4 cm, there are approximately 23 valves per leg. The maximum total pressure loss from the foot to the hip would therefore be $23 \times \Delta p_{v,max} = 920$ Pa = 6.9 mmHg, which is low enough to ensure efficient blood return to the heart. The valve exhibits sufficient pressure sensitivity to open with minimal pressure loss, which is notably lower than the 13.7 kPa (103 mmHg) required for full opening of a valve model without surface reserve, as previously demonstrated in [76].

The low pressure loss also results in reduced mechanical stress in the leaflets (Figure 3.12, top row), in comparison to the ultimate tensile strength found in [177]. Moreover, the leaflets experience minimal deformation, with a maximum strain of 3%, as illustrated in Figure 3.12, bottom row.

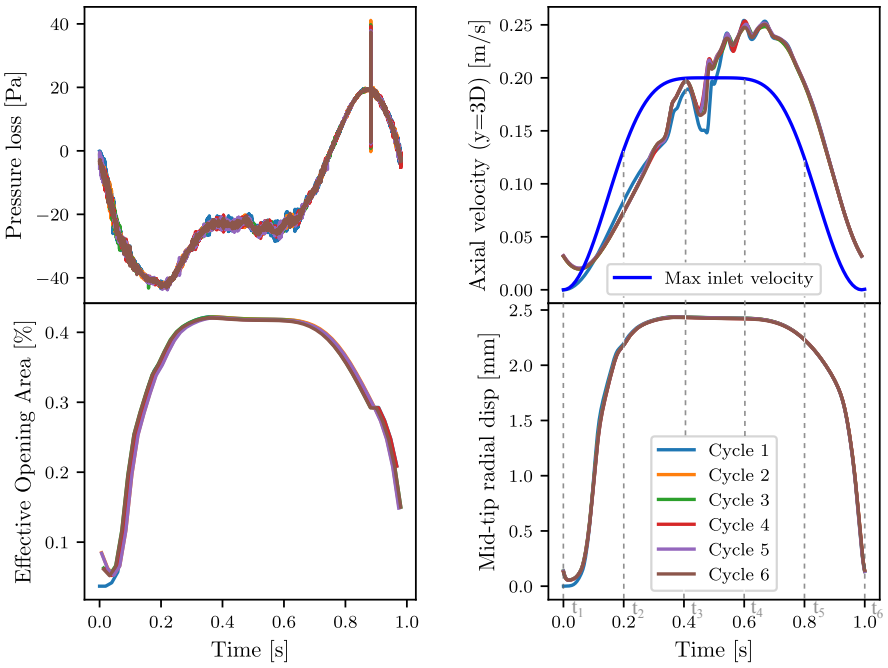

Figure 3.11: Top-left: Pressure loss through the valve at its center, with probes located 40 mm apart (one distal and one proximal to the valve). Top-right: Velocity at 3 diameters downstream of the valve. Bottom-left: Effective opening area of the valve. Bottom-right: Displacement of the mid-point of one leaflet tip. Each cycle is plotted in a different color.

3.3.3 Effective Opening Area (EOA) estimation

The bottom-left graph in Figure 3.11 displays the effective opening area (EOA) of the valve, a pivotal metric that gauges the valve's capacity to permit blood flow. This

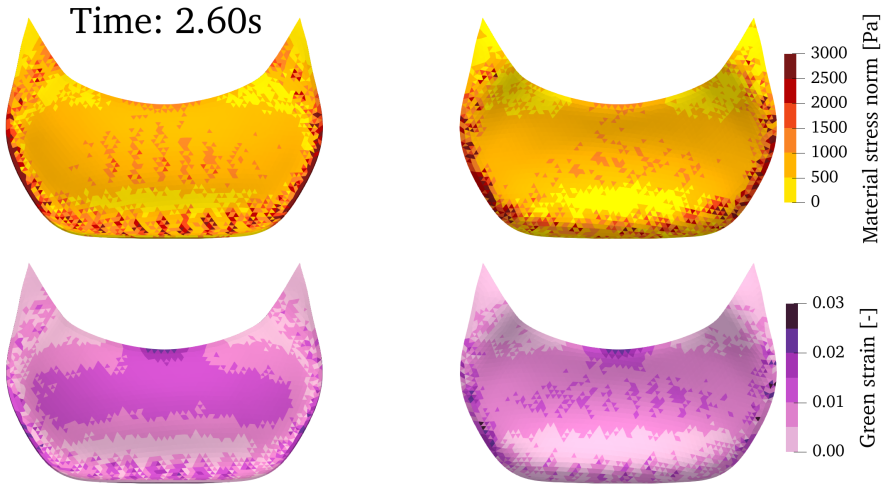

Figure 3.12: Snapshots of the leaflets during the 3^{rd} cycle at $t = 2.60$ s. The top row shows the material stress field (i.e., 2^{nd} Piola-Kirchhoff stress, Equation (2.66)), and the bottom row shows the field of the Green-Lagrange strain tensor trace(Equation (2.63)).

indicates the extent of valve blockage. In this study, two methods were employed for the estimation of the EOA. The initial method entails approximating the valve's cross-sectional area as an ellipse. The major axis is defined as the radius of the vein, denoted as R. The minor axis is defined as the radial displacement of the mid-tip point on the leaflet, represented by $u_{mid,r}$ (see Figure 3.11, bottom-right). The cross-sectional area of the valve therefore given by the formula $\pi R u_{mid,r}$, while the cross-sectional area of the vein is πR^2. The EOA is then approximated as the ratio of the mid-point displacement to the radius, expressed as $u_{mid,r}/R$. The second method, which is illustrated in Figure 3.13a and Figure 3.13b, employs Paraview software. A 2D projection view was used to determine both the inlet and valve's

(a) (b)

Figure 3.13: Images of the cross-sectional areas of the inlet (a) and valve (b) used to calculate the effective opening area (EOA).

cross-sectional areas. The inlet area, colored in black (Figure 3.13a) over a white background, was calculated by enumerating the number of black pixels within the image. Similarly, for the valve area, the valve was colored in white on top of the inlet black cross-sectional area masking the parts of the inlet. The true EOA was calculated as the ratio of the number of black pixels corresponding to the valve area to the number of black pixels corresponding to the inlet area.

The first method, with a maximum radial displacement of 2.5 mm, yielded an EOA of 50%. However, the second method yielded a maximum EOA of 42%, indicating that the initial method overestimated the EOA by nearly 20%. This discrepancy indicates that approximating the valve cross-section as an ellipse may not be very accurate. Accordingly, the second method (real EOA) was employed for the remainder of this study. The 42% EOA found here is lower than the 65% reported by Lurie et al. The maximum EOA is observed at 0.35 s into the cycle and remains at approximately 40% until the closing phase begins. The minimal EOA, which is below 5%, is observed at 0.04 s. The transition from the minimum EOA to 40% (the opening phase) occurs in approximately 0.2 s, whereas the closing phase takes around 0.35 s. A similar pattern was observed in the validation test case discussed in Section 2.6.6. The temporal profile used for the inlet results in a continuous blood flow through the valve as it closes, exerting a resistive force on the leaflets. This resistance results in a slower rate of closure than opening. The same dynamics are observed for the mid-tip radial displacement (Figure 3.11, bottom-right). It is notable that the valve never reaches a fully closed state, which may have implications for the movement of blood in the sacs. It would be beneficial to test the different inflow temporal profile in order to better understand this hypothesis.

In regard to the EOA formulation presented in Equation (3.3), the calculated value of 67% exceeds the actual EOA. Hence, Equation (3.3) is not a suitable estimation of the EOA.

3.3.4 Proximal hemodynamics

The hemodynamics within the valve is illustrated in Figures 3.14, 3.15, and 3.16. Figure 3.14 illustrates the flow dynamics within the sinus at the onset of cycle 3, showcasing the pathlines of massless particles seeded using the aforementioned methodology (rendered in Paraview). Three distinct regions and associated regimes were identified.

1- In the lower portion of the sinus, the particles remain in proximity to their initial injection locations. Such particles are not advected by the flow and remain trapped in this region.

2- In the vicinity of the leaflet tips, the particles are initially propelled away from the sinus and towards a stagnation point, designated as point A in Figure 3.14a. From this point, a portion of the particles reverse their direction of flow and enter the bags, while the remainder flow into the wake of the valve commissures and then towards the commissures. Subsequently, the particles return to the sinus, forming a vortex ring-like structure. This flow pattern is illustrated in

Figure 3.14a. For particles injected at the onset of cycle 3, those advected into this structure ultimately exit the sinus after several cycles.

3- In the intermediate zone, the particles follow the movement of the leaflets, oscillating back and forth. During their residence within the sinus, the particles display a noteworthy degree of movement. This region serves as a buffer zone between the other two regions.

To provide additional support for this description, a video of the pathlines is available for viewing at `https://youtu.be/z4Ttjdw8WUY`. The presence of Region 1 is attributed to the limited movement of the leaflets near the base, which depends

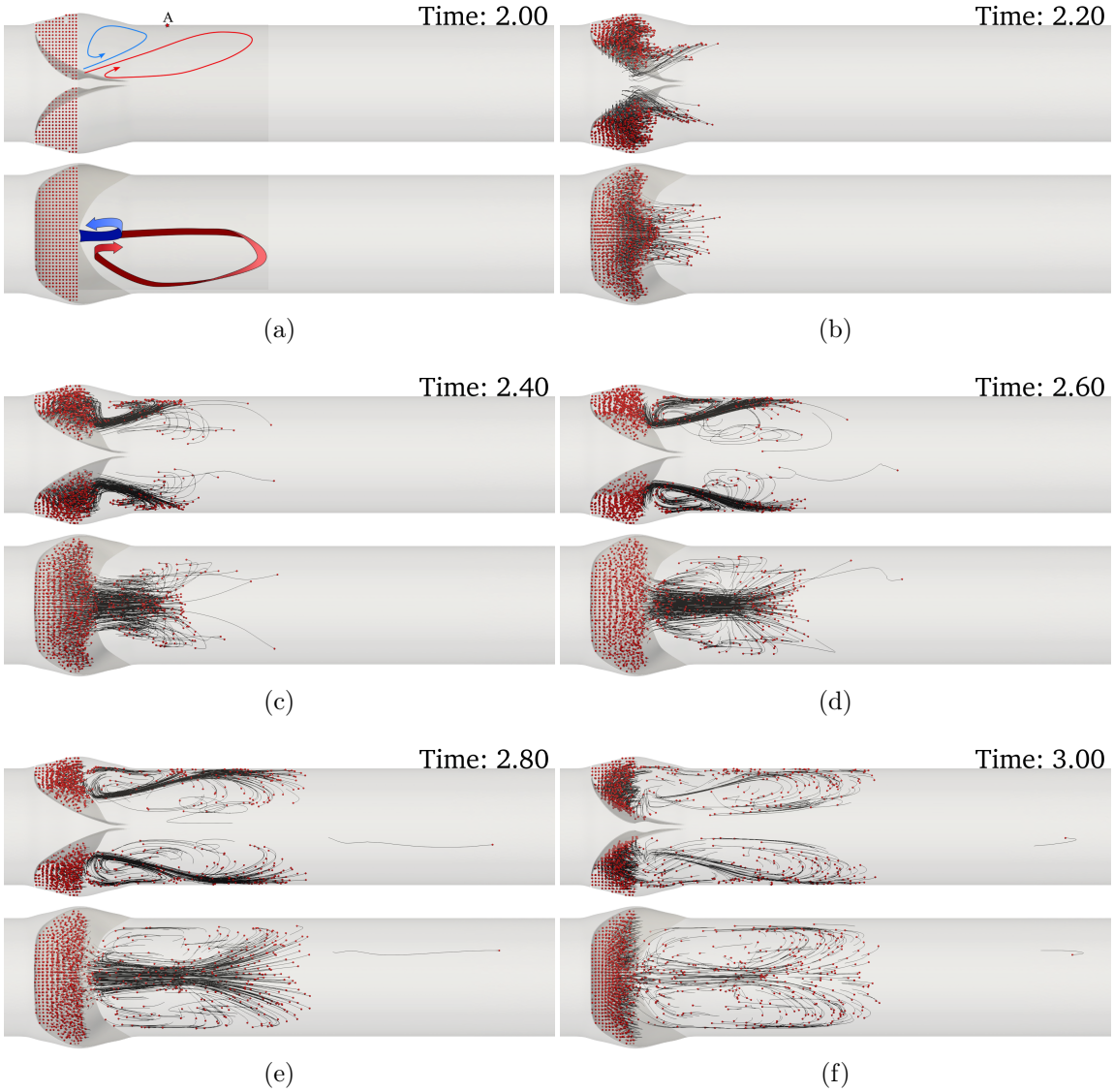

Figure 3.14: (a) Seeded tracers at $t = 2$ s inside the sinus (beginning of cycle 3, t_1 in Figure 3.11). Snapshots (b, t_2) through (f, t_6): Pathlines during cycle 3 at various instants. Sagittal (top) and frontal planes (bottom) are displayed for each instant.

on the geometric model. This may be due to either the leaflet geometry or the assumption of a rigid vein wall. It is recommended that the angle between the leaflet base and the vein wall be either relaxed or that the deformation of the vein wall be accounted for.

The downstream blood flow is depicted in the sagittal and frontal plane in Figures 3.15 and 3.16 t, respectively. The axial velocity snapshots of the sagittal and frontal planes of the valve (Figure 3.15, left, and Figure 3.16, left) illustrate several elements of the complex flow structure discussed earlier. Backward flow is observed in the wake of the leaflet commissures (Figure 3.16e) and behind the leaflet tips (Figure 3.15e). The presence of these backward-flow regions gives rise to the formation of shear layers, as illustrated in the vorticity maps (Figure 3.15, right, and Figure 3.16, right). In the sagittal plane, the flow expands behind the leaflet tips, while in the frontal plane, it is confined toward the center of the vein. The interaction of these phenomena results into a 90° reorientation of the flow in the cross-section of the vein. Accordingly, the subsequent valve must accommodate this reorientation in order to maintain the proper flow direction, as observed in the studies referenced in this paper, namely, those by Lurie and Kistner [191] and Chen et al. [74]. However, the absence of helical flow calls into question the hypothesis proposed by [74, 191]. Further analysis of helicity is necessary to fully assess this point.

The wall shear stress (WSS) on the sinus wall is illustrated in Figure 3.17. As the WSS distributions on the sinus side of the leaflets and the sinus wall are similar, only the latter is displayed. The maximum WSS is reached during the valve's opening and closing phases, with values of approximately 0.1 Pa across most regions except the base of the sacs. This value is markedly lower than the WSS observed in the lumen, which can reach up to 11 Pa. Upon reaching its maximum opening, the valve exhibits a WSS in the sinus region drops below 0.02 Pa. Once the fluid has reached a steady state, namely after 0.4 s of the cycle, a region of low WSS emerges, situated approximately half a diameter downstream of the leaflets. This region of low WSS corresponds to the vortex ring structure observed in the pathlines (Figure 3.17d, point A).

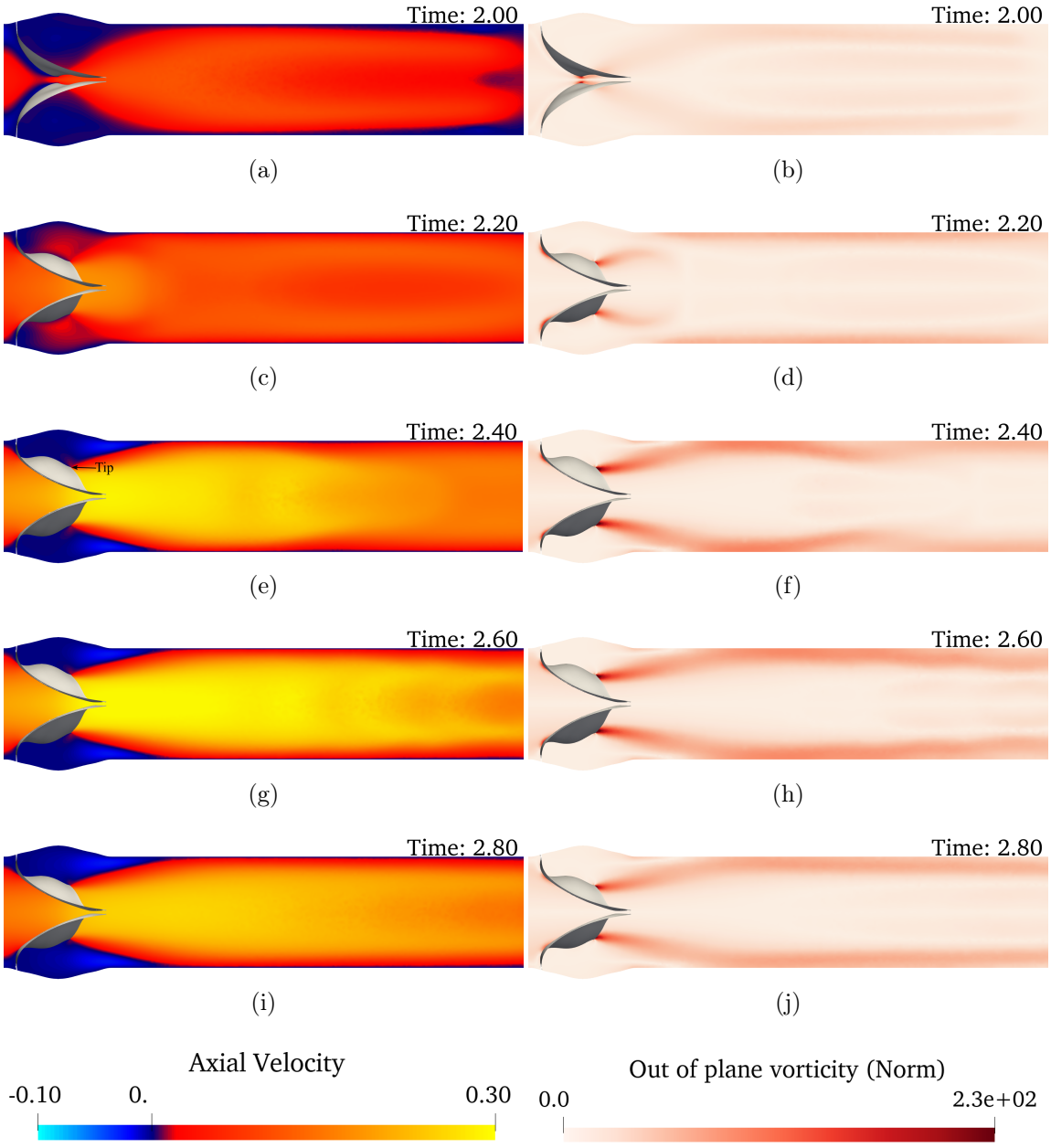

Figure 3.15: Sagittal plane snapshots of the axial velocity (left) and the norm of the out-of-plane vorticity (right) from t_1 to t_5 (top to bottom). Red indicates flow toward the heart, blue indicates backward flow. The outlet is located far after the right edge of each image.

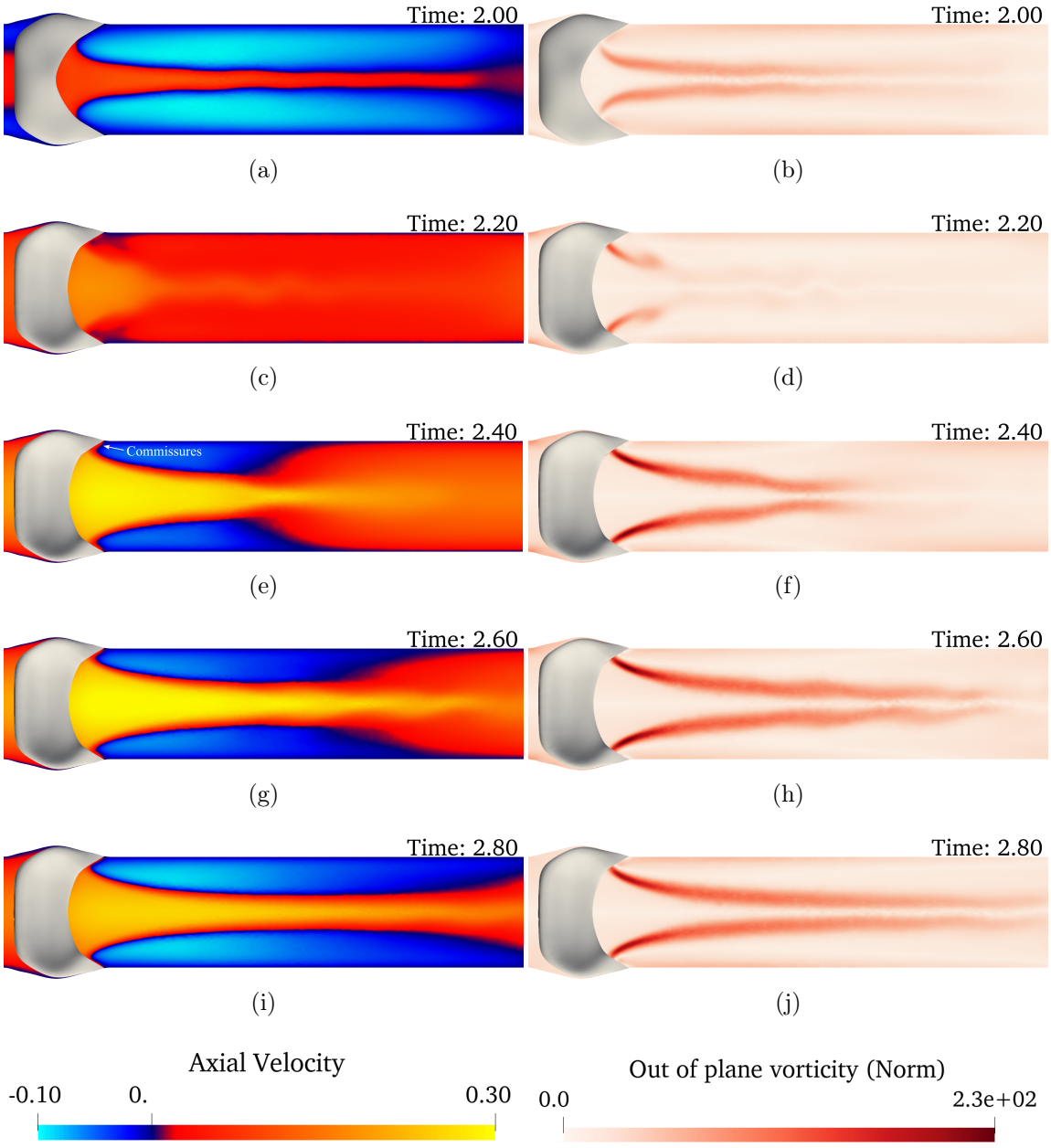

Figure 3.16: Frontal plane snapshots of the axial velocity (left) and the norm of the out-of-plane vorticity (right) from t_1 to t_5 (top to bottom). Red indicates flow toward the heart, blue indicates backward flow. The outlet is located far after the right edge of each image.

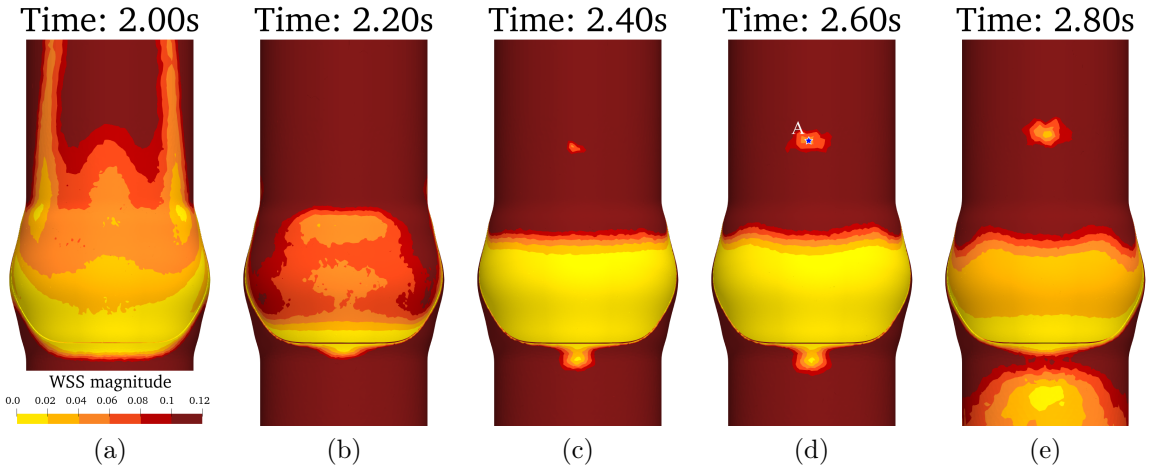

Figure 3.17: Wall shear stress magnitude on the perivalvular vein wall from t_1 to t_5.

3.3.5 Residence time inside the valvular bags

In the context of DVT, the residence time of blood within the sinus is a critical parameter. The residence time is defined as the time required for a particle to leave the sinus after being injected. To this end, massless particles are seeded uniformly within the sinus at the onset of each cycle. Subsequently, the percentage of particles remaining in the sinus at each instant is calculated. The results are presented in Figure 3.18a. The particle dynamics within the sinus demonstrates an inverse relationship with the valve. During the opening phase, the percentage of particles in the sinus decreases until it reaches a plateau. Thereafter, it increases to a local maximum during the closing phase (noted L_i on Figure 3.18a). $V_{\mathrm{to\ drain}}$ at the end of the cycles decreases from one cycle to the next, which values are used to model the residence time. As it seems to follow an exponential decrease, $V_{\mathrm{to\ drain}}$ is plotted in logarithmic scale in Figure 3.18b. Subsequently, the residence time is estimated by a logarithmic fit on the 4 last values of $V_{\mathrm{to\ drain}}$ at the end of each cycle. For instance, the requisite number of cycles to drain 95% and 99% of the particles is 42 and 68, respectively. In other words, 5% of the particles remain in the sinus for 42 s, and 1% for 68 s.

Table 3.1: Ratio of the successive local maximums of the percentage of particles in the sinus for each seed.

Injection	$\frac{\mathrm{L}_1}{\mathrm{L}_0}$	$\frac{\mathrm{L}_2}{\mathrm{L}_1}$	$\frac{\mathrm{L}_3}{\mathrm{L}_2}$	$\frac{\mathrm{L}_4}{\mathrm{L}_3}$	$\frac{\mathrm{L}_5}{\mathrm{L}_4}$	$\frac{\mathrm{L}_6}{\mathrm{L}_5}$
Cycle 1	0.6973	0.8973	0.9235	0.9313	0.9432	0.9437

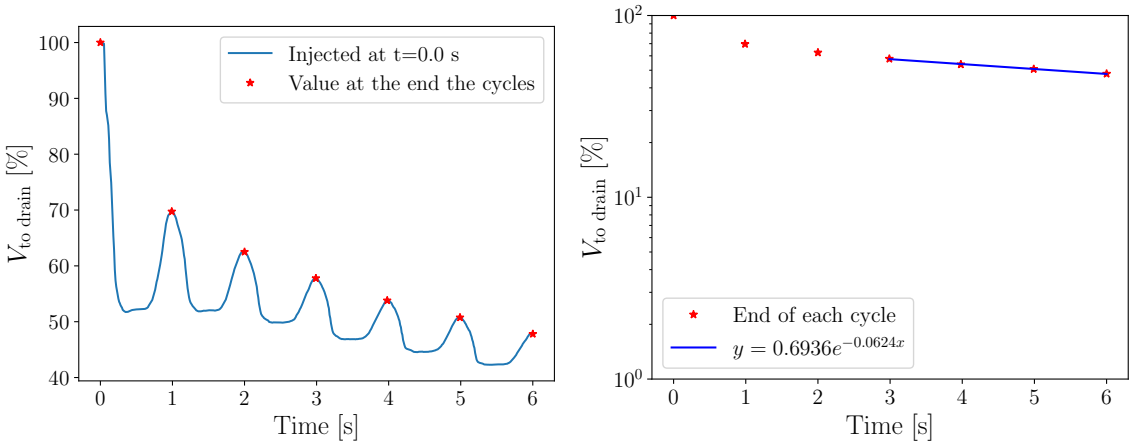

(a) (b)

Figure 3.18: (a) Plot of the percentage of particles in the sinus with respect to time. The injection is done uniformly in space at the start of the simulation. The values at the end of each cycle are marked with the red stars. (b) Logarithmic plot of the percentage of particles in the sinus. The blue curve plots the logarithmic fit made with the 4 last values.

3.3.6 Discussion

In conclusion, a novel 3D model of a vein valve has been developed based on the surface reserve hypothesis. A preliminary structural analysis of the leaflets was conducted to gain insight into their dynamic behavior under controlled mechanical loads. The pressure sensitivity required for opening was found to be sufficiently low to accommodate physiological conditions. Subsequently, a case study was presented in which a femoral vein valve was subjected to a short respiratory pump inflow. This valve exhibited good pressure sensitivity, ensuring opening with minimal pressure loss, in contrast to stretch-opening models that have been previously described in the literature. The EOA of the present model remains lower than the physiological values found in the literature, indicating that the model's geometry should be refined or that an alternative inflow profile should be tested.

Additionally, this study demonstrated the formation of a vortex ring-like structure in the downstream region of the leaflets, accompanied by a 90°reorientation of the flow in the transverse plane. The hypothesis that helical flow is responsible for this reorientation was rejected.

Two significant issues were identified: incomplete closure of the leaflets and minimal particle movement at the base of the sacs, impeding the efficient drainage process in this geometry. Further research should be conducted to ascertain whether these behaviors are influenced by the inflow temporal profile, the location of the valve (e.g., diameter) or the geometry of the leaflets. The following chapter will address these concerns and introduce further studies based on the findings presented here.

Chapter4

FSI simulations of veins valves

Chapter overview: *In this chapter, three studies of the hemodynamics of venous valves will be carried out, guided by the following questions:*

- ***How are valve dynamics modulated by the geometric and hemodynamic conditions along the deep venous system of the leg?*** *In Section 4.1, three sizes of venous diameter are considered to mimic blood flow in a popliteal, femoral and common femoral vein valve. The geometry of the leaflets is the same as shown in Section 3.2. The dynamics of the leaflets, the development of the blood flow and the wall shear stress on the sinus wall are compared.*
- ***Does a higher inlet blood flow renew the blood in the sinuses, as in a calf muscle pump configuration?*** *Section 4.2 present one of the cases of Section 4.1 submitted to a calf muscle pump inlet blood flow to assess its effect on valve dynamics and sinusoidal flow, compared with the supine position blood flow.*
- ***In a system of consecutive valves, does the blood flow from the first valve influence the dynamics of the second valve?*** *A case of venous valves in series corresponding to common femoral vein valves is presented in Section 4.3. First, the dynamics of the first valve are compared with the corresponding single valve case. Finally, the flow and dynamics of the two valves are analyzed to assess the effect of having a series of valves.*

Contents

4.1 Vein valves: associated hemodynamics along the lower limb

4.1.1 Presentation of the cases' geometry

The objective of this study is to examine the impact of hemodynamics on the deep venous system, with a particular focus on the segment extending from the knee to the hip. This encompasses an evaluation of flow development, flow characteristics, and wall shear stress within the venous sinus.

Three cases are considered in this study. The PV case represents the popliteal valve, the FV case represents the femoral valve, and the CFV case represents the common femoral valve. Please refer to Figure 3.1 for details of the various case locations in the deep venous system (circled in red). The geometry employed in each case is that described in Section 3.3, which pertains to venous valve dynamics under realistic blood flow conditions. The diameter of the vein is 6 mm, 10 mm, and 14 mm for the PV, FV, and CFV cases, respectively (see Section 3.1.1 for details on the physiological vein size). The thickness of the leaflets is 70 µm for the PV and FV cases, and 100 µm for the CFV case. The length and depth of the sinus are fixed at one and one-and-a-half vein diameters, respectively. Further details regarding the geometry can be found in Table 4.1. The dimensions have been selected to assess the impact of vessel size through two distinct approaches: firstly, by varying the diameter while maintaining the same leaflet thickness (PV and FV cases), and secondly, by maintaining the same ratio of leaflet thickness to diameter (FV and CFV cases). This methodology is designed to fully characterize the valve dynamics and the flow within the sinus in relation to vessel diameter, which values are discussed in Section 3.1.1.

Table 4.1: Characteristics of each case.

Case Parameters	**Popliteal**	**Femoral**	**Common Femoral**
Case Denominations	PV	FV	CFV
Diameter (mm)	6	10	14
Leaflet Thickness (µm)	70	70	100
Sinus Length (mm)	6	10	14
Sinus Depth (mm)	7.2	12	16.8

To define the velocity-time profile in terms of the normalized time within each cycle, we introduce t_c as the time modulo the breathing period $T_{breath} = 1.2$ s of the cycle, i.e., $t_c = t \mod T_{breath}$. This means that t_c resets to zero at the start of each new cycle and varies within the interval $[0, T_{breath})$. The velocity profile is then given by:

$$v(t) = \begin{cases} v_{\max}\left(1 - \left|\cos^5\left(\pi t_c / T_{cos}\right)\right|\right) & \text{for } t_c < T_{cos} = 1, \\ 0 & \text{for } t_c \geq T_{cos}. \end{cases} \tag{4.1}$$

Here, $v_{\max}$ represents the maximum velocity (see Table 4.2). During $T_{cos} = 1$ the blood flows through the inlet of the domain, then the blood flow is stopped for the rest of the cycle (i.e. 0.2 s). This profile is similar to that presented in Section 3.3.1 but extended for 0.2 s after the cosine with a null inlet velocity.

4.1.2 Computational set-ups

The simulations are based on several simplifications and assumptions. The vein wall is assumed to be rigid, and the thickness of the leaflets is maintained at a constant value. The leaflets are positioned in a closed configuration, which is assumed to be stress-free. Each case parameters employed in the simulations are detailed in Table 4.2.

The computational time is comparable for the PV and FV cases, but the CFV case is more computationally expensive. The PV and FV cases were executed on 192 cores (80 for the solid, 112 for the fluid) of the ADASTRA HPC cluster of GENCI/CINES for 1.2 s of physical time, resulting in a total runtime of 24 h. The CFV case requires 36 h to run on the same configuration for 1.2 s of physical time. The computational time can be broken down into three main components: approximately 30% of the computational resources are allocated to solving the structural problem, 30% to solving the mesh movement, and 20% to 30% to the dynamic mesh adaptation. The high cost of solving the solid problem, which is also a pseudo-solid problem due to the mesh movement, is attributed to the preconditioning of the linear solver. A straightforward Jacobi preconditioning technique is employed. The method demonstrates excellent results when the linear system matrix is diagonally dominant. Nevertheless, substantial sparse matrices with non-diagonally dominant structures frequently emerge from structural problems, which constrains the efficacy of the Jacobi preconditioning technique. The implementation of an enhanced preconditioning technique for the structural linear solver would markedly reduce the

Table 4.2: Physical, mesh, and numerical parameters for each case.

Physical parameters			
	PV	**FV**	**CFV**
Fluid			
Diameter (m)	0.006	0.01	0.014
Density ρ_f $(kg \cdot m^{-3})$	1050		
Viscosity ν $(m^2 \cdot s^{-1})$	3.3×10^{-6}		
Bulk velocity $(m \cdot s^{-1})$	0.16	0.2	0.2
Reynolds number	150	320	450
Solid			
Density ρ_s $(kg \cdot m^{-3})$	1050		
Young's modulus E (MPa)	0.1		
Poisson's ratio ν *(-)*	0.1		
Mesh parameters			
Fluid			
Δ_x *close to the leaflets* (μm)	50	70	100
Δ_x *away* (μm)	150	210	300
Solid			
Δ_x (μm)	70	70	100
Numerical parameters			
Fluid			
Time integration	LSRK4 (2.15)		
Mesh movement	Pseudo Solid (2.6.1)		
$R_{min,PS}$ *(mm)*	0.100	0.140	0.200
$R_{max,PS}$ *(mm)*	0.50	1.05	1.50
Solid			
Time integration	Newmark (2.4.4.2)		
Decay factor γ	0.0		
Contact	Penalty method (3.3.1)		
$F_{max,contact}$ *(Pa)*	200	200	200
δ_{offset} (μm)	25	50	50
$l_{activation}$ (μm)	50	50	100
Material model	Neo-Hookean (2.73)		
Coupling			
Subiterating procedure	Aitken (2.6.5)		

computational expense.

4.1.3 The different valves' dynamics

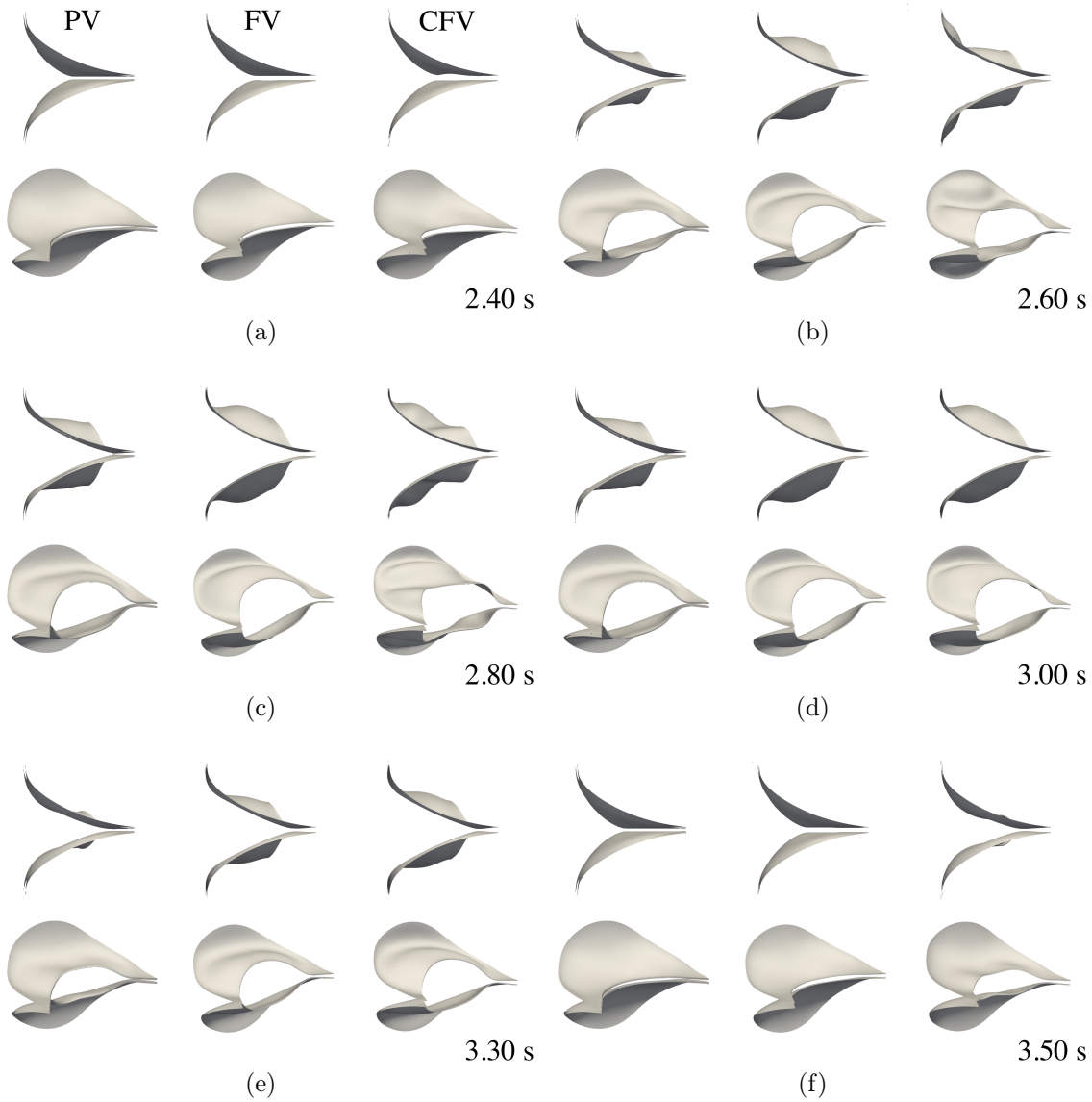

Figure 4.1: Leaflet dynamics at different times of the third cycle. In each time snapshot, the top views are in the sagittal plane, and the bottom views are taken from three-quarters downstream of the valve. The corresponding instants of the snapshots are indicated by the grey dashed lines in Figure 4.2a.

The dynamics of the leaflets display disparate behaviors across the three cases. Valve positions in the third cycle (which is sufficient to obtain results independent of the initial conditions, see Section 3.3.2) are presented in Figure 4.1. In the PV case, the leaflets only partially open, corresponding to phase II as described in Section 3.2, while in the FV and CFV cases, the leaflets undergo complete buckling, reaching

phase III (Figure 4.1d). It is noteworthy that in the FV case, the leaflets open from their tips, whereas in the CFV case, the opening occurs at the base (see Figures 4.1b and 4.1c). These dynamics are further illustrated in Figure 4.2a. The effective orifice area (EOA) differs between the three cases, with the PV case achieving 32%, while both the FV and CFV cases reach 42% observed at 0.35 s and 0.45 s in the third cycle, respectively. Note that the leaflets start their movement at an earlier time in the FV and CFV cases compared to the PV case. The closing phase of the PV case appears to exhibit a high degree of symmetry with the opening phase, whereas the FV and CFV cases display distinct characteristics during the closing process. The distinct dynamics of closing obtained for the three cases are attributed to added-mass effect but the added-mass have not been quantified in this study.

To compare the pressure loss between cases, and as the absolute pressure loss scales with the distal dynamic pressure, Figure 4.2b illustrates the dimensionless pressure loss across the valve. The maximum pressure loss to the distal dynamic pressure is observed in the PV case, which is consistent with the reduced EOA observed for this case. The PV valve leads to a higher . In terms of absolute pressure, 40 Pa is the maximum observed in the CFV case, which remains sufficiently low to ensure the return of blood to the heart under physiological conditions. It is evident that the pressure dynamics of the PV case differs significantly from those of the FV and CFV cases. The PV case demonstrates only a plateau phase, whereas the FV and CFV cases exhibit a first pressure peak around 2.6 s. Subsequently, the pressure declines to a plateau phase for the FV and CFV cases from 2.8 s to 3.1 s, followed by an inversion of the pressure gradient, which aligns with the blood deceleration phase.

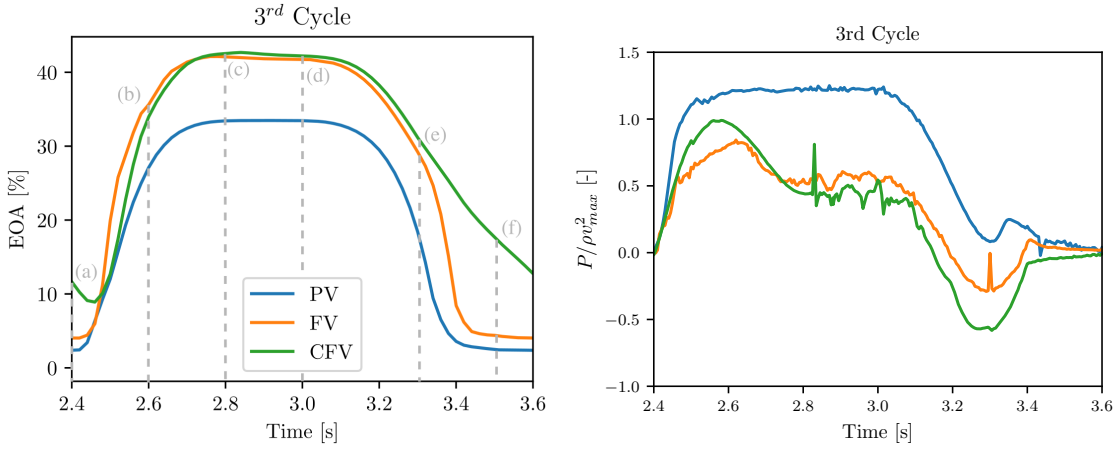

(a) (b)

Figure 4.2: (a) Effective orifice area of the third cycle for the three cases. The gray dashed lines represent the instants of the images presented in Figure 4.1. (b) Dimensionless pressure loss across the valve during the third cycle for each case. The pressure loss is the difference between the pressure at the center one diameter upstream and three diameters downstream of the valve.

4.1.4 Velocity fields and flow patterns

The development of blood flow in the wake of the valves is illustrated in the velocity images in Figures 4.3, 4.4, and 4.5. The maximum velocity at the end of the sinus, centered on the cross-section, reaches 0.306, 0.308, and 0.290 m/s for the PV, FV, and CFV cases, respectively, occurring at $t_{\text{cycle}} = 0.6$ s in each case. As illustrated in Figure 4.3, the flow develops more rapidly in the PV case compared to the FV and CFV cases. The same type of flow structure is observed behind the leaflets in all cases, as previously presented in Section 3.3.4. Mixing layers are initiated following the commissures of the leaflets, evolving into two distinct recirculations,

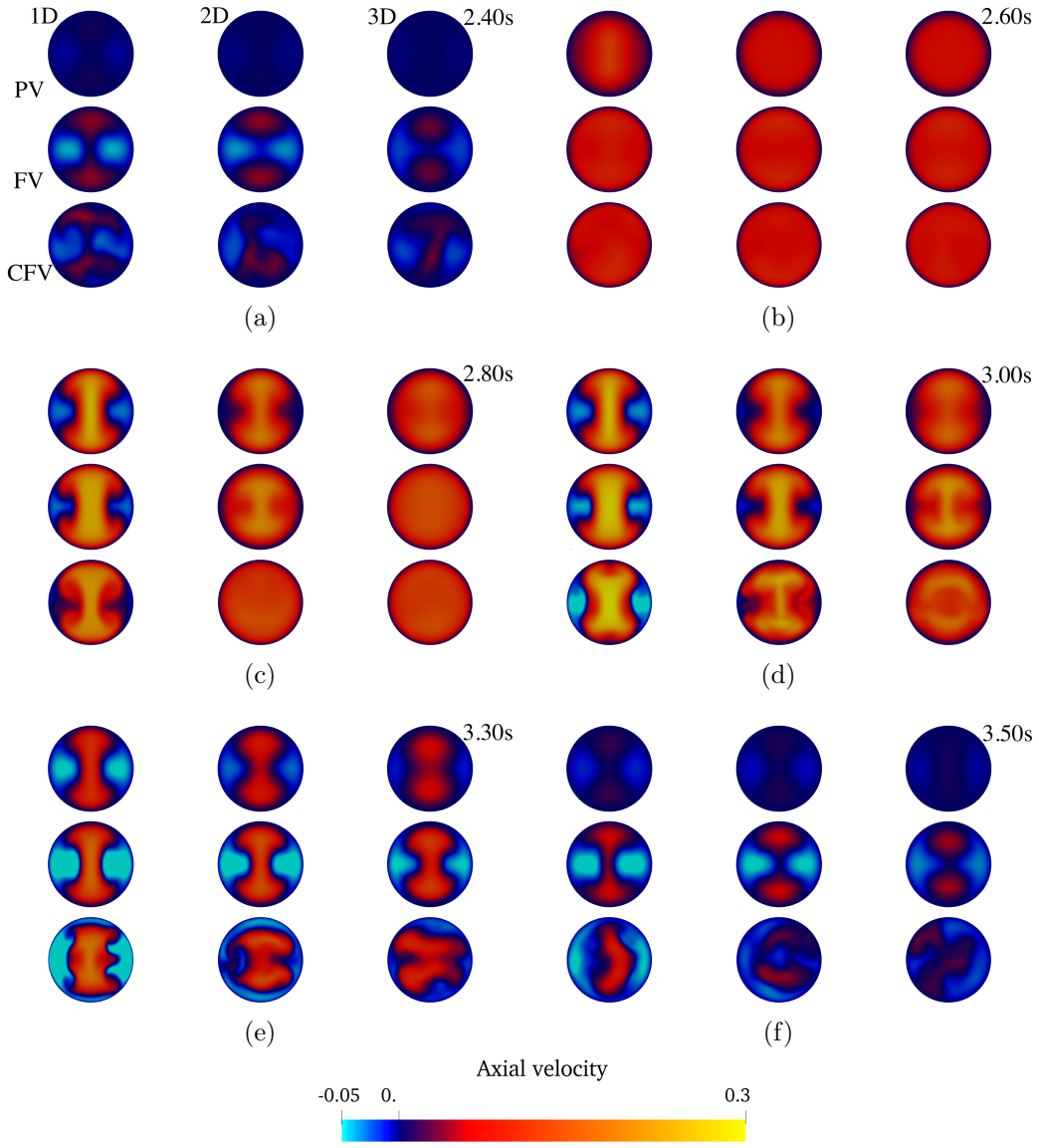

Figure 4.3: Transversal plane snapshots of the axial component of the velocity at different instants ((c) during opening, (d) plateau, (e) closing, and (f) closed phase). Red indicates flow towards the heart; blue indicates backflow.

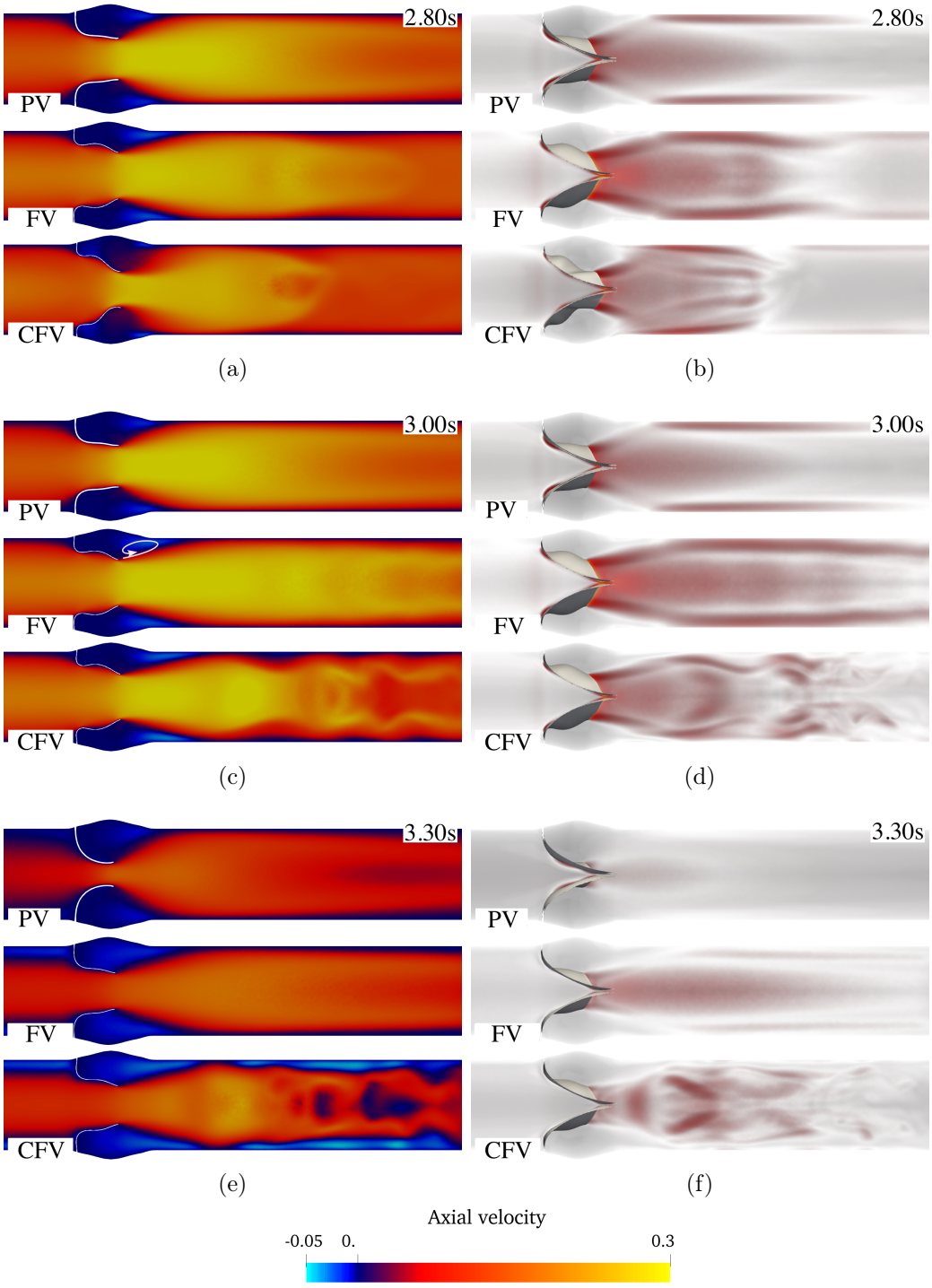

Figure 4.4: Axial velocity and vorticity in the sagittal plane snapshots during opening (a; b), plateau (c; d), and closing (e; f). Red indicates flow towards the heart; blue indicates backflow. The vorticity scale is adapted to each case; the snapshots illustrate the flow structure only.

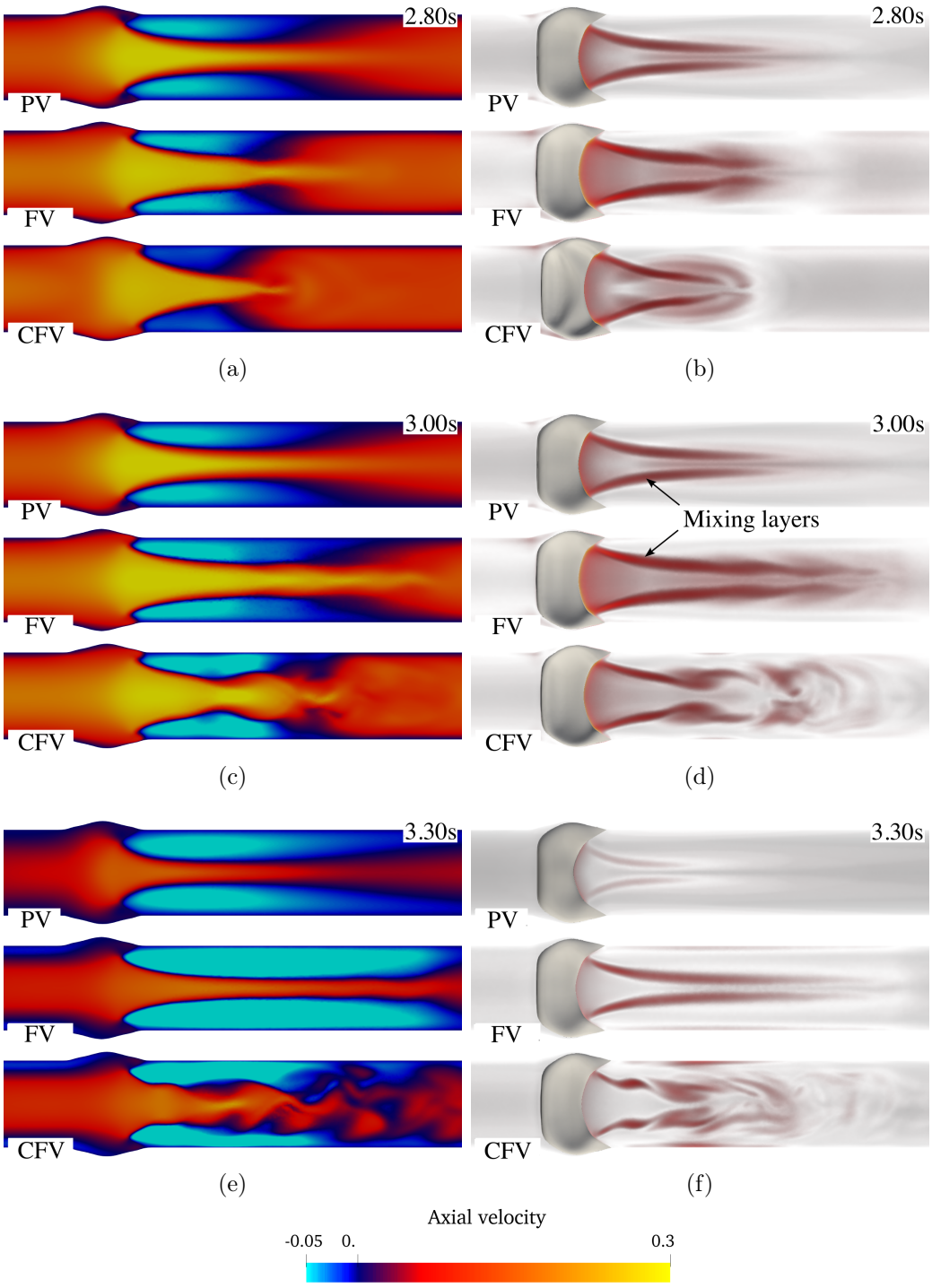

Figure 4.5: Axial velocity and vorticity in the frontal plane snapshots during opening (a; b), plateau (c; d), and closing (e; f). Red indicates flow towards the heart; blue indicates backflow. The vorticity scale is adapted to each case; the snapshots illustrate the flow structure only.

as illustrated in Figure 4.5. These mixing layers extend towards the center of the vein, with stable layers observed in the PV case and instabilities and vortex shedding arising in the FV and CFV cases, as depicted in Figure 4.5b. Similarly, the axial velocity profile of each case (with the probe situated at a distance of three valve diameters downstream from the center of the valve) also exhibits a comparable trend, as illustrated in Figure 4.6.

Two vortices emerge at the leaflet tips, resulting in an expansion of the flow towards the wall in this direction, as illustrated in Figure 4.4c. The confluence of these phenomena gives rise to the reorientation of the blood flow subsequent to the valve [186]. This adaptation is designed to minimize the impact of the valve on the blood flow, as suggested by Lurie [186]. Nevertheless, no helical flow is discerned in the wake of the valves. A spectral analysis of the velocity signals presented in Figure 4.6 was conducted to identify the frequency of the vortex shedding in the wake of the valves. The dimensionless frequencies are given as the Strouhal number, defined as $St = fD/\bar{v}_{\text{inlet}}$, where D is the diameter of the vein and $\bar{v}_{\text{inlet}}$ is the mean inlet velocity. No vortex shedding was detected for the PV case, while the FV and CFV cases exhibit vortex shedding with associated Strouhal numbers $St_{\text{FV}} = 1.66$ and $St_{\text{CFV}} = 1.98$, which are comparable to the values reported in vessel stenosis studies [217, 218], ranging from 0.93 to 2.63. The vortices mainly detach from the leaflets' commissures and are oriented in the normal direction of the frontal plane.

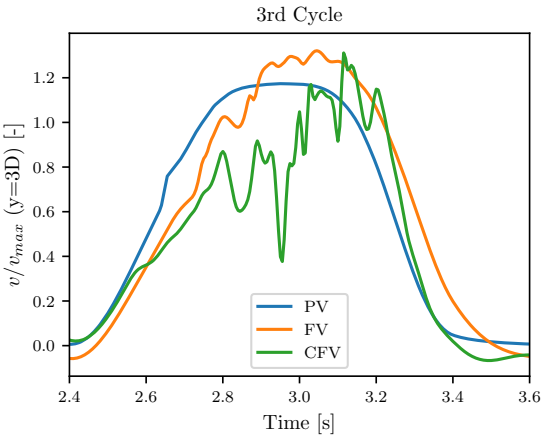

Figure 4.6: Dimensionless axial velocity at the center of the valve, three diameters in the proximal direction. The third cycle is displayed here.

4.1.5 Flow in the valve bags

To complete the analysis of the hemodynamics within the valvular sacs, massless tracers were seeded in the sinus region. Initially, the sinus region was isolated to serve as an injector. The proximal limit of the sinus was established at the initial position of the midpoint of the leaflet tips. The tracers were then released at the beginning of the simulation and were advected by the flow. The results are presented in Figure 4.7. During the opening phase, particles situated in proximity to the leaflet

tips are removed from the sinus. A vortex ring is formed in the wake of the leaflet

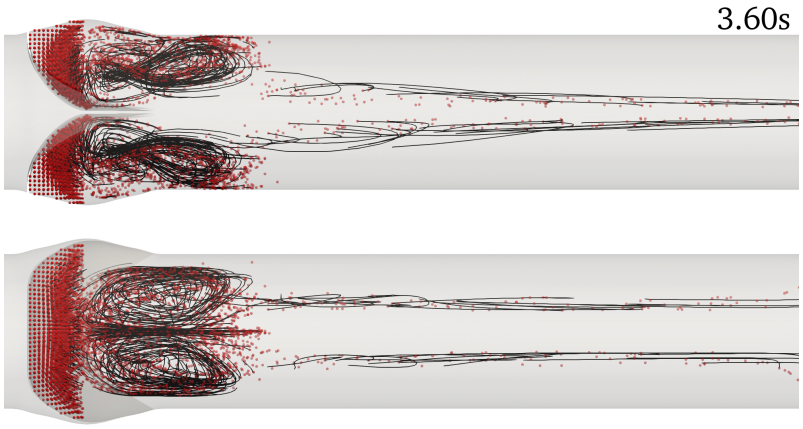

(a)

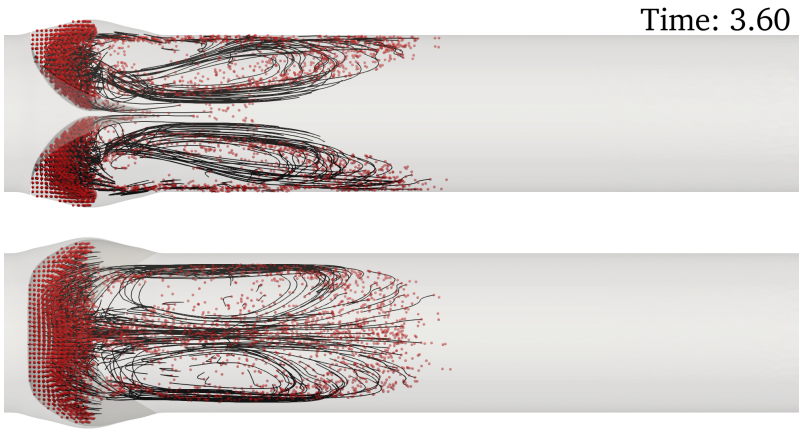

(b)

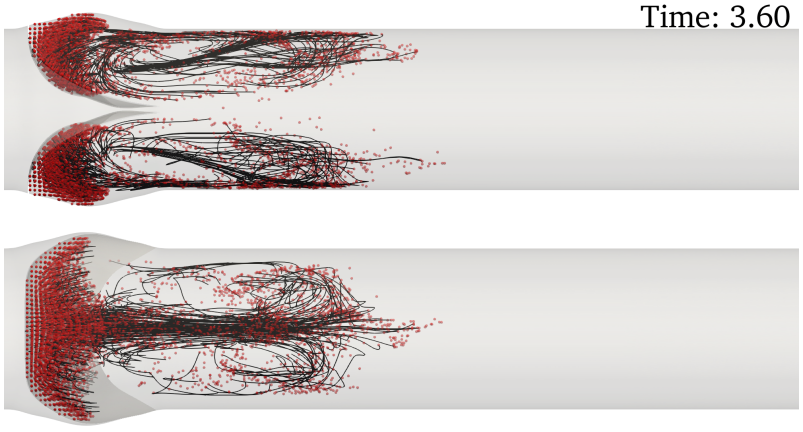

(c)

Figure 4.7: Pathlines of the particles seeded in the sinus at the outset of the third cycle for each case (top to bottom: PV, FV, and CFV cases, respectively).

tips and is located outside the sinus. Only those particles situated near the proximal outlet plane of the sinus exhibit a notable displacement from their initial positions. Conversely, the particles located towards the base of the sacs display markedly static behavior. This observation suggests that the renewal of the blood accumulated in the depth of the sinus is a challenging process, particularly within this specific geometry. The present study indicates that the larger the vein, the more efficient it is to flush the sinus as confirmed by the percentage of volume drained (see Table 4.3). The subsequent section will investigate the impact of the calf muscle pump on the valve dynamics and the flow within the sinus.

Table 4.3: Percentage of volume drained per cycle for each case. The particles are seeded in the sinus at $t = 0$ s.

Case	**Cycle 1**	**Cycle 2**	**Cycle 3**	**Complete**
PV	29.6	8.3	6.2	44.2
FV	30.4	10.1	6.9	47.4
CFV	30.5	15.5	8.4	54.5

Furthermore, the wall shear stress (WSS) dynamics exhibit notable differences across the various cases. The WSS is scaled with v/D in order to be comparable across cases. The scaled WSS maps on the parietal side of the leaflets exhibit a similar pattern to those observed on the sinus wall; therefore, only the sinus wall maps are presented in Figure 4.8. Each case displays a distinctive WSS pattern on the sinus wall. In the PV case, where the leaflets do not undergo complete buckling, the scaled WSS is observed to be lower than in the FV and CFV cases. The maximum and minimum WSS values for the FV and CFV cases are comparable, but the leaflet dynamics exert a significant influence on WSS dynamics on the sinus wall. In the CFV case, the presence of WSS persists for a longer period during the opening phase than in the FV case. In contrast, for the PV case, WSS is only present during the closing phase. Once the flow is fully developed, a low WSS zone is observed just after the end of the sinus. This takes the form of a point in the popliteal vein case and a semi-lunar shape in the other two cases.

4.1.6 Discussion

This study investigated the hemodynamics associated with venous valves along the lower limb, specifically focusing on the popliteal (PV), femoral (FV), and common femoral (CFV) veins. By analyzing valves of varying diameters and leaflet thicknesses, the impact of vessel size on valve dynamics, flow characteristics, and wall shear stress within the venous sinus was assessed.

The valve dynamics exhibited significant differences across the cases. In the PV case, the leaflets only partially opened (phase II behavior), whereas in the FV and CFV cases, the leaflets underwent complete buckling (phase III). This disparity is attributed to the scaling strategies employed: maintaining constant leaflet thickness

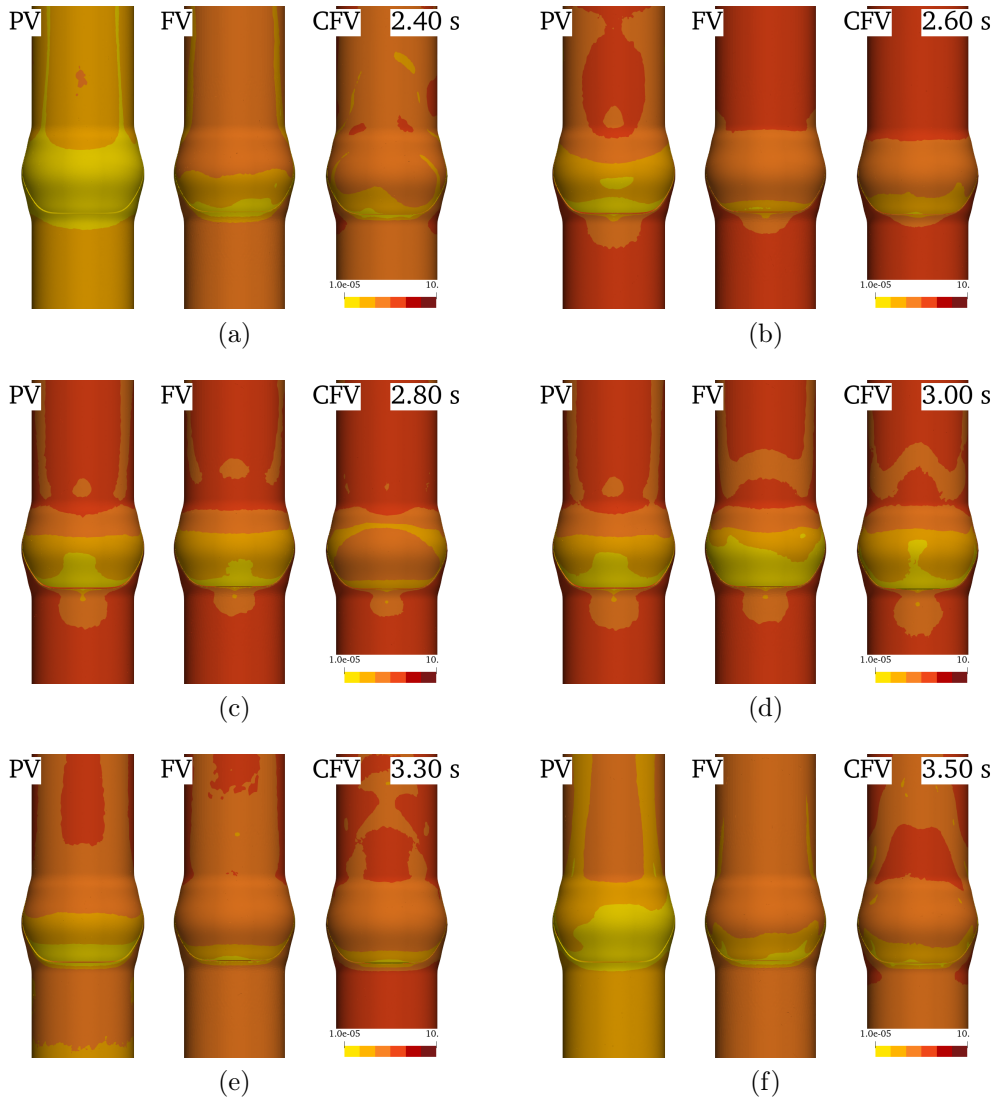

Figure 4.8: Maps of the wall shear stress (WSS) scale by v/D on the sinus wall at different times of the cycle. The color bar is in logarithmic scale.

(PV and FV cases) versus a constant ratio of leaflet thickness to diameter (FV and CFV cases). Larger veins allowed for greater leaflet mobility due to increased fluid forces overcoming structural resistance. Consequently, the effective orifice area (EOA) was higher in the FV and CFV cases (42%) compared to the PV case (32%), indicating more efficient blood flow in larger veins.

Analyzing the pressure loss across the valves revealed that the maximum pressure loss occurred in the CFV case (40 Pa), yet remained within physiological limits to ensure adequate venous return. The distinct pressure profiles—such as the plateau phase in the PV case versus the pressure peaks in the FV and CFV cases—highlight the influence of vessel diameter on hemodynamic behavior during valve opening and closing.

The study of velocity fields and flow patterns demonstrated that while the flow downstream of the PV was fully developed under pulsatile conditions, vortex shedding was prominent in the FV and CFV cases. Vortices detached from the leaflets' commissures and were oriented normal to the frontal plane, a phenomenon more pronounced in larger vessels due to higher Reynolds numbers and increased flow instabilities. These flow patterns are crucial as they can affect shear stress distributions and may have implications for areas prone to thrombosis.

The flow within the bags was investigated using particle pathlines, which indicated minimal movement of particles near the base of the sinus across all cases, suggesting potential zones of stagnation. However, the FV and CFV cases showed slightly enhanced sinus flushing compared to the PV case, implying that larger vessel diameters may improve blood renewal within the sinus and reduce the risk of thrombosis associated with prolonged residence times.

The wall shear stress (WSS) dynamics varied notably among the cases. The PV case exhibited lower WSS on the sinus wall, likely due to less vigorous leaflet motion and reduced flow within the sinus. In contrast, the FV and CFV cases showed higher WSS values influenced by dynamic leaflet movements and increased flow velocities. Understanding WSS patterns is essential, as regions of low shear stress are associated with endothelial dysfunction and thrombosis.

Overall, the findings underscore the significant role of vessel diameter and leaflet scaling in venous valve function. Larger veins with fully buckling leaflets not only facilitate more efficient blood flow but also exhibit dynamic flow patterns that may influence vascular health. These insights are vital for advancing the understanding of venous hemodynamics and could inform the design of therapeutic interventions for venous disorders. The case presented in the next section explores the effects of varying inflow conditions, such as those induced by the calf muscle pump, on valve dynamics and sinus residence times.

4.2 Calf muscle pump: towards sinus drainage?

4.2.1 Typical inflow in calf muscle pump configuration

The primary aim of this study is to assess valve dynamics within the context of calf muscle contraction. Specifically, this study aims to replicate the contraction flow observed via echo-Doppler measurements performed at CHU Nîmes. A particular focus is placed on flow enhancement and its influence on drainage in the sinus region. The case under consideration is a femoral valve, with geometry identical to that described in Section 3.3. The diameter of the valve is set to 10 mm, and the leaflet thickness is uniformly 70 µm. The sinus length is one diameter, and the sinus depth is 1.2 times the radius.

The physical parameters used in the simulation include a fluid and solid density of 1050 kg/m^3 and a fluid dynamic viscosity of 3.3×10^{-3} Pa.s. The solid is modeled as a neo-Hookean material with a Young's modulus of 1×10^5 Pa and a Poisson's ratio of 0.45. The inflow profile has a period of 1.2 s and follows a radial parabolic profile, peaking at 0.4 m/s. The time-dependent profile is described by Equation (4.2) in the same fashion as the breathing cycle mimicking profile (Equation (4.1)). This profile is compared with the previously established profile, as illustrated in Figure 4.9a. The corresponding Reynolds number is 600, which is twice that of the FV case.

$$v(t) = \begin{cases} v_{\max}\left(1 - \cos^2(\pi t)\right) & \text{for } t < 1 \text{ s}, \\ 0 & \text{for } t \geq 1 \text{ s}. \end{cases} \tag{4.2}$$

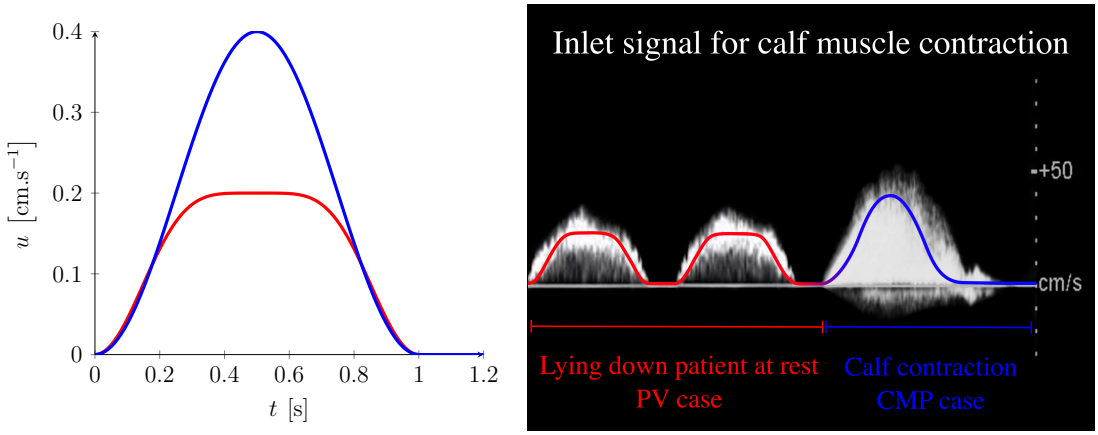

(a) (b)

Figure 4.9: (a) Comparison of the inflow velocity profiles for the calf muscle pump (blue) and the resting inflow (red). (b) Qualitative comparison of the inflow velocity profile of the contraction simulation. The first two cycles are taken from the FV case presented in Section 3.3, and the third utilizes the calf muscle contraction inflow.

4.2.2 Computational set-up

With the goal of replicating calf muscle contractions, the computational setup has been adapted from the FV case described in Section 4.1. This ensures that the dynamics of the calf muscle pump can be compared directly with the resting configuration. The numerical and mesh parameters are identical to those used in the FV case and can be found in Table 4.2.

The initial solution for this calf muscle pump (FV-CMP) case is taken from the FV case at the end of cycle two. The contraction phase corresponds to the third cycle and is compared with the third cycle of the FV case, which serves as the reference. The computational time for 1.2 s of physical time is the same as for the CFV case presented in Section 4.1.2.

4.2.3 General valve dynamics

The leaflet dynamics observed for the FV-CMP are quite similar to those of the FV case, with complete buckling observed, reaching phase III (see Section 3.2). The resulting EOA and associated variation are plotted in Figure 4.10. The maximum effective orifice area (EOA) recorded for the FV-CMP case is 52%, observed at 0.5 s, which is 10% higher than the reference case. The opening time to reach the maximum EOA is 0.45 s, which is faster than the closing time (0.6 s). However, at the outset of the opening and the end of the closing phase, the EOA for each case follows a similar trend. The gain in opening area is mainly due to the higher inlet Reynolds number in the FV-CMP case than the FV case.

The closing is slower than the opening, but not as much as observed in the CFV case, where the leaflets were significantly slowed down by added-mass effect. Having established the differences in leaflet dynamics, we now turn to how these movements influence blood flow patterns and velocity fields in the sinus region.

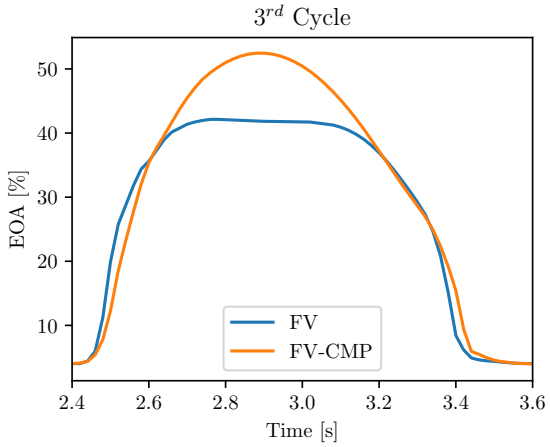

Figure 4.10: Effective Opening Area (EOA) for the reference case FV and the FV-CMP case.

4.2.4 Velocity fields

The pressure loss through the valve is represented in Figure 4.11 (left and center graphs), for the FV-CMP and FV cases. The maximum absolute pressure loss is obtained as expected for the FV-CMP; however, the FV-CMP case is more efficient in utilizing the available pressure from the incoming blood flow, which is consistent with the findings presented in Section 3.3.2. The blood flow develops to a maximum velocity of 47 cm.s^{-1}, observed at the centerline downstream of the sinus. The axial velocity at the center of the valve, three diameters in the proximal direction, is plotted in Figure 4.11. More instabilities are observed in the FV-CMP, which is consistent with the higher inlet Reynolds number. Vortex shedding is also observed in the FV-CMP case, and the associated Strouhal number is 0.88, which is lower than that of the FV case. The vortices detach in the same manner as in the FV case, behind the leaflets' commissures, and are oriented in the normal direction of the frontal plane.

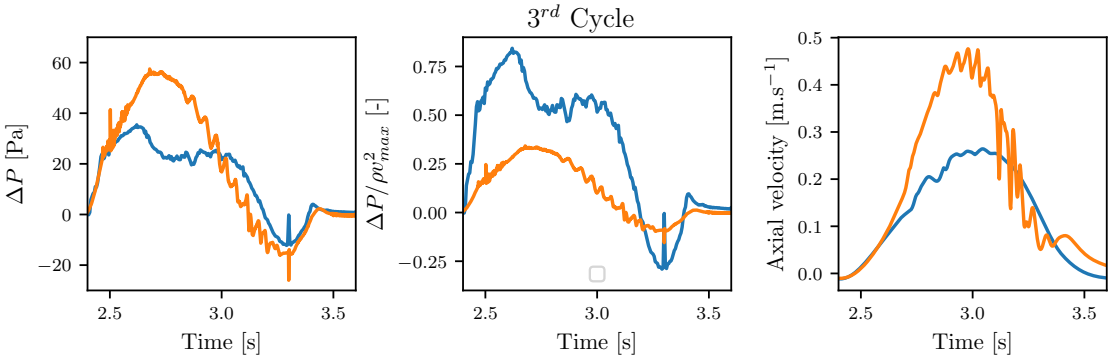

Figure 4.11: Left: Pressure loss across the valve during the third cycle for the FV-CMP and FV cases. The pressure loss is the difference between the pressure at the center one diameter upstream and three diameters downstream of the valve. Center: Pressure loss scaled by the maximum dynamic pressure applied on the inlet boundary. Right: Axial velocity at the center of the valve, three diameters in the proximal direction, for the FV-CMP and FV cases.

To analyze the flow inside the valvular sacs, massless tracers were also seeded within the sinus. The results are plotted in Figure 4.12. The pathlines in the FV-CMP and FV cases reveal similar vortex structures. In both cases, a vortex ring forms behind the leaflets' tips, with particles following distinct paths depending on their initial position in the sinus. The particles injected close to the midpoint of the tip come back into the sinus close to the wall, and the particles injected near the valve commissures travel back into the wake of their respective valve commissure. Significantly more particle movement in the sinus is recorded during the closing phase in the FV-CMP configuration. The buffer region, discussed in Section 3.3.4, goes deeper in the sacs in the FV-CMP. This suggests that the FV-CMP is more efficient at moving and mixing the blood within the sinus than the bed-resting configuration. In both cases, the particles located near the bottom of the sacs, even if they move during the cycle, remain close to their initial positions.

4.2.5 Towards a reduced residence time

An important indicator of sinus drainage is the time red blood cells (RBCs) and platelets spend inside the sinus, i.e., the residence time. An estimation of the residence time was initially developed for arteries [219], which involves the oscillatory shear rate and the shear stress acting on the arterial wall, τ_w. Estimating the wall shear stress requires having a fully resolved boundary layer, which can be numeri-

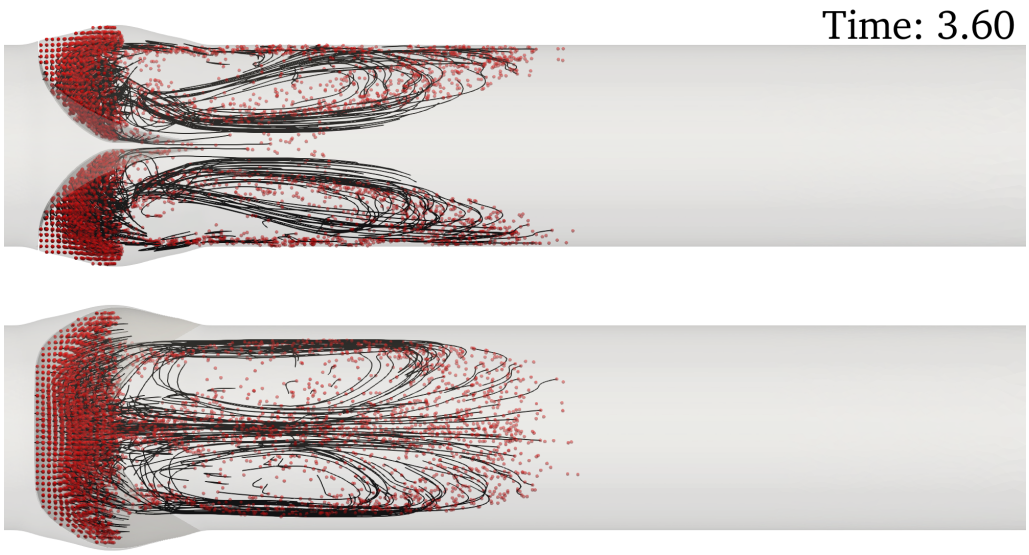

(a)

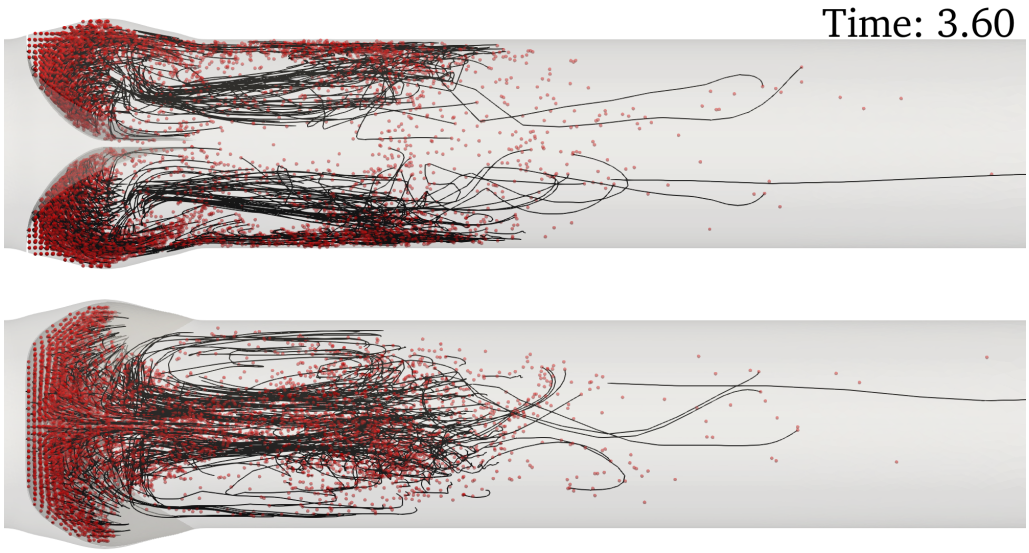

(b)

Figure 4.12: Pathlines of particles seeded at time $t = 2.40$ s for the reference FV case (a) and the FV-CMP case (b). The particles are massless tracers seeded uniformly in the sinus at the outset of the third cycle.

cally very costly. To overcome this limitation, the residence time can be estimated using tracers, i.e., massless particles seeded in the sinus and advected by the fluid. The percentage of particles still present at the end of the cycle gives a close estimation of the volume remaining after each cycle. The resulting graph is presented in Figure 4.13. As expected, the volume-to-drain curves differ for the third cycle. An estimation of the residence time was calculated using a geometric sequence based on the percentage of particles remaining in the sinus after each cycle (see Section 3.3.5). The associated geometric sequence has the following parameters: first term 0.595 and ratio 0.799 for the FV-CMP case, and 0.595 and 0.885 for the FV case. The residence time of 1% of the fluid initially present in the sinus is 25 s for the FV-CMP case, compared to 43 s for the FV case. The time required to flush the majority of the sinus is much lower in the FV-CMP configuration. Accordingly, the calf muscle contraction is more efficient at flushing the sinus than the bed-resting configuration.

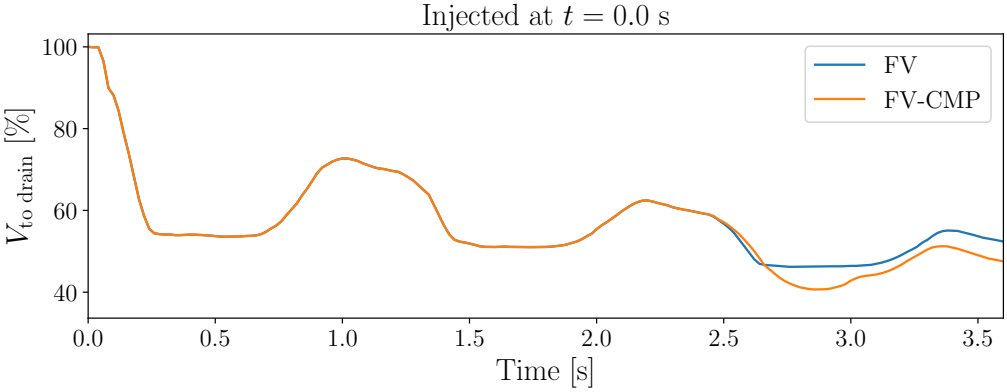

Figure 4.13: Percentage of the volume to drain. The particles are seeded at time $t = 0.0$ s, i.e., at the beginning of the FV case simulation.

4.2.6 Discussion

This study investigated the hemodynamics of venous valves under the influence of the calf muscle pump (FV-CMP), aiming to understand how enhanced inflow due to muscle contraction affects valve dynamics and sinus drainage. By replicating the contraction flow observed via echo-Doppler measurements, the FV-CMP configuration was compared to a resting femoral vein (FV) case to assess the impact on various hemodynamic parameters.

The FV-CMP case exhibited similar leaflet behavior to the FV case, with complete buckling reaching phase III. However, the FV-CMP valve achieved a higher maximum effective orifice area (EOA) of 52%, a 10% increase over the FV case. This enhanced opening is primarily attributed to the higher inlet Reynolds number, which exerts greater dynamic pressure on the leaflets. The valve in the FV-CMP case opened more rapidly, reaching maximum EOA in 0.45 s, and closed more slowly (0.6 s).

The flow downstream of the FV-CMP valve led to vortex shedding, characterized by a Strouhal number of 0.88, which is lower than that of the FV case. The vortices detached from the leaflets' commissures, maintaining a similar detachment mechanism as in the FV case but potentially with a higher intensity due to the higher flow velocity. The pathlines of massless tracers seeded in the sinus demonstrated that the FV-CMP facilitated greater particle movement. This indicates improved mixing and reduced areas of stagnation within the sinus, which are critical for preventing thrombus formation. Additionally, a substantial reduction of the residence time underscores the effectiveness of the FV-CMP in promoting sinus drainage. The geometric sequences used to model the drainage process highlighted a lower ratio in the FV-CMP case (0.799) versus the FV case (0.885), indicating a faster decay of residual volume over successive cycles.

Overall, our findings suggest that the FV-CMP enhances valve performance by increasing the EOA, promoting faster valve opening, and facilitating sinus drainage through enhanced flow dynamics. The increased flow velocity and associated instabilities contribute to improved mixing within the sinus, potentially reducing the risk of thrombus formation due to prolonged blood stasis. However, despite these improvements, particles near the bottom of the sacs remained close to their initial positions in both configurations, indicating that certain regions may still be susceptible to stagnation.

Several important considerations emerge from this study. First, the influence of geometry on valve performance necessitates further investigation. While a consistent geometry is maintained to isolate the effect of inflow velocity, variations in sinus depth, leaflet curvature, and valve placement could further optimize sinus drainage. For instance, modifying the sinus or leaflet shape might enhance flow recirculation patterns, improving the clearance of stagnant blood near the sac bottoms. Second, the downstream effects of the observed vortex shedding on subsequent valves are not fully understood. The vortices generated in the FV-CMP case could impact the hemodynamics of downstream valves, potentially influencing their performance and the overall efficiency of venous return. Understanding these interactions is crucial, especially in veins where valves are closely spaced. The case presented in the next section will address these issues.

4.3 Dynamics of consecutive valves

This study aims to achieve two objectives. First, the interaction of two valves in series and the associated hemodynamic markers are presented. The differences in flow features and residence time in the sinus region are of particular interest. The first and second valves will be referred to as V1 and V2, respectively. However, a new geometry is used for V1 and V2; thus, a comparison with the reference CFV case is made with V1 to assess the efficiency of the new geometry.

4.3.1 A relaxed insertion angle

The case presented here is a common femoral vein (CFV) with a 14 mm diameter containing two consecutive valves. The CFV case presented in Section 4.1 is taken as a reference. The original geometry had a 90° angle at the agger, which likely counteracts the flow development and may provoke blockage. This can also be a source of instability development. To mitigate this issue, the angle at the agger has been relaxed by 10.2°, as illustrated in Figure 4.14. The midpoint of the leaflets' tip has been lowered in the distal direction, as well as the valve's commissures. The first modification provides more surface reserve, and the second prevents the leaflets from staying too close to one another near the commissures. The sinus dimensions are the same as those described in Section 4.1.1. The leaflet thickness is set at 100 µm. The inflow waveform and flow rate are also consistent with the previous case.

The physical parameters used in the simulation are similar to the CFV case (see Table 4.2). The time profile is the one described in Equation (4.1).

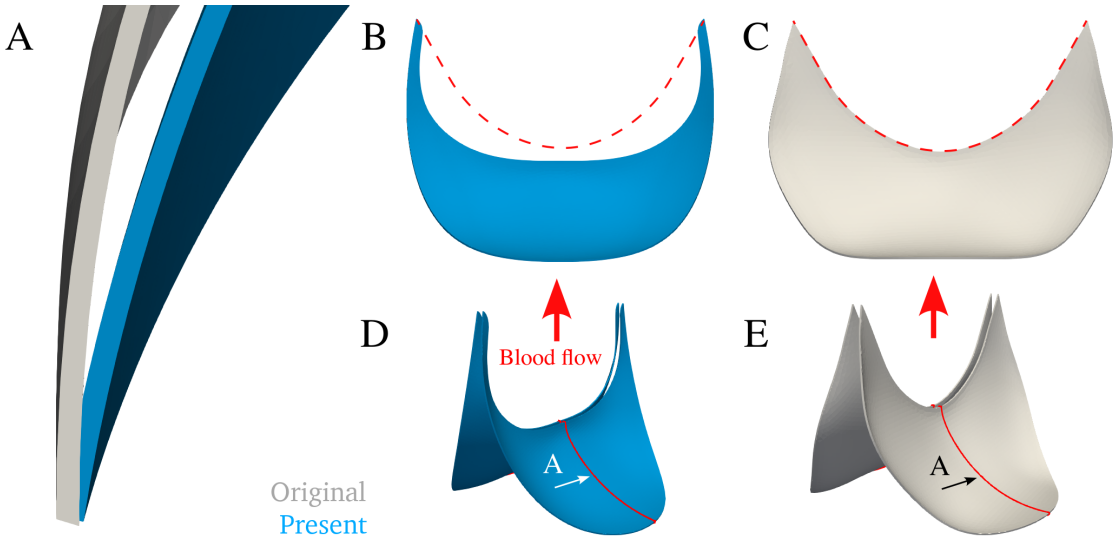

Figure 4.14: Comparison of the modified (blue) and reference (gray) geometry. (A) focus on the angle relaxation at the bottom of the valve. (B; C) comparison views from the sinus. The original tip shape from (C) is reported in (B) to exhibit the modifications (lowered mid-point tip and relaxed insertion angle). (D; E) view from 3 quarter. The natural direction of blood flow is indicated with the red arrow to help visualization.

4.3.2 Numerical parameters

Apart from the mesh that has to be generated onto the new geometry, the rest of the computational setup remains consistent with that used in the CFV case (see Table 4.2). The mesh parameters are as follows: the size is 140 µm in a 5-element layer near the leaflets, 210 µm at the wall, and 280 µm in the rest of the domain. For the pseudo-solid parameters, $R_{min,PS}$ and $R_{max,PS}$ are set to 420 µm and 2.1 mm, respectively.

In this configuration, the computational time for 1.2 s of physical duration increases to 96 h on 384 cores of the ADASTRA HPC cluster of GENCI/CINES (compared to 36 h on 192 cores for the CFV case). The partitioning is the same as presented in Section 4.1.2, with a slightly higher cost due to mesh movement (35%).

4.3.3 Hemodynamics in a series of valves

The resulting hemodynamic patterns followed by the particles seeded in the sinus (at the outset of the third cycle) are illustrated in Figure 4.15. In the snapshots taken at maximum inlet velocity, the particles display two distinct movement patterns:

- **CFV case:** Only the particles close to the outlet plane of the sacs are advected towards the sagittal plane to leave the sinus near the midpoint of the leaflet tip. These particles enter back into the sinus either close to the sinus wall centerline or near the valve commissure. This pattern takes time to develop and reaches its full extent at the end of the cycle.

- **V1 case:** The particles are advected away from the sagittal plane towards the valve commissures, unveiling two symmetrical recirculations within the sinus. Comparing Figure 4.15a and Figure 4.15b, the flow structures develop faster in the V1 case.

In addition, significantly more movement, especially at the bottom of the sacs, is observed in the V1 case (Figure 4.15d).

The valves' EOA dynamics are depicted in Figure 4.18a. While a maximum EOA of 42% is observed for the CFV, V1, and V2 valves, the dynamics of the valves in series differ from the CFV case. The V1 and V2 valves open and close quicker than the CFV valve, with the V2 valve closing slightly faster than V1. The opening remains quicker than the closing for the valves in series. Some oscillations appear on the V2 valve plateau, which are due to the flow perturbed by the V1 valve. To support these observations, the dynamics of the V1 and CFV valves are compared in Figure 4.16. The snapshots show that the V1 valve opens more close to the valve commissures than the CFV valve (Figure 4.16c and Figure 4.16d). The V1 valve also closes faster than the CFV valve (Figure 4.16e). The V2 valve is not presented here, but the dynamics are similar to the V1 valve.

The velocity fields and the Q-criterion for the valves in series are displayed in Figure 4.17, exhibiting vortex shedding only downstream of V2. More precisely, V2 vortex shedding initiates once the perturbed flow from V1 reaches V2. The axial velocity taken at the center of the valve 3 diameter downstream of the valve, plotted

in Figure 4.18b, witnesses the perturbations of the flow in the wake of the V2 valve by the presence of the V1 valve. The corresponding Strouhal is 1.56 for this vortex shedding, which is of the same order as the PV and CFV case.

The pressure loss through the different valves is plotted in Figure 4.18b. The dynamics of the pressure loss through each valve in series is similar to the CFV one. The peak pressure loss is the same for the valves in series, reaching 36 Pa at 2.6 seconds (0.2 s after the outset of the third cycle), which is lower than the CFV case. After peak inlet velocity is reached (2.9 s), the pressure loss stabilizes for all valves at 15 Pa for the V2 and CFV valves against 25 Pa for the V1 valve. The minimum reverse pressure loss equals -25 Pa for the V2 and CFV valve and -12 Pa for the V1. The opening of the CFV geometry is more costly than the new geometry while maintaining the opened position seems to be more costly for the V1 valve compared to V2 and CFV. The higher reverse pressure loss would markedly help the faster closing of the V2 valve compared to the V1 valve.

Regarding the 90° orientation of the blood flow after the second valve, it is not as clear as in the reference case. In the frontal plane, the mixing layers behind the wake of each valve commissure develop towards the center of the vein. However, in the sagittal plane, no noticeable extension of the flow sheet towards the vein wall is detected. From what was observed in the previous paragraph, 90° orientation of the blood flow after the first valve is not necessary to reduce the pressure loss through the second valve.

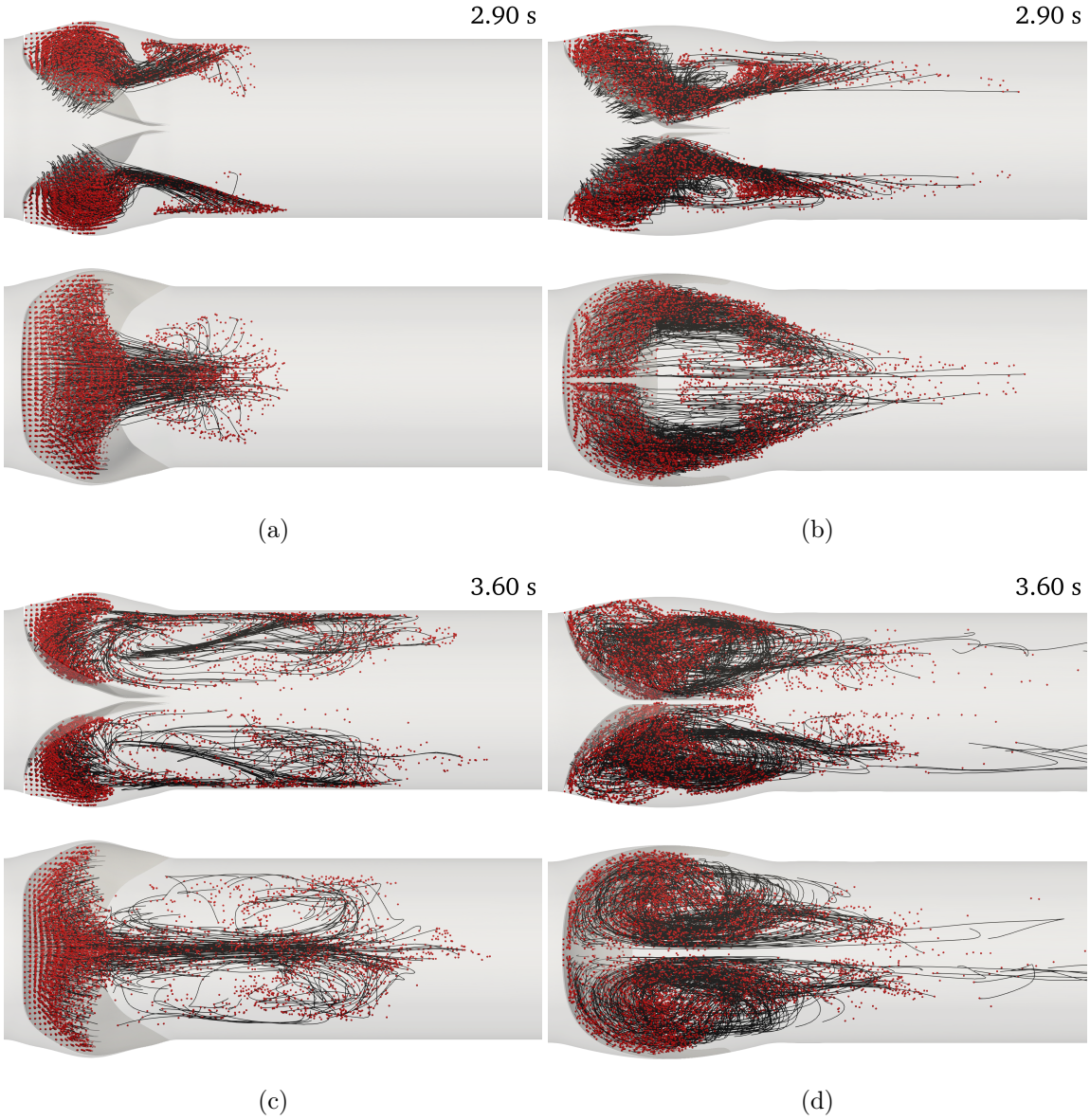

Figure 4.15: Pathlines of particles seeded at the outset of the third cycle for the CFV (a, c) case and V1 (b, d). (a) and (b) are at time $t = 2.90$ s, i.e., at maximum inlet velocity. (c) and (d) are at time $t = 3.60$ s, the outset of the third cycle.

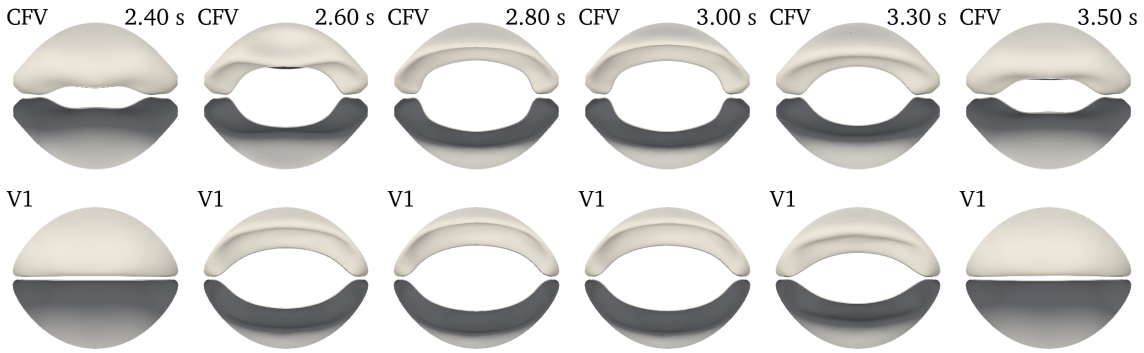

Figure 4.16: Snapshots of the V1 valve compared to the CFV valve at different times.

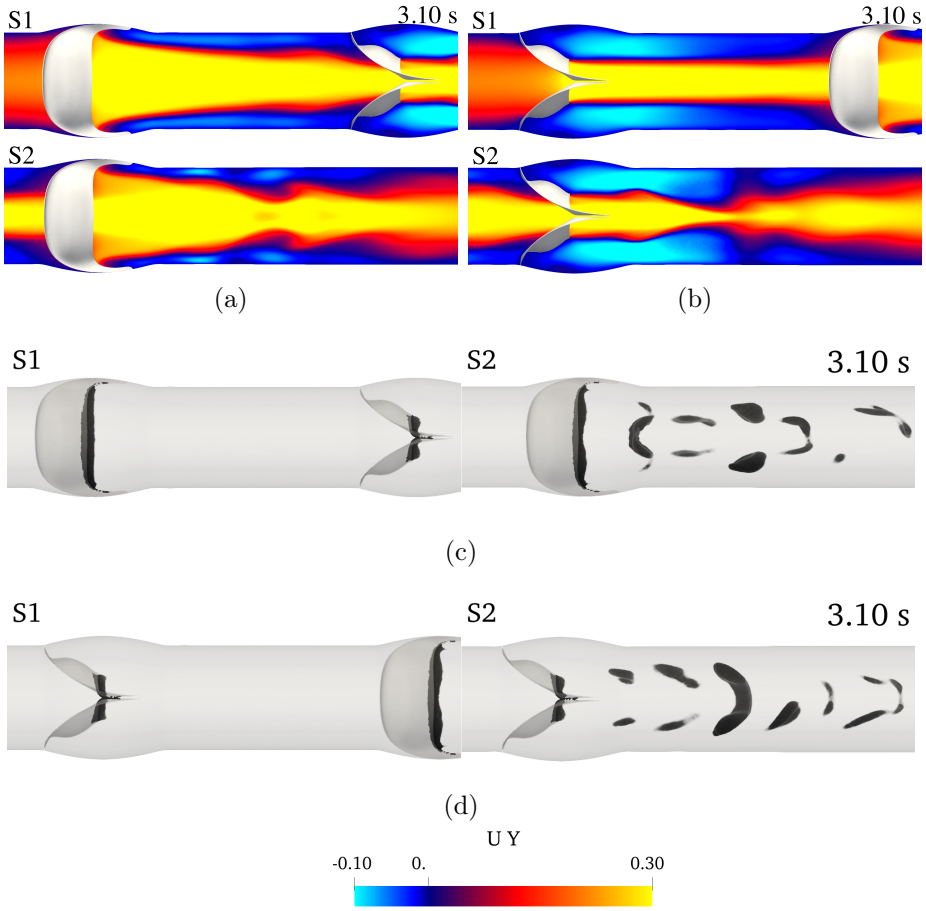

Figure 4.17: Snapshot of the velocity field of each valve in the frontal (a) and the sagittal plane (b) and the Q-criterion (bottom) in the frontal (c) and sagittal (b) planes at $t = 3.10$ s.

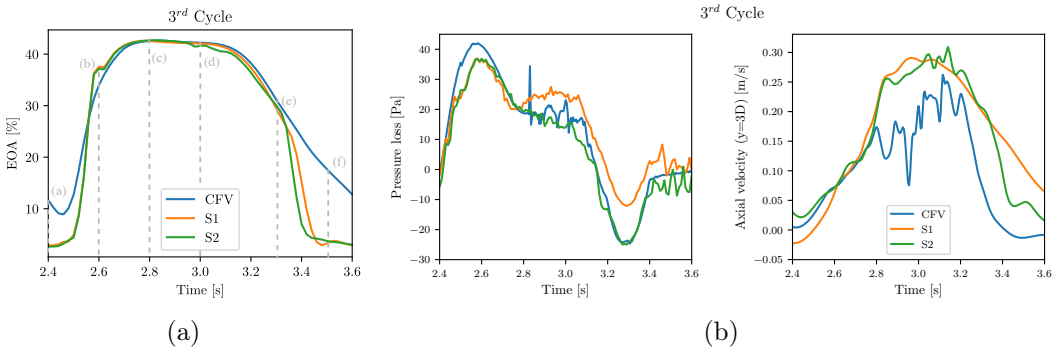

Figure 4.18: (a) Plot of the effective opening area (EOA) for the CFV case, V1, and V2 valves. (b) Left: pressure loss across the valve of the third cycle for the V1, V2 and CFV valves. The pressure loss is the difference between the pressure at the center one diameter upstream and 3 diameter downstream of the valve. Right: axial velocity at the center of the valve 3 diameter in the proximal direction for the V1, V2 and CFV valves.

4.3.4 Effect on the residence time

The residence time was calculated using a geometric sequence based on the percentage of particles remaining in the sinus after each cycle. This method provides a reliable estimate of the duration of blood residence in the sinus region, thus facilitating the assessment of the efficacy of drainage in different configurations. To this effect, the massless particles are seeded uniformly within the sinus at time $t = 0$ s. The temporal variation of the percentage of blood initially present in the sinus that remains to be drained is plotted in Figure 4.19. A significant difference is observed from the next cycle after the injection of particles: only 27% and 23% remain for V1 and V2, respectively, compared to 69% for the reference case. From this point of view, the new geometry has more than twice the drainage efficiency of the reference one in one cycle. The residence times obtained are 11, 9, and 31 seconds for the V1, V2, and CFV valves, respectively. The blood initially present within the sinus of the CFV case remains three times longer than in the new geometry. Moreover, the residence time is reduced in the V2 valve compared to the V1 valve. This suggests that the blood is more efficiently drained in the second valve than in the first one.

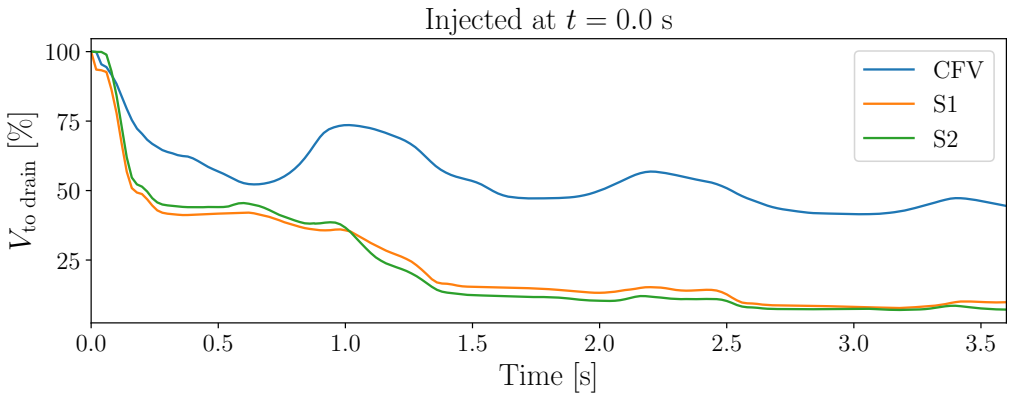

Figure 4.19: Plot of the percentage of the volume to drain with regard to time. The particles are seeded at time $t = 0.0$ s.

4.3.5 Discussion

The present study investigates the impact of a relaxed insertion angle on the hemodynamics of consecutive venous valves, comparing a new geometric configuration to a reference case. By relaxing the angle at the agger by 10.2° and adjusting the positions of the leaflets' tips and commissures, the modified geometry aims to enhance flow development and mitigate potential blockages and instabilities observed in the original design.

This analysis reveals that these geometric modifications significantly improve the hemodynamic performance of the valves. In Section 4.3.3, the particles within the sinus of the first valve (V1) exhibit more pronounced and faster-developing flow structures compared to the CFV reference case. This enhanced movement, especially

at the bottom of the sacs (Figure 4.15d), suggests improved mixing and potential reduction in areas of stagnation, which are critical factors in thrombosis prevention.

The analysis of the Figure 4.18a indicates that both V1 and V2 valves open and close more rapidly than the CFV valve. The quicker valve dynamics, with the V2 valve closing slightly faster than V1, may contribute to more efficient blood flow and reduced residence times. The observed oscillations on the V2 valve plateau are attributed to flow perturbations from the upstream V1 valve, highlighting the complex interactions in valves arranged in series.

Vortex shedding was observed only downstream of V2, initiated by the perturbed flow from V1. This finding underscores the influence of upstream valve dynamics on downstream flow patterns. The absence of a clear 90° orientation of blood flow after the second valve, as opposed to the reference case, suggests that the modified geometry alters differently the development of mixing layers, particularly in the sagittal plane.

The most significant improvement is noted in the Residence Time within the sinus region (Section 4.3.4). The new geometry demonstrates more than twice the drainage efficiency of the reference case within one cycle. The residence times for V1 and V2 are substantially reduced to 11 and 9 seconds, respectively, compared to 31 seconds for the CFV valve. This reduction indicates that blood is more efficiently drained in the modified geometry, particularly in the second valve, which is crucial for minimizing the risk of thrombosis associated with prolonged blood stasis.

Along with the enhanced flow dynamics and reduced residence times, the peak pressure loss across the valves is lower in the new geometry compared to the reference case. This observation confirms the improved efficiency of the modified design while maintaining a physiological pressure gradient to ensure proper blood circulation.

In summary, the modifications introduced in the valve geometry—namely, the relaxed insertion angle and adjusted leaflet positions—have led to significant improvements in hemodynamic performance. The enhanced flow structures, quicker valve dynamics, and reduced residence times contribute to more efficient blood flow and potentially lower the risk of thrombotic events. These findings highlight the importance of geometric considerations in the onset of deep vein thrombosis.

Chapter5

Discussion

5.1 Conclusion

In light of the significant global burden of venous thromboembolism (VTE), there is a pressing need for the qualitative and quantitative assessment of venous valve function. Given that the majority of VTE cases are hospital-acquired, it is imperative to gain a deeper understanding of the biomechanical behaviour of the venous valve in order to enhance the diagnosis and treatment of VTE. Cardiovascular valves are coupled physical systems comprising biological tissues that interact with blood flow, either mechanically or chemically. Thrombus formation is frequently observed in the valves of the deep venous system of the lower extremity. The endothelium is responsible for preventing blood clotting; however, prolonged bed rest can disrupt its functions. It is established that the anticoagulant phenotypes of endothelial cells (ECs) are sensitive to the mechanical forces to which they are subjected.

The development of in silico models of venous valves represents a promising avenue for investigating the interaction of endothelial cells (ECs) with blood flow. FSI methods are inherently well-suited to simulating the interaction between blood flow and the venous valve. However, to gain insight into relevant haemodynamic markers such as wall shear stress (WSS), flow patterns, or pressure distribution within the valve, it is essential to select an appropriate FSI method. These methods have been employed in a diverse array of applications, spanning from heart valves to red blood cell transport. They have demonstrated their capacity to offer insights into the biomechanical behaviour of the venous valve and its interaction with blood flow.

In silico models of venous valves have been developed, which propose the deformation of valve geometries under strain. This assumption facilitates the design of the leaflets, yet it does not replicate the intricate behaviour of the valve under physiological conditions. Either the pressure required to open the valve is considerable, as evidenced by Buxton and Clarke [76], or the stiffness must be reduced under physiological conditions. As demonstrated by Hofferberth et al. [28], in vivo venous valves, when cut open and unfolded, display complete unfolding of the leaflets onto the vein wall, indicating an excess of surface area. To the best of the author's knowledge, no in silico model has been developed to investigate surface reserve.

The objective of the present study was to develop an in silico model of a venous

valve to assess the biomechanical behaviour of a valve with surface reserve. It forms part of the DY-MTEV project, which aims to provide new insights into venous thromboembolism with a particular focus on endothelial cells (ECs). The project is divided into three work packages: the medical imaging of valve dynamics and blood flow at the CHU of Nîmes; the in vitro experiments on ECs at the CBS; and the in silico valve model at IMAG (Chapter 1).

The FSI solver, developed by Fabbri et al. [110], serves as the foundation for the methodology employed throughout this thesis. A neo-Hookean material type was incorporated into the structural solver to address the shortcomings of the existing Saint-Venant-Kirchhoff approach. The originally designed constant under-relaxation technique was then enhanced through the incorporation of the Aitken dynamic relaxation method. Furthermore, a contact penalty algorithm was introduced to prevent the leaflets from interpenetrating. All methods have been validated on extensively studied benchmarks, and the results are in good agreement with the existing literature (Chapter 2).

The newly validated methods were subsequently applied to the novel valve geometry design, which was created based on a comprehensive literature review. A structural analysis was conducted to evaluate the various configurations and deformations inherent to the design. The results demonstrate that the valve is capable of opening under physiological conditions. Subsequently, the initial FSI simulation of the valve with surface reserve was conducted. The typical flow characteristics of the venous valve were observed, including the formation of recirculations in the wake of the valve commissures and leaflets, which resulted in a significant reorientation of the flow further downstream. The pressure gradient required to open the valve under supine flow conditions is sufficiently low to ensure adequate venous return from the foot to the heart. In addition, a novel methodology for estimation of the residence time has been put forth, establishing that 1% of the blood initially present within the sinus resides for 68 s (Chapter 3).

Subsequently, the valve model was employed to examine haemodynamic modifications along the lower limb deep vein system. Three cases were constructed with the objective of reproducing the flow conditions in a popliteal, femoral and common femoral vein valve. The inflow parameters were modified to align with the specific location of each valve, resulting in a range of Reynolds numbers from 150 to 420. The observed dynamics of the leaflets were specific to each case. The flow patterns immediately downstream of the valve were found to be comparable for each case, with the formation of a vortex ring at the tip of the leaflets. However, downstream, different flow patterns were observed, ranging from highly stable and developed steady flow to transient flow with complex vortex structures (from low to high Reynolds). The wall shear stress distribution on the sinus wall demonstrated varying dynamics during the opening and closing phases, but was comparable once the flow was established. Higher values were observed in the femoral and common femoral vein valve configurations (Chapter 4.1).

The impact of a calf muscle pump was examined by modifying the inflow parameters of the femoral valve configuration. The valve was subjected to a sinusoidal inflow condition, with a maximum velocity that was twice that observed in the

supine inflow. As might be expected, the observed EOA is higher than that observed in the supine inflow condition. Given that the Reynolds number is twice that of the reference case, the flow pattern is analogous to that observed in the common femoral vein valve configuration. Concerning residence time, it is evident that the residence time is inherently shorter in the calf muscle pump condition (Chapter 4.2).

Finally, the question of the effect of geometry on valve haemodynamics was addressed, along with the haemodynamics in a paired valve system. A new design, based on the dimensions of the common femoral vein, was proposed as a means of overcoming the limitations of the original design. The valve was subjected to the same inflow conditions as those experienced by the common femoral vein valve configuration. The dynamics of the leaflets are comparable to those observed in the configuration of the common femoral vein. A novel recirculation pattern was observed in the sinus. No vortex ring is formed at the tip of the leaflets; rather, the blood enters the sinus through the centre. This movement is further enhanced during the closing phase, resulting in significantly more efficient sinus emptying. The residence time has been reduced by a factor of three in comparison to the original common femoral vein valve configuration (see Chapter 4.3).

The development of a biomechanically oriented fluid-structure interaction solver and its application in the context of venous valve dynamics has been a fruitful endeavour. Despite the inherent limitations of the model, the results enlight the dependence of sinus drainage to geometric consideration, offering new insights into the onset of thrombotic events.

5.2 Perspectives

The utilisation of a flexible wall for the vein may prove an effective strategy for achieving the physiological conditions of a venous valve. In particular, at the valve agger, a deformable vein wall may facilitate the deformation of the leaflets in close proximity to the wall. In the context of the calf muscle pump, the vein wall could be made to move in order to reproduce the effect of muscle contraction.

In the context of systems comprising serial venous valves, the application of periodic conditions may prove beneficial. The use of periodic conditions has the potential to reduce the computational cost by acting on several levers. The first step is to reduce the computational domain, which will result in a smaller number of elements in the mesh. This will facilitate the mesh movement procedure. The exclusion of a second valve would also be advantageous for the structural solver. The physical time required to reach a fully developed flow and flush out the initial conditions would also be reduced.

The venous valve geometry remains very simplified compared to a patient-specific geometry. Reproducing the valve geometry from medical imaging would be a good step towards a more realistic model. The valve geometry could be extracted from medical imaging and the leaflets segmented to create a 3D model. The valve could then be subjected to the same inflow conditions as used in this work. The results could be compared to assess the relevance of the model.

In addition to patient geometry, further study of venous valves in the vicinity of

bifurcations may prove beneficial. For instance, a broad range of sapheno-femoral junction configurations can be observed in patients. It would be beneficial to assess the impact of branching on valve functionality in order to gain insight into the initiation of thrombus formation within the valve bags. Certain patterns may be more susceptible to thrombus formation, and this should be taken into account.

As previously stated in the FEM method presentation, this work has employed four-node tetrahedral elements (linear), despite the availability of 10-node tetrahedral elements (quadratic). The project commenced with the use of these elements, but they were subsequently discarded. The results they produced were not in line with expectations and introduced instability issues in FSI simulations. Zhang et al. [149] argued that the original formulation of the shape functions for those elements is not well suited to non-linear solid mechanics. Such an approach may result in a non-SPD mass matrix, which could potentially lead to the preconditioned gradient linear solver crashing. They have put forward a revised formulation of the shape functions to address this issue. The use of 10-node tetrahedral elements would enable us to refine the mesh and enhance the precision of the results. Similarly, the use of shell elements for the valve leaflets would be beneficial. The leaflets are thin structures, so using shell elements would enable us to reduce the number of elements without compromising accuracy.

As outlined in the computational setup sections, the computational resources required to run the simulations can be significant. The majority of the expenditure is attributed to the structural linear solver. Improved preconditioning is the most effective way to reduce the time spent on the structural linear solver. There are a number of options to consider, including the use of the PETSC library [220–222]. It would be beneficial to devote particular attention to the monolithic FSI literature. As the matrix of the linear solver obtained in the monolithic formulation is highly non-SPD, they have developed robust preconditioning methods, including multigrid and algebraic approaches.

It should be noted that, despite not being discussed in this work, the FSI method is still highly susceptible to pressure spikes caused by the interpolation of velocity made after dynamic mesh adaptation. This is in line with the findings presented in [120]. The Aitken dynamic relaxation method has enhanced the stability of the system, but the stability limit remains very close. Furthermore, this issue is compounded in the cases treated here, due to the necessity for intensive remeshing when the valve is in proximity to the closed position. One potential solution to this issue is to utilise alternative boundary conditions at the interface, which could help to mitigate the pressure peaks. The Robin conditions are a combined Dirichlet and Neumann condition designed to handle FSI cases with a significant added-mass effect. By subtracting part of the fluid traction from the right-hand side of the structural linear system and adding it to the mass matrix, we can stabilise the coupling. Another potential solution is the use of pseudo-compressibility. Pseudo-compressibility is a method used to stabilise the pressure field in incompressible flow. This approach introduces a compressibility term into the continuity equation. Further work could concentrate on utilising pseudo-compressibility to stabilise the FSI coupling in the iterations following a remeshing process.

Bibliography

[1] Roth Gregory A. et al. "Global Burden of Cardiovascular Diseases and Risk Factors, 1990–2019". In: *Journal of the American College of Cardiology* 76.25 (Dec. 22, 2020). Publisher: American College of Cardiology Foundation, pp. 2982–3021. DOI: 10.1016/j.jacc.2020.11.010 (cit. on p. 1).

[2] G. A. Mensah, G. A. Roth, and V. Fuster. "The Global Burden of Cardiovascular Diseases and Risk Factors". In: *Journal of the American College of Cardiology* 74.20 (Nov. 2019), pp. 2529–2532. DOI: 10.1016/j.jacc.2019.10.009 (cit. on p. 1).

[3] A. M. Wendelboe and G. E. Raskob. "Global Burden of Thrombosis: Epidemiologic Aspects". In: *Circulation Research* 118.9 (Apr. 29, 2016), pp. 1340–1347. DOI: 10.1161/CIRCRESAHA.115.306841 (cit. on p. 1).

[4] A. Cohen et al. "Venous thromboembolism (VTE) in Europe: The number of VTE events and associated morbidity and mortality". In: *Thrombosis and Haemostasis* 98.10 (2007), pp. 756–764. DOI: 10.1160/TH07-03-0212 (cit. on p. 2).

[5] S. D. Grosse et al. "The economic burden of incident venous thromboembolism in the United States: A review of estimated attributable healthcare costs". In: *Thrombosis Research* 137 (Jan. 2016), pp. 3–10. DOI: 10.1016/j.thromres.2015.11.033 (cit. on p. 2).

[6] S. W. Narayan et al. "Preventability of venous thromboembolism in hospitalised patients". In: *Internal Medicine Journal* 53.4 (Apr. 2023), pp. 577–583. DOI: 10.1111/imj.15600 (cit. on p. 2).

[7] C. T. Esmon. "The Roles of Protein C and Thrombomodulin in the Regulation of Blood Coagulation". In: *Journal of Biological Chemistry* 264.9 (Mar. 1989), pp. 4743–4746. DOI: 10.1016/S0021-9258(18)83649-3 (cit. on p. 2).

[8] E. M. Conway. "Thrombomodulin and its role in inflammation". In: *Seminars in Immunopathology* 34.1 (Jan. 2012), pp. 107–125. DOI: 10.1007/s00281-011-0282-8 (cit. on p. 2).

[9] J. E. Sadler. "BIOCHEMISTRY AND GENETICS OF VON WILLEBRAND FACTOR". In: *Annual Review of Biochemistry* 67.1 (June 1998), pp. 395–424. DOI: 10.1146/annurev.biochem.67.1.395 (cit. on p. 2).

[10] C. V. Denis and P. J. Lenting. "von Willebrand factor: at the crossroads of bleeding and thrombosis". In: *International Journal of Hematology* 95.4 (Apr. 2012), pp. 353–361. DOI: 10.1007/s12185-012-1041-x (cit. on p. 2).

[11] S. Sevitt. "The structure and growth of valve-pocket thrombi in femoral veins". In: *Journal of Clinical Pathology* 27.7 (July 1, 1974), pp. 517–528. DOI: 10.1136/jcp.27.7.517 (cit. on p. 3).

[12] E. G. Brooks et al. "Valves of the deep venous system: an overlooked risk factor". In: *Blood* (2009). DOI: 10.1182/blood-2009-03-209981 (cit. on pp. 3, 6, 11).

[13] J. D. Welsh et al. "Hemodynamic regulation of perivalvular endothelial gene expression prevents deep venous thrombosis". In: *Journal of Clinical Investigation* 129.12 (Nov. 11, 2019), pp. 5489–5500. DOI: 10.1172/JCI124791 (cit. on pp. 3, 6, 11, 12).

[14] S. S. Abbas et al. "State-of-the-art numerical fluid–structure interaction methods for aortic and mitral heart valves simulations: A review:" in: *Simulation* (2021). DOI: 10.1177/00375497211023573 (cit. on pp. 4, 18).

[15] C. Chuck et al. "Investigating the Effect of Leaflet Quantity on Aortic Valve Stress-Strain Distribution". In: *The Proceedings of the National Academy of Sciences* (2016) (cit. on pp. 4, 7, 60).

[16] J. De Hart et al. "A three-dimensional computational analysis of fluid–structure interaction in the aortic valve". In: *Journal of Biomechanics* 36.1 (Jan. 2003), pp. 103–112. DOI: 10.1016/S0021-9290(02)00244-0 (cit. on pp. 4, 7, 18).

[17] K. Dumont et al. "Comparison of the Hemodynamic and Thrombogenic Performance of Two Bileaflet Mechanical Heart Valves Using a CFD/FSI Model". In: *Journal of Biomechanical Engineering* 129.4 (Aug. 1, 2007), pp. 558–565. DOI: 10.1115/1.2746378 (cit. on pp. 4, 7, 18).

[18] P. E. Hammer et al. "Surgical reconstruction of semilunar valves in the growing child: Should we mimic the venous valve? A simulation study". In: *The Journal of Thoracic and Cardiovascular Surgery* 153.2 (Feb. 2017), pp. 389–396. DOI: 10.1016/j.jtcvs.2016.08.019 (cit. on pp. 4, 55).

[19] H. J. Kim et al. "Determinants of effective orifice area in aortic valve replacement: anatomic and clinical factors". In: *Journal of Thoracic Disease* 12.5 (May 2020), pp. 1942–1951. DOI: 10.21037/jtd-20-188 (cit. on pp. 4, 58).

[20] W. Mao et al. "Fully-coupled fluid-structure interaction simulation of the aortic and mitral valves in a realistic 3D left ventricle model". In: *PLOS ONE* 12.9 (Sept. 8, 2017). Ed. by D. Tang, e0184729. DOI: 10.1371/journal.pone.0184729 (cit. on pp. 4, 7, 14, 18).

[21] N. Masoumi et al. "Laser microfabricated poly(glycerol sebacate) scaffolds for heart valve tissue engineering". In: *Journal of Biomedical Materials Research Part A* 101A.1 (Jan. 2013), pp. 104–114. DOI: 10.1002/jbm.a.34305 (cit. on pp. 4, 7).

[22] J. Sigüenza et al. “Fluid-structure interaction of a pulsatile flow with an aortic valve model: A combined experimental and numerical study: Fluid-structure interaction of a pulsatile flow with an aortic valve model: A combined experimental and numerical study”. In: *International Journal for Numerical Methods in Biomedical Engineering* 34.4 (Apr. 2018), e2945. DOI: 10.1002/cnm.2945 (cit. on pp. 4, 7, 14, 18, 21).

[23] P. Stradins. “Comparison of biomechanical and structural properties between human aortic and pulmonary valve*1”. In: *European Journal of Cardio-Thoracic Surgery* 26.3 (Sept. 2004), pp. 634–639. DOI: 10.1016/j.ejcts.2004.05.043 (cit. on pp. 4, 7, 8).

[24] K. Weind, C. Ellis, and D. Boughner. “Aortic valve cusp vessel density: Relationship with tissue thickness”. In: *The Journal of Thoracic and Cardiovascular Surgery* 123.2 (Feb. 2002), pp. 333–340. DOI: 10.1067/mtc.2002.119696 (cit. on pp. 4, 7).

[25] J. G. Betts et al. *Anatomy and Physiology 2e*. OpenStax. 2022 (cit. on pp. 4–6, 8, 52).

[26] R. F. Tuma, W. N. Duràn, and K. Ley. *Microcirculation*. Second Edition. Handbook of Physiology. Elsevier, 2008 (cit. on p. 5).

[27] M. H. Meissner. “Lower Extremity Venous Anatomy”. In: *Seminars in Interventional Radiology* 22.3 (Sept. 2005), pp. 147–156. DOI: 10.1055/s-2005-921948 (cit. on pp. 5, 52).

[28] S. C. Hofferberth et al. “A geometrically adaptable heart valve replacement”. In: *Science Translational Medicine* 12.531 (Feb. 19, 2020), eaay4006. DOI: 10.1126/scitranslmed.aay4006 (cit. on pp. 7, 53–56, 60, 103).

[29] S. A. Korossis, J. Fisher, and E. Ingham. “Cardiac valve replacement: A bioengineering approach”. In: *Cardiac valve replacement* (2000) (cit. on p. 7).

[30] N. Masoumi et al. “Tri-layered elastomeric scaffolds for engineering heart valve leaflets”. In: *Biomaterials* 35.27 (Sept. 2014), pp. 7774–7785. DOI: 10.1016/j.biomaterials.2014.04.039 (cit. on p. 7).

[31] F. Saremi et al. “CT and MR Imaging of the Pulmonary Valve”. In: *RadioGraphics* 34.1 (Jan. 2014), pp. 51–71. DOI: 10.1148/rg.341135026 (cit. on p. 7).

[32] M. Thubrikar et al. “The design of the normal aortic valve”. In: *American Journal of Physiology-Heart and Circulatory Physiology* 241.6 (Dec. 1, 1981), H795–H801. DOI: 10.1152/ajpheart.1981.241.6.H795 (cit. on p. 7).

[33] B. J. Bellhouse and L. Talbot. “The fluid mechanics of the aortic valve”. In: *Journal of Fluid Mechanics* 35.4 (Mar. 10, 1969), pp. 721–735. DOI: 10.1017/S0022112069001406 (cit. on p. 7).

[34] E. R. Mohler. “Mechanisms of aortic valve calcification”. In: *The American Journal of Cardiology* 94.11 (Dec. 2004), pp. 1396–1402. DOI: 10.1016/j.amjcard.2004.08.013 (cit. on p. 7).

[35] H. L. Oliveira et al. "Three-dimensional fluid–structure interaction simulation of the Wheatley aortic valve". In: *International Journal for Numerical Methods in Biomedical Engineering* 40.2 (Feb. 2024), e3792. DOI: 10.1002/cnm.3792 (cit. on pp. 7, 18).

[36] H. Y. Chen et al. "Biomechanical comparison between mono-, bi-, and tricuspid valve architectures". In: *Journal of Vascular Surgery: Venous and Lymphatic Disorders* 2.2 (Apr. 2014), 188–193.e1. DOI: 10.1016/j.jvsv.2013.08.004 (cit. on pp. 7, 18, 60).

[37] C. Duran-Hernandez, R. Ledesma-Alonso, and G. Etcheverry. "Using Autoregressive with Exogenous Input Models to Study Pulsatile Flows". In: *Applied Sciences* 10.22 (Nov. 20, 2020), p. 8228. DOI: 10.3390/app10228228 (cit. on pp. 7, 60).

[38] T. Le et al. "Computational methods for fluid-structure interaction simulation of heart valves in patient-specific left heart". In: *Fluids* (2021), p. 42. DOI: https://doi.org/10.3390/fluids7030094 (cit. on pp. 7, 18).

[39] M.-C. Hsu et al. "Dynamic and fluid–structure interaction simulations of bioprosthetic heart valves using parametric design with T-splines and Fung-type material models". In: *Computational Mechanics* 55.6 (June 2015), pp. 1211–1225. DOI: 10.1007/s00466-015-1166-x (cit. on pp. 7, 14, 18).

[40] D. Kamensky et al. "An immersogeometric variational framework for fluid–structure interaction: Application to bioprosthetic heart valves". In: *Computer Methods in Applied Mechanics and Engineering* 284 (Feb. 2015), pp. 1005–1053. DOI: 10.1016/j.cma.2014.10.040 (cit. on pp. 7, 18, 48).

[41] C. S. Peskin. "Flow Patterns Around Heart Valves: A Numerical Method". In: *Journal of Computational Physics* 10 (1972), pp. 252–271. DOI: https://doi.org/10.1016/0021-9991(72)90065-4 (cit. on pp. 7, 14, 18).

[42] F. Lurie and R. Kistner. "The Relative Position of Paired Valves at Venous Junctions Suggests Their Role in Modulating Three-dimensional Flow Pattern in Veins". In: *European Journal of Vascular and Endovascular Surgery* 44.3 (Sept. 2012), pp. 337–340. DOI: 10.1016/j.ejvs.2012.06.018 (cit. on pp. 8, 56, 57).

[43] *BioRender*. BioRender.com. URL: https://www.biorender.com (cit. on p. 9).

[44] *National Center for Biotechnology Information (NCBI)[Internet]. Bethesda (MD): National Library of Medicine (US), National Center for Biotechnology Information*. 1988. URL: https://pubmed.ncbi.nlm.nih.gov (cit. on p. 10).

[45] A. Giannetti. "Le début de la thrombose dans les veines profondes (dvt) : l'effet couplé de l'étirement et du cisaillement sur les cellules endothéliales." PhD thesis. 2023 (cit. on pp. 11, 53–55, 61).

[46] A. Tagliabue, L. Dedè, and A. Quarteroni. "Complex blood flow patterns in an idealized left ventricle: A numerical study". In: *Chaos: An Interdisciplinary Journal of Nonlinear Science* 27.9 (Sept. 1, 2017), p. 093939. DOI: 10.1063/1.5002120 (cit. on p. 14).

[47] L. Dedè, F. Menghini, and A. Quarteroni. "Computational fluid dynamics of blood flow in an idealized left human heart". In: *International Journal for Numerical Methods in Biomedical Engineering* 37.11 (Nov. 2021), e3287. DOI: 10.1002/cnm.3287 (cit. on p. 14).

[48] M. Ballard et al. "Probing the effect of morphology on lymphatic valve dynamic function". In: *Biomechanics and Modeling in Mechanobiology* 17.5 (Oct. 2018), pp. 1343–1356. DOI: 10.1007/s10237-018-1030-y (cit. on pp. 14, 18).

[49] H. Li et al. "The effects of valve leaflet mechanics on lymphatic pumping assessed using numerical simulations". In: *Scientific Reports* 9.1 (July 23, 2019), p. 10649. DOI: 10.1038/s41598-019-46669-9 (cit. on pp. 14, 18).

[50] K. T. Wolf et al. "Effect of valve spacing on peristaltic pumping". In: *Bioinspiration & Biomimetics* 18.3 (May 1, 2023), p. 035002. DOI: 10.1088/1748-3190/acbe85 (cit. on pp. 14, 18, 60).

[51] P. D. Ballyk et al. "Simulation of non-Newtonian blood flow in an end-to-side anastomosis". In: *Biorheology* (1994). DOI: 10.3233/bir-1994-31505 (cit. on p. 14).

[52] M. Conti et al. "Carotid artery hemodynamics before and after stenting: A patient specific CFD study". In: *Computers & Fluids* (2016). DOI: 10.1016/j.compfluid.2016.04.006 (cit. on p. 14).

[53] W. P. Guess et al. "Fluid-structure interaction modelling and stabilisation of a patient-specific arteriovenous access fistula". In: *Biomechanics and Modeling in Mechanobiology* 17.2 (Apr. 2018), pp. 479–497. DOI: 10.1007/s10237-017-0973-8 (cit. on pp. 14, 18).

[54] E. Järvinen et al. "A method for partitioned fluid–structure interaction computation of flow in arteries". In: *Medical Engineering & Physics* 30.7 (Sept. 2008), pp. 917–923. DOI: 10.1016/j.medengphy.2007.12.008 (cit. on p. 14).

[55] J. Hron and S. Turek. "A Monolithic FEM/Multigrid Solver for an ALE Formulation of Fluid-Structure Interaction with Applications in Biomechanics". In: *Fluid-Structure Interaction*. Vol. 53. Series Title: Lecture Notes in Computational Science and Engineering. Berlin, Heidelberg: Springer Berlin Heidelberg, 2006, pp. 146–170. DOI: 10.1007/3-540-34596-5_7 (cit. on p. 17).

[56] M. Razzaq et al. "FEM multigrid techniques for fluid–structure interaction with application to hemodynamics". In: *Applied Numerical Mathematics* 62.9 (Sept. 2012), pp. 1156–1170. DOI: 10.1016/j.apnum.2010.12.010 (cit. on p. 17).

[57] T. Richter. "A monolithic geometric multigrid solver for fluid-structure interactions in ALE formulation: Monolithic Geometric Multigrid Solver for Fluid-Structure Interactions". In: *International Journal for Numerical Methods in Engineering* 104.5 (Nov. 2, 2015), pp. 372–390. DOI: 10.1002/nme.4943 (cit. on p. 17).

[58] M. W. Gee, U. Küttler, and W. A. Wall. "Truly monolithic algebraic multigrid for fluid–structure interaction". In: *International Journal for Numerical Methods in Engineering* 85.8 (Feb. 25, 2011), pp. 987–1016. DOI: 10.1002/nme.3001 (cit. on p. 17).

[59] U. Langer and H. Yang. "Numerical Simulation of Fluid-Structure Interaction Problems with Hyperelastic Models: A Monolithic Approach". In: *Mathematics and Computers in Simulation* (Aug. 16, 2014). DOI: https://doi.org/10.1016/j.matcom.2016.07.008 (cit. on p. 17).

[60] M. Mayr et al. "A Temporal Consistent Monolithic Approach to Fluid-Structure Interaction Enabling Single Field Predictors". In: *SIAM Journal on Scientific Computing* 37.1 (Jan. 2015), B30–B59. DOI: 10.1137/140953253 (cit. on p. 17).

[61] R. Barrett et al. *Templates for the Solution of Linear Systems: Building Blocks for Iterative Methods*. SIAM. 2006 (cit. on p. 17).

[62] D. Balzani et al. "Numerical modeling of fluid–structure interaction in arteries with anisotropic polyconvex hyperelastic and anisotropic viscoelastic material models at finite strains". In: *International Journal for Numerical Methods in Biomedical Engineering* 32.10 (Oct. 2016), e02756. DOI: 10.1002/cnm.2756 (cit. on p. 17).

[63] A. T. Barker and X.-C. Cai. "Scalable parallel methods for monolithic coupling in fluid–structure interaction with application to blood flow modeling". In: *Journal of Computational Physics* 229.3 (Feb. 2010), pp. 642–659. DOI: 10.1016/j.jcp.2009.10.001 (cit. on p. 17).

[64] Y. Wu and X.-C. Cai. "A fully implicit domain decomposition based ALE framework for three-dimensional fluid–structure interaction with application in blood flow computation". In: *Journal of Computational Physics* 258 (Feb. 2014), pp. 524–537. DOI: 10.1016/j.jcp.2013.10.046 (cit. on p. 17).

[65] A. Gerbi. "Numerical approximation of cardiac electro-fluid-mechanical models: coupling strategies for large-scale simulation". PhD thesis. 2018 (cit. on p. 17).

[66] M. Bucelli et al. "Partitioned and Monolithic Algorithms for the Numerical Solution of Cardiac Fluid-Structure Interaction". In: *Communications in Computational Physics* 32.5 (June 2022), pp. 1217–1256. DOI: 10.4208/cicp.OA-2021-0243 (cit. on p. 17).

[67] M. Heil. "An efficient solver for the fully coupled solution of large-displacement fluid–structure interaction problems". In: *Computer Methods in Applied Mechanics and Engineering* 193.1 (Jan. 2004), pp. 1–23. DOI: 10.1016/j.cma.2003.09.006 (cit. on p. 17).

[68] R. Schussnig, D. R. Q. Pacheco, and T.-P. Fries. "Efficient split-step schemes for fluid-structure interaction involving incompressible generalised Newtonian flows". In: *Computers & Structures* 260 (Feb. 2022), p. 106718. DOI: 10.1016/j.compstruc.2021.106718 (cit. on p. 17).

[69] M. A. Fernández. "Coupling schemes for incompressible fluid-structure interaction: implicit, semi-implicit and explicit". In: *SeMA Journal* 55.1 (Sept. 2011), pp. 59–108. DOI: 10.1007/BF03322593 (cit. on p. 17).

[70] A. Naseri et al. "A semi-implicit coupling technique for fluid-structure interaction problems with strong added-mass effect". In: *Journal of Fluids and Structures* 80 (2018), pp. 94–112. DOI: https://doi.org/10.1016/j.jfluidstructs.2018.03.012 (cit. on p. 18).

[71] A. Swillens et al. "Comparison of Non-Invasive Methods for Measurement of Local Pulse Wave Velocity Using FSI-Simulations and In Vivo Data". In: *Annals of Biomedical Engineering* 41.7 (July 2013), pp. 1567–1578. DOI: 10.1007/s10439-012-0688-z (cit. on p. 18).

[72] T. E. Tezduyar et al. "Arterial fluid mechanics modeling with the stabilized space–time fluid–structure interaction technique". In: *International Journal for Numerical Methods in Fluids* 57.5 (June 20, 2008), pp. 601–629. DOI: 10.1002/fld.1633 (cit. on p. 18).

[73] S. Calandrini and E. Aulisa. "Fluid-structure interaction simulations of venous valves: a monolithic ALE method for large structural displacements". In: *International Journal for Numerical Methods in Biomedical Engineering* (May 3, 2018). DOI: https://doi.org/10.1002/cnm.3156 (cit. on pp. 18, 60).

[74] H. Y. Chen et al. "Hemodynamics of venous valve pairing and implications on helical flow". In: *Journal of Vascular Surgery: Venous and Lymphatic Disorders* 6.4 (July 2018), 517–522.e1. DOI: 10.1016/j.jvsv.2018.02.005 (cit. on pp. 18, 60, 69).

[75] M. Ariane et al. "Modelling and simulation of flow and agglomeration in deep veins valves using discrete multi physics". In: *Computers in Biology and Medicine* 89 (Oct. 2017), pp. 96–103. DOI: 10.1016/j.compbiomed.2017.07.020 (cit. on pp. 18, 60).

[76] G. A. Buxton and N. Clarke. "Computational Phlebology: The Simulation of a Vein Valve". In: *Journal of Biological Physics* 32.6 (Dec. 2006), pp. 507–521. DOI: 10.1007/s10867-007-9033-4 (cit. on pp. 18, 60, 65, 103).

[77] F.-B. Tian et al. “Fluid–structure interaction involving large deformations: 3D simulations and applications to biological systems”. In: *Journal of Computational Physics* 258 (Feb. 2014), pp. 451–469. DOI: 10.1016/j.jcp.2013.10.047 (cit. on p. 18).

[78] S. Badia, F. Nobile, and C. Vergara. “Fluid–structure partitioned procedures based on Robin transmission conditions”. In: *Journal of Computational Physics* 227.14 (July 2008), pp. 7027–7051. DOI: 10.1016/j.jcp.2008.04.006 (cit. on p. 18).

[79] A. Brandely and E. Lefrancois. “Etude de l’effet de la masse ajoutée pour garantir la convergence d’un problème de sloshing dans un réservoir partiellement rempli”. In: 22ème Congrès Français de Mécanique. CFM2015. Lyon, 2015. DOI: https://hal.science/hal-03444683v1 (cit. on p. 18).

[80] E. Burman and M. A. Fernández. “Stabilization of explicit coupling in fluid–structure interaction involving fluid incompressibility”. In: *Computer Methods in Applied Mechanics and Engineering* 198.5 (Jan. 2009), pp. 766–784. DOI: 10.1016/j.cma.2008.10.012 (cit. on p. 18).

[81] P. Causin, J. Gerbeau, and F. Nobile. “Added-mass effect in the design of partitioned algorithms for fluid–structure problems”. In: *Computer Methods in Applied Mechanics and Engineering* 194.42 (Oct. 2005), pp. 4506–4527. DOI: 10.1016/j.cma.2004.12.005 (cit. on p. 18).

[82] C. Förster, W. A. Wall, and E. Ramm. “Artificial added mass instabilities in sequential staggered coupling of nonlinear structures and incompressible viscous flows”. In: *Computer Methods in Applied Mechanics and Engineering* 196.7 (Jan. 2007), pp. 1278–1293. DOI: 10.1016/j.cma.2006.09.002 (cit. on p. 18).

[83] E. Lefrançois. “How an added mass matrix estimation may dramatically improve FSI calculations for moving foils”. In: *Applied Mathematical Modelling* 51 (Nov. 2017), pp. 655–668. DOI: 10.1016/j.apm.2017.07.022 (cit. on p. 18).

[84] E. Lefrançois et al. “Overcoming the added mass effect in FSI calculations relating to dynamic squat”. In: *Ocean Engineering* 267 (Jan. 2023), p. 113280. DOI: 10.1016/j.oceaneng.2022.113280 (cit. on p. 18).

[85] P. Le Tallec and J. Mouro. “Fluid structure interaction with large structural displacements”. In: *Computer Methods in Applied Mechanics and Engineering* 190.24 (Mar. 2001), pp. 3039–3067. DOI: 10.1016/S0045-7825(00)00381-9 (cit. on p. 18).

[86] D. Panunzio, M.-A. Puscas, and R. Lagrange. “FSI—vibrations of immersed cylinders. Simulations with the engineering open-source code TrioCFD. Test cases and experimental comparisons”. In: *Comptes Rendus. Mécanique* 350 (G3 Sept. 6, 2022), pp. 451–476. DOI: 10.5802/crmeca.126 (cit. on p. 18).

[87] M. Song, E. Lefrançois, and M. Rachik. "A partitioned coupling scheme extended to structures interacting with high-density fluid flows". In: *Computers & Fluids* 84 (Sept. 2013), pp. 190–202. DOI: 10.1016/j.compfluid.2013.05.022 (cit. on p. 18).

[88] A. Bogaers et al. "Extending the robustness and efficiency of artificial compressibility for partitioned fluid–structure interactions". In: *Computer Methods in Applied Mechanics and Engineering* 283 (Jan. 2015), pp. 1278–1295. DOI: 10.1016/j.cma.2014.08.021 (cit. on p. 18).

[89] J. Degroote et al. "Simulation of fluid–structure interaction with the interface artificial compressibility method". In: *International Journal for Numerical Methods in Biomedical Engineering* 26.3 (Mar. 2010), pp. 276–289. DOI: 10.1002/cnm.1276 (cit. on p. 18).

[90] J. Degroote et al. "Stability of a coupling technique for partitioned solvers in FSI applications". In: *Computers & Structures* 86.23 (Dec. 2008), pp. 2224–2234. DOI: 10.1016/j.compstruc.2008.05.005 (cit. on pp. 18, 19, 48).

[91] J. A. Vierendeels et al. "Computer Simulation of Intraventricular Flow and Pressure Gradients During Diastole". In: *Journal of Biomechanical Engineering* 122.6 (Dec. 1, 2000), pp. 667–674. DOI: 10.1115/1.1318941 (cit. on p. 18).

[92] A. La Spina et al. "On the role of (weak) compressibility for fluid-structure interaction solvers". In: *International Journal for Numerical Methods in Fluids* 92.2 (Feb. 2020), pp. 129–147. DOI: 10.1002/fld.4776 (cit. on p. 18).

[93] P. Raback et al. "Fluid-structure interaction boundary condition by artificial compressibility". In: ECCOMAS Computational Fluid Dynamics Conference 2001. 2001, p. 13 (cit. on p. 18).

[94] K. Riemslagh, J. Vierendeels, and E. Dick. "An efficient coupling procedure for flexible wall fluid-structure interation". In: Fluids 2000 Conference and Exhibit. 2000, p. 13. DOI: https://doi.org/10.2514/6.2000-2336 (cit. on p. 18).

[95] C. Kadapa. "Insights into the performance of loosely-coupled FSI schemes based on Robin boundary conditions". In: *ArXiv* (May 31, 2021). DOI: https://doi.org/10.48550/arXiv.2105.14831 (cit. on p. 18).

[96] M. Akbay, C. Schroeder, and T. Shinar. "Boundary pressure projection for partitioned solution of fluid-structure interaction with incompressible Dirichlet fluid domains". In: *Journal of Computational Physics* 425 (Jan. 2021), p. 109894. DOI: 10.1016/j.jcp.2020.109894 (cit. on p. 18).

[97] S. Badia, A. Quaini, and A. Quarteroni. "Splitting Methods Based on Algebraic Factorization for Fluid-Structure Interaction". In: *SIAM Journal on Scientific Computing* 30.4 (Jan. 2008), pp. 1778–1805. DOI: 10.1137/070680497 (cit. on p. 18).

[98] M. A. Fernández, J. Mullaert, and M. Vidrascu. "Explicit Robin–Neumann schemes for the coupling of incompressible fluids with thin-walled structures". In: *Computer Methods in Applied Mechanics and Engineering* 267 (Dec. 2013), pp. 566–593. DOI: 10.1016/j.cma.2013.09.020 (cit. on p. 18).

[99] R. Thirumalaisamy, N. A. Patankar, and A. P. S. Bhalla. "Handling Neumann and Robin boundary conditions in a fictitious domain volume penalization framework". In: *Journal of Computational Physics* 448 (Jan. 2022), p. 110726. DOI: 10.1016/j.jcp.2021.110726 (cit. on p. 18).

[100] Ž. Tuković et al. "Added Mass Partitioned Fluid–Structure Interaction Solver Based on a Robin Boundary Condition for Pressure". In: *OpenFOAM®*. Cham: Springer International Publishing, 2019, pp. 1–22. DOI: 10.1007/978-3-319-60846-4_1 (cit. on p. 18).

[101] A. Aitken. "On Bernoulli's numerical solution of algebraic equations". In: *Proceedings of the Royal Society of Edinburgh* 46 (1926), pp. 289–305. DOI: doi:10.1017/S0370164600022070 (cit. on p. 19).

[102] A. Aitken. "Studies in Practical Mathematics. II. The evaluation of the latent roots and latent vectors of a matrix." In: *Proceedings of the Royal Society of Edinburgh* (1937), p. 269. DOI: doi:10.1017/S0370164600013808 (cit. on pp. 19, 47).

[103] B. M. Irons and R. C. Tuck. "A version of the Aitken accelerator for computer iteration". In: *International Journal for Numerical Methods in Engineering* 1.3 (July 1969), pp. 275–277. DOI: 10.1002/nme.1620010306 (cit. on pp. 19, 47).

[104] M. Cerquaglia et al. "A fully partitioned Lagrangian framework for FSI problems characterized by free surfaces, large solid deformations and displacements, and strong added-mass effects". In: *Computer Methods in Applied Mechanics and Engineering* 348 (May 2019), pp. 409–442. DOI: 10.1016/j.cma.2019.01.021 (cit. on pp. 19, 48).

[105] J. H. Chow and E. Ng. "Strongly coupled partitioned six degree-of-freedom rigid body motion solver with Aitken's dynamic under-relaxation". In: *International Journal of Naval Architecture and Ocean Engineering* 8.4 (July 2016), pp. 320–329. DOI: 10.1016/j.ijnaoe.2016.04.001 (cit. on p. 19).

[106] U. Küttler and W. A. Wall. "Fixed-point fluid–structure interaction solvers with dynamic relaxation". In: *Computational Mechanics* 43.1 (Dec. 2008), pp. 61–72. DOI: 10.1007/s00466-008-0255-5 (cit. on pp. 19, 48).

[107] A. Shamanskiy and B. Simeon. "Mesh moving techniques in fluid-structure interaction: robustness, accumulated distortion and computational efficiency". In: *Computational Mechanics* 67.2 (Feb. 2021), pp. 583–600. DOI: 10.1007/s00466-020-01950-x (cit. on pp. 19, 48).

[108] Yigit, Sternel, and Schäfer. "Efficiency of fluid-structure interaction simulations with adaptive underrelaxation and multigrid acceleration". In: *The International Journal of Multiphysics* 1.1 (Jan. 2007), pp. 85–99. DOI: 10.1260/175095407780130535 (cit. on pp. 19, 48).

[109] D. P. Mok. *Partitionierte Lösungsansätze in der Strukturdynamik und der Fluid-Struktur-Interaktion*. Bericht / Institut für Baustatik der Universität Stuttgart Nr. 36. Stuttgart: Inst. f. Baustatik, Univ, 2001 (cit. on pp. 19, 48).

[110] T. Fabbri et al. "Design of a high fidelity Fluid–Structure Interaction solver using LES on unstructured grid". In: *Computers & Fluids* 265 (Oct. 2023), p. 105963. DOI: 10.1016/j.compfluid.2023.105963 (cit. on pp. 19, 104).

[111] P. Matteoli, F. Nicoud, and S. Mendez. "Impact of the membrane viscosity on the tank-treading behavior of red blood cells". In: *Physical Review Fluids* 6.4 (Apr. 20, 2021), p. 043602. DOI: 10.1103/PhysRevFluids.6.043602 (cit. on pp. 19, 21).

[112] P. Taraconat et al. "Detecting cells rotations for increasing the robustness of cell sizing by impedance measurements, with or without machine learning". In: *Cytometry Part A* 99.10 (Oct. 2021), pp. 977–986. DOI: 10.1002/cyto.a.24356 (cit. on pp. 19, 21).

[113] W. A. Wall et al. "Partitioned Analysis of Transient Nonlinear Fluid Structure Interaction Problems Including Free Surface Effects". In: *Multifield Problems*. Berlin, Heidelberg: Springer Berlin Heidelberg, 2000, pp. 159–166. DOI: 10.1007/978-3-662-04015-7_18 (cit. on p. 19).

[114] J.-F. Gerbeau and M. Vidrascu. "A Quasi-Newton Algorithm Based on a Reduced Model for Fluid-Structure Interaction Problems in Blood Flows". In: *ESAIM: Mathematical Modelling and Numerical Analysis* 37.4 (July 2003), pp. 631–647. DOI: 10.1051/m2an:2003049 (cit. on p. 19).

[115] C. Kassiotis et al. "Nonlinear fluid–structure interaction problem. Part I: implicit partitioned algorithm, nonlinear stability proof and validation examples". In: *Computational Mechanics* 47.3 (Mar. 2011), pp. 305–323. DOI: 10.1007/s00466-010-0545-6 (cit. on p. 19).

[116] W. G. Dettmer and D. Perić. "A Fully Implicit Computational Strategy for Strongly Coupled Fluid–Solid Interaction". In: *Archives of Computational Methods in Engineering* 14.3 (Aug. 17, 2007), pp. 205–247. DOI: 10.1007/s11831-007-9006-6 (cit. on p. 19).

[117] B. Hübner, E. Walhorn, and D. Dinkler. "A monolithic approach to fluid–structure interaction using space–time finite elements". In: *Computer Methods in Applied Mechanics and Engineering* 193.23 (June 2004), pp. 2087–2104. DOI: 10.1016/j.cma.2004.01.024 (cit. on p. 19).

[118] H. G. Matthies, R. Niekamp, and J. Steindorf. "Algorithms for strong coupling procedures". In: *Computer Methods in Applied Mechanics and Engineering* 195.17 (Mar. 2006), pp. 2028–2049. DOI: 10.1016/j.cma.2004.11.032 (cit. on p. 19).

[119] S. Turek and J. Hron. "Proposal for Numerical Benchmarking of Fluid-Structure Interaction between an Elastic Object and Laminar Incompressible Flow". In: *Fluid-Structure Interaction*. Ed. by M. Schäfer and H.-J. Bungartz. Vol. 53. Series Title: Lecture Notes in Computational Science and Engineering. Berlin, Heidelberg: Springer Berlin Heidelberg, 2006, pp. 371–385. DOI: 10.1007/3-540-34596-5_15 (cit. on p. 19).

[120] T. Fabbri. "Development of a high fidelity fluid-structure interaction solver : towards flexible foils simulation." PhD thesis. Université de Grenoble, 2022 (cit. on pp. 19, 25, 44, 106).

[121] T. Wick. "Fully Eulerian fluid–structure interaction for time-dependent problems". In: *Computer Methods in Applied Mechanics and Engineering* 255 (Mar. 2013), pp. 14–26. DOI: 10.1016/j.cma.2012.11.009 (cit. on p. 19).

[122] G. De Nayer et al. "Flow past a cylinder with a flexible splitter plate: A complementary experimental–numerical investigation and a new FSI test case (FSI-PfS-1a)". In: *Computers & Fluids* 99 (July 2014), pp. 18–43. DOI: 10.1016/j.compfluid.2014.04.020 (cit. on p. 19).

[123] F. P. T. Baaijens. "A fictitious domain/mortar element method for fluid-structure interaction". In: *International Journal for Numerical Methods in Fluids* 35.7 (Apr. 15, 2001), pp. 743–761. DOI: 10.1002/1097-0363(20010415)35:7<743::AID-FLD109>3.0.CO;2-A (cit. on pp. 19, 48).

[124] T. Bano et al. "Investigation of Fluid-Structure Interaction Induced Bending for Elastic Flaps in a Cross Flow". In: *Applied Sciences* 10.18 (Sept. 5, 2020), p. 6177. DOI: 10.3390/app10186177 (cit. on p. 19).

[125] L. Boilevin-Kayl, M. A. Fernández, and J.-F. Gerbeau. "A Loosely Coupled Scheme for Fictitious Domain Approximations of Fluid-Structure Interaction Problems with Immersed Thin-Walled Structures". In: *SIAM Journal on Scientific Computing* 41.2 (Jan. 2019), B351–B374. DOI: 10.1137/18M1192779 (cit. on pp. 19, 48, 49).

[126] A. Gil et al. "The Immersed Structural Potential Method for haemodynamic applications". In: *Journal of Computational Physics* 229.22 (Nov. 2010), pp. 8613–8641. DOI: 10.1016/j.jcp.2010.08.005 (cit. on pp. 19, 48).

[127] C. Hesch et al. "On continuum immersed strategies for Fluid–Structure Interaction". In: *Computer Methods in Applied Mechanics and Engineering* 247-248 (Nov. 2012), pp. 51–64. DOI: 10.1016/j.cma.2012.07.021 (cit. on pp. 19, 48).

[128] S. Basting et al. "Extended ALE Method for fluid–structure interaction problems with large structural displacements". In: *Journal of Computational Physics* 331 (Feb. 2017), pp. 312–336. DOI: 10.1016/j.jcp.2016.11.043 (cit. on p. 19).

[129] C. Kapada, W. G. Dettmer, and D. Peric. "A fictitious domain/distributed Lagrange multiplier based fluid-structure interaction scheme with hierarchical B-Spline grids". In: *Computer Methods in Applied Mechanics and Engineering* (2015), pp. 1–27. DOI: https://doi.org/10.1016/j.cma.2015.12.023 (cit. on p. 19).

[130] A. Gil et al. "An enhanced Immersed Structural Potential Method for fluid–structure interaction". In: *Journal of Computational Physics* 250 (Oct. 2013), pp. 178–205. DOI: 10.1016/j.jcp.2013.05.011 (cit. on p. 19).

[131] T. Wick. "Flapping and contact FSI computations with the fluid–solid interface-tracking/interface-capturing technique and mesh adaptivity". In: *Computational Mechanics* 53.1 (Jan. 2014), pp. 29–43. DOI: 10.1007/s00466-013-0890-3 (cit. on p. 19).

[132] J. Lorentzon and J. Revstedt. "A numerical study of partitioned fluid-structure interaction applied to a cantilever in incompressible turbulent flow". In: *International Journal for Numerical Methods in Engineering* 121.5 (Mar. 15, 2020), pp. 806–827. DOI: 10.1002/nme.6245 (cit. on p. 19).

[133] S. Mendez and F. Nicoud. *YALES2BIO*. URL: https://imag.umontpellier.fr/~yales2bio/ (cit. on p. 20).

[134] V. Moureau, P. Domingo, and L. Vervisch. "Design of a massively parallel CFD code for complex geometries". In: *Comptes Rendus Mécanique*. High Performance Computing 339.2 (Feb. 1, 2011), pp. 141–148. DOI: 10.1016/j.crme.2010.12.001 (cit. on p. 20).

[135] M. Malandain, N. Maheu, and V. Moureau. "Optimization of the deflated Conjugate Gradient algorithm for the solving of elliptic equations on massively parallel machines". In: *Journal of Computational Physics* 238 (Apr. 2013), pp. 32–47. DOI: 10.1016/j.jcp.2012.11.046 (cit. on pp. 20, 24).

[136] C. Chnafa, S. Mendez, and F. Nicoud. "Image-based large-eddy simulation in a realistic left heart". In: *Computers & Fluids* 94 (May 1, 2014), pp. 173–187. DOI: 10.1016/j.compfluid.2014.01.030 (cit. on pp. 21, 22).

[137] L. Lanotte et al. "Red cells' dynamic morphologies govern blood shear thinning under microcirculatory flow conditions". In: *Proceedings of the National Academy of Sciences of the United States of America* (2016). DOI: 10.1073/pnas.1608074113 (cit. on p. 21).

[138] S. Mendez, E. Gibaud, and F. Nicoud. "An unstructured solver for simulations of deformable particles in flows at arbitrary Reynolds numbers". In: *Journal of Computational Physics* 256 (Jan. 1, 2014), pp. 465–483. DOI: 10.1016/j.jcp.2013.08.061 (cit. on p. 21).

[139] T. Puiseux et al. “Numerical simulation of time-resolved 3D phase-contrast magnetic resonance imaging”. In: *PLOS ONE* 16.3 (Mar. 26, 2021). Ed. by I. Borazjani, e0248816. DOI: 10.1371/journal.pone.0248816 (cit. on p. 21).

[140] M. Garreau et al. “Accelerated sequences of 4D flow MRI using GRAPPA and compressed sensing: A comparison against conventional MRI and computational fluid dynamics”. In: *Magnetic Resonance in Medicine* 88.6 (Dec. 2022), pp. 2432–2446. DOI: 10.1002/mrm.29404 (cit. on p. 21).

[141] S. Mendez, W. Garcia, and A. Nicolas. “From Microscopic Droplets to Macroscopic Crowds: Crossing the Scales in Models of Short-Range Respiratory Disease Transmission, with Application to COVID-19”. In: *Advanced Science* 10.19 (July 2023), p. 2205255. DOI: 10.1002/advs.202205255 (cit. on p. 21).

[142] J. Williamson. “Low-storage Runge-Kutta schemes”. In: *Journal of Computational Physics* 35.1 (Mar. 1980), pp. 48–56. DOI: 10.1016/0021-9991(80)90033-9 (cit. on p. 22).

[143] C. Farhat, P. Geuzaine, and C. Grandmont. “The Discrete Geometric Conservation Law and the Nonlinear Stability of ALE Schemes for the Solution of Flow Problems on Moving Grids”. In: *Journal of Computational Physics* 174.2 (Dec. 2001), pp. 669–694. DOI: 10.1006/jcph.2001.6932 (cit. on p. 23).

[144] D. Boffy and L. Gastaldi. “Stability and geometric conservation laws for ALE formulations”. In: *Computer Methods in Applied Mechanics and Engineering* (2003), pp. 4717–4739. DOI: https://doi.org/10.1016/j.cma.2004.02.020 (cit. on p. 23).

[145] O. C. Zienkiewicz, R. L. Taylor, and J. Z. Zhu. *The finite element method: its basis and fundamentals*. 6. ed., reprint., transferred to digital print. Amsterdam Heidelberg: Elsevier, 2010 (cit. on p. 25).

[146] O. Zienkiewicz, R. Taylor, and D. Fox. “General Problems in Solid Mechanics and Nonlinearity”. In: *The Finite Element Method for Solid and Structural Mechanics*. Elsevier, 2014, pp. 1–20. DOI: 10.1016/B978-1-85617-634-7.00001-6 (cit. on pp. 25, 37).

[147] M. Liu and D. G. Corman. “Formulation of Rayleigh damping and its extensions”. In: *Computers & Structures* (1995), pp. 277–285. DOI: https://doi.org/10.1016/0045-7949(94)00611-6 (cit. on p. 37).

[148] T. K. Caughey and M. E. J. O’Kelly. “Classical Normal Modes in Damped Linear Dynamic Systems”. In: *Journal of Applied Mechanics* (1965). DOI: https://doi.org/10.1115/1.3643949 (cit. on p. 37).

[149] G. Zhang et al. “A mass lumping scheme for the 10-node tetrahedral element”. In: *Engineering Analysis with Boundary Elements* 106 (Sept. 2019), pp. 190–200. DOI: 10.1016/j.enganabound.2019.04.018 (cit. on pp. 38, 106).

[150] P. Flores et al. “On the continuous contact force models for soft materials in multibody dynamics”. In: *Multibody System Dynamics* 25.3 (Mar. 2011), pp. 357–375. DOI: 10.1007/s11044-010-9237-4 (cit. on p. 39).

[151] F. Chouly and H. Patrick. "On convergence of the penalty method for unilateral contact problems". In: *Applied Numerical Mathematics* 65 (Mar. 2013), pp. 27–40. DOI: 10.1016/j.apnum.2012.10.003 (cit. on p. 39).

[152] J. Hallquist, G. Goudreau, and D. Benson. "Sliding interfaces with contact-impact in large-scale Lagrangian computations". In: *Computer Methods in Applied Mechanics and Engineering* 51.1 (Sept. 1985), pp. 107–137. DOI: 10.1016/0045-7825(85)90030-1 (cit. on p. 39).

[153] P. Flores. *Contact-impact analysis in multibody systems based on the nonsmooth dynamics approach*. 2015. DOI: 10.13140/RG.2.1.5059.6327 (cit. on p. 39).

[154] G. Gilardi and I. Sharf. "Literature survey of contact dynamics modelling". In: *Mechanism and Machine Theory* 37.10 (Oct. 2002), pp. 1213–1239. DOI: 10.1016/S0094-114X(02)00045-9 (cit. on p. 39).

[155] P. Flores. "Contact mechanics for dynamical systems: a comprehensive review". In: *Multibody System Dynamics* 54.2 (Feb. 1, 2022), pp. 127–177. DOI: 10.1007/s11044-021-09803-y (cit. on p. 39).

[156] M. Hubbard and W. J. Stronge. "Bounce of hollow balls on flat surfaces". In: *Sports Engineering* 4.2 (May 2001), pp. 49–61. DOI: 10.1046/j.1460-2687.2001.00073.x (cit. on pp. 40, 41, 43).

[157] C. Dobrzynski and P. Frey. "Anisotropic Delaunay Mesh Adaptation for Unsteady Simulations". In: *Proceedings of the 17th International Meshing Roundtable*. Berlin, Heidelberg: Springer Berlin Heidelberg, 2008, pp. 177–194. DOI: 10.1007/978-3-540-87921-3_11 (cit. on p. 46).

[158] C. Dapogny, C. Dobrzynski, and P. Frey. "Three-dimensional adaptive domain remeshing, implicit domain meshing, and applications to free and moving boundary problems". In: *Journal of Computational Physics* 262 (Apr. 2014), pp. 358–378. DOI: 10.1016/j.jcp.2014.01.005 (cit. on p. 46).

[159] P. Benard et al. "Mesh adaptation for large-eddy simulations in complex geometries". In: *International Journal for Numerical Methods in Fluids* 81.12 (Aug. 30, 2016), pp. 719–740. DOI: 10.1002/fld.4204 (cit. on p. 46).

[160] S. Pertant et al. "A finite-volume method for simulating contact lines on unstructured meshes in a conservative level-set framework". In: *Journal of Computational Physics* 444 (Nov. 2021), p. 110582. DOI: 10.1016/j.jcp.2021.110582 (cit. on p. 46).

[161] R. Janodet et al. "An unstructured conservative level-set algorithm coupled with dynamic mesh adaptation for the computation of liquid-gas flows". In: 29th European Conference on Liquid Atomization and Spray Systems. Paris, 2019 (cit. on p. 46).

[162] A. Pushkarev et al. "Numerical approach for simulation of moving bodies by using the dynamic mesh adaptation method within ALE technique". In: *ECCOMAS MSF 2017*. Ljubljana, Slovenia, 2017. DOI: https://normandie-univ.hal.science/hal-01658684v1 (cit. on p. 46).

[163] F. Duchaine, T. Morel, and A. Piacentini. "On a first use of CWIPI at CERFACS". In: *CERFACS Reports* (2009) (cit. on p. 46).

[164] E. Quémerais. *Coupling with interpolation parallel interface*. URL: `https://w3.onera.fr/cwipi/fr` (cit. on p. 46).

[165] A. Caggiati. "The venous valves of the lower limbs". In: *Phlebolymphology* 20.2 (2013), pp. 87–95 (cit. on pp. 53, 54).

[166] A. Fronek et al. "Common femoral vein dimensions and hemodynamics including Valsalva response as a function of sex, age, and ethnicity in a population study". In: *Journal of Vascular Surgery* 33.5 (May 2001), pp. 1050–1056. DOI: 10.1067/mva.2001.113496 (cit. on pp. 53, 57, 58).

[167] J. Keiler, R. Seidel, and A. Wree. "The femoral vein diameter and its correlation with sex, age and body mass index – An anatomical parameter with clinical relevance". In: *Phlebology: The Journal of Venous Disease* 34.1 (Feb. 2019), pp. 58–69. DOI: 10.1177/0268355518772746 (cit. on p. 53).

[168] C. A. Engelhorn et al. "Vascular ultrasonographic measurement of diameters of great saphenous veins without reflux in women". In: *Jornal Vascular Brasileiro* 16.2 (May 18, 2017), pp. 92–97. DOI: 10.1590/1677-5449.008016 (cit. on p. 54).

[169] I. A. Maher et al. "Anatomical measurement of great saphenous vein and superficial femoral vein by colored duplex ultrasound". In: *International Journal of Advanced Research* 6.2 (Feb. 28, 2018), pp. 1012–1020. DOI: 10.21474/IJAR01/6522 (cit. on p. 54).

[170] T. O. Kalayci et al. "Venous flow volume measured by duplex ultrasound can be used as an indicator of impaired tissue perfusion in patients with peripheral arterial disease". In: *Medical Ultrasonography* 17.4 (Dec. 1, 2015), pp. 482–486. DOI: 10.11152/mu.2013.2066.174.flw (cit. on pp. 54, 57, 58, 64).

[171] A. Caggiati. "Fascial relations and structure of the tributaries of the saphenous veins". In: *Surgical and Radiologic Anatomy* 22.3 (Dec. 2000), pp. 191–196. DOI: 10.1007/s00276-000-0191-3 (cit. on p. 54).

[172] J. V. Psaila and J. Melhuish. "Viscoelastic properties and collagen content of the long saphenous vein in normal and varicose veins". In: *British Journal of Surgery* 76.1 (1989), pp. 37–40. DOI: 10.1002/bjs.1800760112 (cit. on p. 54).

[173] D. P. Vekilov and K. J. Grande-Allen. "Mechanical Properties of Diseased Veins". In: *Methodist DeBakey Cardiovascular Journal* 14.3 (July 1, 2018), p. 182. DOI: 10.14797/mdcj-14-3-182 (cit. on p. 54).

[174] C. D. Buescher et al. "Experimental Studies of the Effects of Abnormal Venous Valves on Fluid Flow". In: *Biotechnology Progress* 21.3 (Sept. 5, 2008), pp. 938–945. DOI: 10.1021/bp049835u (cit. on p. 54).

[175] K. Van Langevelde, A. Šrámek, and F. R. Rosendaal. "The Effect of Aging on Venous Valves". In: *Arteriosclerosis, Thrombosis, and Vascular Biology* 30.10 (Oct. 2010), pp. 2075–2080. DOI: 10.1161/ATVBAHA.110.209049 (cit. on p. 54).

[176] D. Pavcnik et al. "Percutaneous bioprosthetic venous valve: A long-term study in sheep". In: *Journal of Vascular Surgery* 35.3 (Mar. 2002), pp. 598–602. DOI: 10.1067/mva.2002.118825 (cit. on p. 54).

[177] J. S. Ackroyd, M. Pattison, and N. L. Browse. "A study of the mechanical properties of fresh and preserved human femoral vein wall and valve cusps". In: *British Journal of Surgery* 72.2 (1984), pp. 117–119. DOI: 10.1002/bjs.1800720216 (cit. on pp. 55, 56, 60, 65).

[178] H.-Y. S. Huang and J. Lu. "Biaxial mechanical properties of bovine jugular venous valve leaflet tissues". In: *Biomechanics and Modeling in Mechanobiology* 16.6 (Dec. 2017), pp. 1911–1923. DOI: 10.1007/s10237-017-0927-1 (cit. on p. 56).

[179] J. Lu and H.-Y. S. Huang. "Biaxial mechanical properties of venous valve leaflet tissues". In: 40th Annual Meeting of the American Society of Biomechanics. Raleigh, NC, USA, 2016. DOI: http://www.lib.ncsu.edu/resolver/1840.16/10980 (cit. on p. 56).

[180] A. A. Benson and H.-Y. S. Huang. "Tissue Level Mechanical Properties and Extracellular Matrix Investigation of the Bovine Jugular Venous Valve Tissue". In: *Bioengineering* 6.2 (May 14, 2019), p. 45. DOI: 10.3390/bioengineering6020045 (cit. on p. 56).

[181] G. A. Holzapfel. "Determination of material models for arterial walls from uniaxial extension tests and histological structure". In: *Journal of Theoretical Biology* 238.2 (Jan. 2006), pp. 290–302. DOI: 10.1016/j.jtbi.2005.05.006 (cit. on p. 56).

[182] B. Herrera, G. Fortuny, and F. Marimón. "Calculation of Human Femoral Vein Wall Parameters In Vivo From Clinical Data for Specific Patient". In: *Journal of Biomechanical Engineering* 134.12 (Dec. 1, 2012), p. 124501. DOI: 10.1115/1.4007948 (cit. on p. 56).

[183] G. L. Moneta et al. "Duplex ultrasound assessment of venous diameters, peak velocities, and flow patterns". In: *Journal of Vascular Surgery* 8.3 (1988), pp. 286–291. DOI: https://doi.org/10.1067/mva.1988.avs0080286 (cit. on p. 56).

[184] R. J. Min, N. M. Khilnani, and P. Golia. "Duplex Ultrasound Evaluation of Lower Extremity Venous Insufficiency". In: *Journal of Vascular and Interventional Radiology* 14.10 (Oct. 2003), pp. 1233–1241. DOI: 10.1097/01.RVI.0000092663.72261.37 (cit. on p. 56).

[185] D. Gunnell. "Associations of height, leg length, and lung function with cardiovascular risk factors in the Midspan Family Study". In: *Journal of Epidemiology & Community Health* 57.2 (Feb. 1, 2003), pp. 141–146. DOI: 10.1136/jech.57.2.141 (cit. on p. 56).

[186] F. Lurie. "Physiology and Pathophysiology of the Venous System". In: *Pan-Vascular Medicine*. Berlin, Heidelberg: Springer Berlin Heidelberg, 2014, pp. 1–19. DOI: 10.1007/978-3-642-37393-0_159-1 (cit. on pp. 57, 84).

[187] R. A. Tauraginskii et al. "Calf muscle pump pressure-flow cycle during ambulation". In: *Journal of Vascular Surgery: Venous and Lymphatic Disorders* 11.4 (July 2023), 783–792.e7. DOI: 10.1016/j.jvsv.2023.04.002 (cit. on p. 57).

[188] E. P. Lin et al. "The Importance of Monophasic Doppler Waveforms in the Common Femoral Vein: A Retrospective Study". In: *Journal of Ultrasound in Medicine* 26.7 (July 2007), pp. 885–891. DOI: 10.7863/jum.2007.26.7.885 (cit. on p. 57).

[189] F. Lurie, R. L. Kistner, and B. Eklof. "The mechanism of venous valve closure in normal physiologic conditions". In: *Journal of Vascular Surgery* 35.4 (Apr. 2002), pp. 713–717. DOI: 10.1067/mva.2002.121123 (cit. on p. 57).

[190] F. Lurie et al. "Mechanism of venous valve closure and role of the valve in circulation: a new concept". In: *Journal of Vascular Surgery* 38.5 (Nov. 2003), pp. 955–961. DOI: 10.1016/S0741-5214(03)00711-0 (cit. on pp. 57, 58, 67).

[191] F. Lurie and R. L. Kistner. "On the existence of helical flow in veins of the lower extremities". In: *Journal of Vascular Surgery: Venous and Lymphatic Disorders* 1.2 (Apr. 2013), pp. 134–138. DOI: 10.1016/j.jvsv.2012.08.002 (cit. on pp. 57, 69).

[192] K.-H. Nam et al. "Velocity field measurements of valvular blood flow in a human superficial vein using high-frequency ultrasound speckle image velocimetry". In: *The International Journal of Cardiovascular Imaging* 28.1 (Jan. 2012), pp. 69–77. DOI: 10.1007/s10554-010-9778-x (cit. on pp. 57–59).

[193] S. E. Rittgers, M. T. Oberdier, and S. Pottala. "Physiologically-based testing system for the mechanical characterization of prosthetic vein valves". In: *BioMedical Engineering OnLine* 6.1 (2007), p. 29. DOI: 10.1186/1475-925X-6-29 (cit. on p. 58).

[194] H. Y. Chen et al. "Prosthetic venous valve patient selection by validated physics-based computational models". In: *Journal of Vascular Surgery: Venous and Lymphatic Disorders* 3.1 (Jan. 2015), pp. 75–80. DOI: 10.1016/j.jvsv.2014.07.003 (cit. on p. 58).

[195] N. S. Aziz et al. "Computational Fluid Dynamics Simulation on Blood Velocity and Vorticity of Venous Valve Behaviour". In: *9th International Conference on Robotic, Vision, Signal Processing and Power Applications*. Vol. 398. Series Title: Lecture Notes in Electrical Engineering. Singapore: Springer Singapore, 2017, pp. 617–625. DOI: 10.1007/978-981-10-1721-6_67 (cit. on p. 59).

[196] N. K. Rajeeva Pandian and A. Jain. "In silico analyses of blood flow and oxygen transport in human micro-veins and valves". In: *Clinical Hemorheology and Microcirculation* 81.1 (Apr. 23, 2022), pp. 81–96. DOI: 10.3233/CH-211345 (cit. on p. 59).

[197] G. Niccolini et al. "Possible Assessment of Calf Venous Pump Efficiency by Computational Fluid Dynamics Approach". In: *Frontiers in Physiology* 11 (Sept. 8, 2020), p. 1003. DOI: 10.3389/fphys.2020.01003 (cit. on p. 59).

[198] M. Ariane et al. "Using Discrete Multi-Physics for studying the dynamics of emboli in flexible venous valves". In: *Computers & Fluids* 166 (Apr. 2018), pp. 57–63. DOI: 10.1016/j.compfluid.2018.01.037 (cit. on p. 60).

[199] Y. A. Gataulin, A. D. Yukhnev, and D. A. Rosukhovskiy. "Fluid–structure interactions modeling the venous valve". In: *Journal of Physics: Conference Series* 1128 (Nov. 2018), p. 012009. DOI: 10.1088/1742-6596/1128/1/012009 (cit. on p. 60).

[200] Y. A. Gataulin et al. "Numerical analysis of the leaflet elasticity effect on the flow in the model of a venous valve". In: *Journal of Physics: Conference Series* 1359.1 (Nov. 1, 2019), p. 012010. DOI: 10.1088/1742-6596/1359/1/012010 (cit. on p. 60).

[201] Y. A. Gataulin, A. D. Yukhnev, and D. A. Rosukhovskiy. "Numerical analysis of the flow in the model of a venous valve: normal and surgical corrected". In: *Journal of Physics: Conference Series* 2103.1 (Nov. 1, 2021), p. 012207. DOI: 10.1088/1742-6596/2103/1/012207 (cit. on p. 60).

[202] H. Y. Chen et al. "Search for an Optimal Design of a Bioprosthetic Venous Valve: In silico and in vitro Studies". In: *European Journal of Vascular and Endovascular Surgery* 58.1 (July 2019), pp. 112–119. DOI: 10.1016/j.ejvs.2018.12.008 (cit. on p. 60).

[203] A. Dryden and M. Ballard. "Numerical investigation of a biomimetic elastic valve for microfluidic pumping". In: *Journal of Fluids and Structures* 103 (May 2021), p. 103265. DOI: 10.1016/j.jfluidstructs.2021.103265 (cit. on p. 60).

[204] X. Liu and L. Liu. "Effect of valve lesion on venous valve cycle: A modified immersed finite element modeling". In: *PLOS ONE* 14.3 (Mar. 4, 2019). Ed. by A. Pandolfi, e0213012. DOI: 10.1371/journal.pone.0213012 (cit. on p. 60).

[205] H. Chen et al. "Editor's Choice – Fluid–Structure Interaction Simulations of Aortic Dissection with Bench Validation". In: *European Journal of Vascular and Endovascular Surgery* 52.5 (Nov. 2016), pp. 589–595. DOI: 10.1016/j.ejvs.2016.07.006 (cit. on p. 60).

[206] H. A. Baksamawi et al. "Modelling Particle Agglomeration on through Elastic Valves under Flow". In: *ChemEngineering* 5.3 (July 26, 2021), p. 40. DOI: 10.3390/chemengineering5030040 (cit. on p. 60).

[207] E. Goranova and N. Nikolov. "Numerical modeling of the venous valve functionning". In: *Journal of Theoretical and Applied Mechanics* (2021), p. 20 (cit. on p. 60).

[208] A. J. Narracott et al. "Fluid-structure interaction analysis of venous valve haemodynamics". In: *4th International Conference on Computational and Mathematical Biomedical Engineering*. 4th International Conference on Computational and Mathematical Biomedical Engineering. July 1, 2015, p. 4 (cit. on p. 60).

[209] A. J. Narracott et al. "Analysis of a mechanical heart valve prosthesis and a native venous valve: Two distinct applications of FSI to biomedical applications". In: *International Journal for Numerical Methods in Biomedical Engineering* 26.3 (Mar. 2010), pp. 421–434. DOI: 10.1002/cnm.1323 (cit. on p. 60).

[210] M. Simão et al. "Identification of DVT diseases using numerical simulations". In: *Medical & Biological Engineering & Computing* 54.10 (Oct. 2016), pp. 1591–1609. DOI: 10.1007/s11517-015-1446-9 (cit. on p. 60).

[211] W.-H. Tien et al. "Characterization of a Bioprosthetic Bicuspid Venous Valve Hemodynamics: Implications for Mechanism of Valve Dynamics". In: *European Journal of Vascular and Endovascular Surgery* 48.4 (Oct. 2014), pp. 459–464. DOI: 10.1016/j.ejvs.2014.06.034 (cit. on p. 60).

[212] Z. Hajati et al. "Fluid-structure interaction of blood flow around a vein valve". In: *BioImpacts* 4.3 (Aug. 23, 2017), pp. 149–166. DOI: 10.34172/bi.2020.21 (cit. on p. 60).

[213] E. Soifer et al. "The effect of pathologic venous valve on neighboring valves: fluid–structure interactions modeling". In: *Medical & Biological Engineering & Computing* 55.6 (June 2017), pp. 991–999. DOI: 10.1007/s11517-016-1575-9 (cit. on p. 60).

[214] L. G. Tikhomolova et al. "Fluid–structure interaction modelling of the venous valve with elastic leaflets". In: *Journal of Physics: Conference Series* 1697.1 (Dec. 1, 2020), p. 012041. DOI: 10.1088/1742-6596/1697/1/012041 (cit. on p. 60).

[215] N. Wijeratne and K. Hoo. "Numerical studies on the hemodynamics in the human vein and venous valve". In: *2008 American Control Conference*. 2008 American Control Conference (ACC '08). Seattle, WA: IEEE, June 2008, pp. 147–152. DOI: 10.1109/ACC.2008.4586482 (cit. on p. 60).

[216] P. P. Gogia and J. H. Braatz. "Validity and Reliability of Leg Length Measurements". In: *Journal of Orthopaedic & Sports Physical Therapy* 8.4 (Oct. 1986), pp. 185–188. DOI: 10.2519/jospt.1986.8.4.185 (cit. on p. 65).

[217] K. Ozden, C. Sert, and Y. Yazicioglu. "Effect of stenosis shape on the sound emitted from a constricted blood vessel". In: *Medical & Biological Engineering & Computing* 58.3 (Mar. 2020), pp. 643–658. DOI: 10.1007/s11517-020-02119-7 (cit. on p. 84).

[218] C. Zhu, J.-H. Seo, and R. Mittal. "Computational modelling and analysis of haemodynamics in a simple model of aortic stenosis". In: *Journal of Fluid Mechanics* 851 (Sept. 25, 2018), pp. 23–49. DOI: 10.1017/jfm.2018.463 (cit. on p. 84).

[219] M. J. Kunov, D. A. Steinman, and C. R. Ethier. "Particle Volumetric Residence Time Calculations in Arterial Geometries". In: *Journal of Biomechanical Engineering* 118.2 (May 1, 1996), pp. 158–164. DOI: 10.1115/1.2795954 (cit. on p. 92).

[220] S. Balay et al. "Efficient Management of Parallelism in Object Oriented Numerical Software Libraries". In: *Modern Software Tools in Scientific Computing*. Ed. by E. Arge, A. M. Bruaset, and H. P. Langtangen. Birkhäuser Press, 1997, pp. 163–202 (cit. on p. 106).

[221] S. Balay et al. *PETSc Web page*. 2024 (cit. on p. 106).

[222] Balay et al. *PETSc/TAO Users Manual*. 2024 (cit. on p. 106).

Résumé

L'objectif principal est de mieux comprendre l'hémodynamique des valves veineuses, ainsi que leurs implications potentielles dans les maladies telles que la thrombose veineuse profonde. Un modèle de valve veineuse basé sur l'hypothèse d'une réserve de surface a été développé. Une analyse structurale complète des feuillets de la valve est proposée pour étudier les déformations sous contraintes mécaniques. Des simulations numériques d'interaction fluide-structure (IFS) ont ensuite été réalisées pour reproduire les conditions de flux sanguin en situation de pompe respiratoire en position allongée. Les résultats montrent que la sensibilité de la valve à la pression permet une ouverture avec une perte de pression faible. La position le long de la cuisse ainsi qu'une géométrie modifiée ont été identifiés comme principaux acteurs influant sur le drainage du sinus. Les résultats obtenus ouvrent des perspectives pour améliorer la compréhension de l'hémodynamique des valves veineuses et comprendre les mécanismes impliqués dans les pathologies veineuses.

Mots clés: thrombose veineuse, YALES2BIO, interaction fluide structure, effort pariétal

Abstract

The main objective is to better understand the hemodynamics of venous valves, and their potential implications in diseases such as deep vein thrombosis. A venous valve model based on the surface reserve hypothesis has been developed. A first comprehensive structural analysis of the valve leaflets is proposed to study deformations under mechanical stress. Numerical simulations of fluid-structure interaction (FSI) were then carried out to reproduce blood flow conditions in a respiratory pump situation in the supine position. The results show that the valve's sensitivity to pressure enables it to open with little pressure loss. Position along the thigh and modified geometry were identified as the main factors influencing drainage. These results open up new avenues for improving our understanding of venous valve hemodynamics and the mechanisms involved in venous pathologies.

Keywords: deep vein thrombosis, YALES2BIO, fluid-structure interaction, wall shear stress